

Micro-XRF geochemical and micropaleontological evidence for
prehistoric land disturbance, Serpent Mounds complex, Rice Lake
(Ontario, Canada)

By Tynan A. Pringle, B.Sc. (Hons.)

*A Thesis Submitted to the School of Graduate Studies in the Partial Fulfillment of the
Requirements for the Degree Master of Science*

McMaster University © Copyright by Tynan A. Pringle January 22, 2019

McMaster University

Master of Science (2019)

Hamilton, Ontario (School of Geography and Earth Science)

TITLE: Micro-XRF geochemical and micropaleontological evidence for prehistoric land disturbance, Serpent Mounds complex, Rice Lake (Ontario, Canada)

AUTHOR: Tynan A. Pringle (McMaster University)

SUPERVISOR: Dr. Joseph I. Boyce

NUMBER OF PAGES: xvii, 150

Lay Abstract

Serpent Mounds is a prehistoric (Middle Woodland Period, ca. 2000–1000 BP) burial mound complex located in Rice Lake, Ontario. Archaeological excavation (1897–1970) determined the site was occupied by people of the Point Peninsula culture (ca. 2200–1350 BP) on a seasonal basis, for burial rites and shellfish gathering. Many questions remain with regard to the date of mounds construction, how long the site was occupied, and how occupation and construction activities impacted the local environment. The site has been designated as a National Historical Site and excavation is no longer permitted in the interest of site preservation and cultural value to First Nations.

This study investigated the history of environmental changes associated with prehistoric indigenous and European land use changes using minimally-invasive methods, including sonar bathymetric mapping, micro-X-ray fluorescence core scanning (μ -XRF-CS) and microfossil analysis of lake sediment cores. Sonar data were employed to map the lake bottom relief (bathymetry) and to reconstruct past changes in lake levels and shoreline positions. micro-X-ray fluorescence (μ -XRF) methods measures changes in elemental abundance in lake core samples to identify human occupation phases and land disturbance. Microfossils (testate amoebae) track the ecosystem response to environmental changes associated with human occupation. The geochemical and microfossil data identified an interval of increased sediment delivery to Rice Lake, coinciding with the arrival of Point Peninsula peoples. The land disturbance is recognized in cores by an increase in zirconium (Zr), titanium (Ti) and other soil-derived elements. During this phase, lake levels rose gradually, wetlands expanded and wild rice was abundant resource available to indigenous peoples. Following European colonization in the 1820's, and the construction of the Hastings Dam (1838 CE), lake levels increased rapidly by over 2 m, causing a shift to a more nutrient-rich (eutrophic) lake environment and a

decline in wild rice stands. Soil erosion associated with European land clearance is recorded by in a dramatic increase in the abundance of soil-derived elements.

Abstract

Serpent Mounds is a prehistoric (Middle Woodland Period, ca. 2000–1000 BP) burial mound complex located on the north shore of Rice Lake, in southern Ontario, Canada. The complex includes a 60 m long and 10 m wide sinuous earthwork ridge interpreted as a serpent effigy and eight smaller oval mound structures. Archaeological excavations determined seasonal site occupation for harvesting wild rice and shellfish and conducting mortuary rites. The timing of mound construction and site occupation is poorly constrained by limited radiocarbon dates, restricted to burials. The site is of high cultural importance as the only known effigy mound structure in Canada and is a sacred First Nations burial ground; thus all investigation must employ non-invasive techniques.

High-resolution μ -XRF-CS and micropaleontologic analysis (testate amoebae) of 12 lake sediment cores was employed to investigate the timing of mound construction, and assess geochemical records of prehistoric land disturbance. Land disturbance is indicated by increased sediment flux, by rising abundance of minerogenic elements (K, Ti, Zr, Si, Fe) within a distinctive silt-rich gyttja unit. The event is also recorded in the thecamoebian assemblage, which is dominated by indicators of a eutrophic, turbid lake environment. Principal component analysis (PCA) and cluster analysis (CA) of μ -XRF data identify distinctive chemofacies across several cores. Accelerator mass spectrometer (AMS) ^{14}C dates for the prehistoric land disturbance episode correspond with the Point Peninsula occupation, indicating a protracted occupation period of ~750 years (2050–1300 cal BP) with two major peaks in soil erosion at 1900 and 1450 cal BP. The sedimentation rate ($> 1.5 \text{ mm yr}^{-1}$) during the Middle Woodland phase of enhanced erosion was comparable to that during the 1838 CE dam construction. The reconstructed Middle Woodland paleoshoreline and water levels indicate a shallow lake and wetland environment, with viable habitats for wild rice stands and shellfish resources. The results

demonstrate that μ -XRF-CS and micropaleontological methods are important for the investigation of culturally-sensitive archaeological sites, including sacred burial grounds where conventional archaeological excavation cannot be undertaken.

Acknowledgements

I would like to offer sincere thanks to Chief Carr of Hiawatha First Nation, Chief Marsden of Alderville First Nation, the Hiawatha First Nation Lands Department, and all members of the Williams Treaty Nations without whom this research would not be possible. The privilege to work around a site as important as Serpent Mounds has been an unforgettable experience, and I do very much hope the findings of this research will be of great benefit to the mutual understanding of human-landscape interactions amongst both archaeologists and indigenous peoples. Huge thanks to my liason officer, Valerie Minelga of Parks Canada. Your patience and expedient response to my often rushed requests for permitting and licensing decisively kept this project moving forward, when it could have easily been lost in bureaucratic confusion. A very special thank you to Bill and Cory at Sunset Cove Resort on Rice Lake, who graciously provided lodging, a research vessel, and equipment. Their involvement in this project make them an indispensable part of the research team.

To Dr. Elizabeth P. Sonnenburg, I owe my interest and eventual pursuit of geoarchaeology, not to mention the supplementary SONAR data provided from her doctoral work. It was at a small Ontario Archaeological Society meeting in Ancaster, Ontario many years ago that I first learned of Rice Lake's archaeological history from Dr. Sonnenburg, but could never have imagined I would one day be taking up the torch of exploration at that very same lake. To my colleagues Nicholas Riddick, Jeremy Gabriel, Majed Turkistani, Anya Janzen, Sian Ford, Chelsi McNeill-Jewer, Christian DiMaria, Doug Blomfield, Alexandra Usyk and everybody within the School of Geography and Earth Sciences who have provided strong friendships since my undergraduate years: I couldn't have done it without you.

For my partner, Dr. Michael D.M. Dryden, I graciously thank for his contributions to the PyTrax code, introducing me to \LaTeX , Python, and photography, and for always

pushing me to improve my quality of work as a scientist. Meeting Michael changed everything I know about myself, and how I approach the world as a geoscientist is evermore improved because of him. A heartfelt thank you to my mother, father, and my brothers, who have always provided the means for me to pursue my scientific passions.

For the privilege of using the Itrax Core Scanner, and for teaching me the fundamentals of excellent figure aesthetics in my undergraduate years, I am eternally grateful to Dr. Eduard G. Reinhardt. I reserve a final, most important thank you to my supervisor, Dr. Joseph I. Boyce, for granting me freedom with this project which few other advisors would provide. Thank you for always providing guidance when I strayed too far from my objectives, and for being open to my many coding experiments which yielded deeper data analysis than I could have hoped for at the outset of these last two years.

This research project was funded through a Natural Sciences and Engineering Research Council of Canada (NSERC) Discovery Grant to J. Boyce and McMaster University Postgraduate Scholarship to T.A. Pringle.

...

Contents

Lay Abstract	iii
Abstract	v
Acknowledgements	vii
Acronyms	xvi
Thesis Format and Contributions	xvii
1 Introduction	1
1.1 Background	1
1.2 Objectives	5
1.3 Setting and Previous Work	7
1.3.1 Study Area	7
1.3.2 Previous Work	9
1.4 Archaeological Background	12
1.5 Methods	20
1.5.1 X-ray Fluorescence (XRF) and Core Scanning	20
1.5.2 Itrax μ -XRF Core Scanner	23
1.5.3 μ -XRF Key Elements and Matrix Effects	25
1.5.3.1 Terrigenous Elements	25
1.5.3.2 Organic Productivity Markers	27

1.5.3.3	Matrix Effects	29
1.5.3.4	Post-processing of Spectra	30
1.5.4	Bathymetry Surveys	31
1.5.5	Core extraction, sampling, and analysis	33
1.6	μ -XRF Data Processing and Analysis: PyTrax	33
1.6.1	Processing Protocols	37
1.7	Thecamoebian Analysis	38

2	Micro-XRF geochemical and micropaleontological evidence for prehistoric land disturbance: construction of the Middle Woodland (ca. 300 BCE–700 CE) Serpent Mounds complex, Rice Lake (Ontario, Canada)	41
2.1	Abstract	41
2.2	Introduction	42
2.3	Study Area	46
2.3.1	Physical Setting	46
2.3.2	Water Levels and Paleoenvironments	49
2.3.3	Site Archaeology	50
2.4	Methods	53
2.4.1	Bathymetric mapping	53
2.4.2	Coring and sediment chronology	54
2.4.3	μ -XRF core scanning	55
2.4.3.1	Statistical analysis	56
2.4.4	Micropaleontology	58
2.5	Results	60
2.5.1	Core lithofacies	60
2.5.2	Itrax element profiles	64
2.5.3	Chemofacies	70

2.5.3.1	FCM Chemofacies	73
2.5.3.2	Detrital Input	73
2.5.3.3	Organic Productivity (Org)	76
2.5.3.4	Carbonate Facies (C1, C2, C3)	76
2.5.3.5	Geochemical Stasis (Eq)	77
2.5.3.6	GOM Chemofacies	77
2.5.3.7	Detrital Input	77
2.5.3.8	Organic Productivity	78
2.5.3.9	Geochemical Stasis	78
2.5.4	Thecamoebian biofacies	80
2.5.4.1	Transgressive Shoreline (B1)	82
2.5.4.2	Turbid shallow lake (B2)	83
2.5.5	Post-Dam eutrophic lake (B3)	84
2.5.5.1	Marginal Wetland (B4)	84
2.5.5.2	Pre-colonial Eutrophic Lake (B5)	85
2.6	Discussion	85
2.6.1	Late Holocene Water Levels and Paleogeography	85
2.6.2	Mid-Holocene Shoreline Transgression (4500 – 3300 cal BP)	86
2.6.3	Middle Woodland Point Peninsula Occupation (2200 – 1300 cal BP)	88
2.6.4	European Settlement Phase (ca. 1820 CE)	91
2.6.5	Archaeological implications	92
2.6.5.1	Prehistoric land disturbance	92
2.6.5.2	Climate and geomorphic factors?	94
2.6.5.3	Non-invasive archaeology	97
2.7	Conclusions	99
3	Summary	101
3.1	Conclusions	101

3.2 Future Work and Archaeological Implications	104
A Chapter 1 Supplement	108
B Chapter 2 Supplement	110
Bibliography	129

List of Figures

1.1	Map of Point Peninsula and Hopewell cultures	2
1.2	Aerial photos of Serpent Mounds	4
1.3	LiDAR digital terrain model of Rice Lake area	8
1.4	Water level curve from Sonnenburg et al. (2013)	10
1.5	Middle Woodland sites at Rice Lake and their contents	14
1.6	Excavation map of Johnston (1968) superimposed over LiDAR map	17
1.7	Excavation photos from Johnston (1968)	19
1.8	Components of Itrax Core Scanner	24
1.9	Map of paths for sonar survey	32
2.1	LiDAR DTM of Rice Lake with inset map of Lake Ontario and Hopewell Culture influence region	43
2.2	Composite SONAR digital bathymetric model with core and site locations	47
2.3	Processing flowchart	56
2.4	Stratigraphic log	61
2.5	SRPM02 age-depth model	63
2.6	SRPM02 elemental profile	65
2.7	Pearson's r correlation heatmap of selected elements	66
2.8	Explained PCA results	70
2.9	Heatmap and cluster results of PCA	72
2.10	Heatmap of element abundances sorted by PCA cluster affiliation	74
2.11	Chemofacies distribution among all cores in dataset	75

2.12 Stratigraphic profile of chemofacies across cores	79
2.13 Thecamoebian biofacies with Q- and R-mode dendrogram	81
2.14 Water level reconstructions	87
2.15 SRPM02 climate correlation	89
A2.1 SRPM-01 element profile	111
A2.2 SRPM-01 chemofacies composition	112
A2.3 SRPM-02 element profile	113
A2.4 SRPM-02 chemofacies composition	114
A2.5 SRPM-03 element profile	115
A2.6 SRPM-05 lithological profile	116
A2.7 SRPM-06 lithological profile	117
A2.8 SRPM-07 element profile	118
A2.9 SRPM-07 chemofacies composition	119
A2.10 SRPM-08 lithological profile	120
A2.11 SRPM-09 element profile	121
A2.12 SRPM-10 element profile	122
A2.13 SRPM-10 chemofacies composition	123
A2.14 SRPM-11 element profile	124
A2.15 SRPM-11 chemofacies composition	125
A2.16 SRPM-12 element profile	126
A2.17 SRPM-12 chemofacies composition	127

List of Tables

1.1	A table of Middle Woodland period archaeological sites at Rice Lake . . .	15
2.1	Radiocarbon dates from this study and others	55
2.2	Table of biofacies count statistics	82
A1.1	Functions of PyTrax	109
A2.1	Table of PCA values for RGB images of cores	110
A2.2	Table of microfossil count statistics	128

Acronyms

AMS accelerator mass spectrometer

CA cluster analysis

DBM digital bathymetric model

EH-2 erosional hiatus 2

FCM full-core model

GOM gyttja-only model

LiDAR light detection and ranging

MSE mean squared error

PCA principal component analysis

μ -XRF micro-X-ray fluorescence

μ -XRF-CS micro-X-ray fluorescence core scanning

\bar{x} SDI average Shannon diversity index

Thesis Format and Contributions

This thesis is in 'sandwich' format with three chapters. **Chapter 1** introduces the research topic and objectives, physical geography, site archaeology, and instruments employed in this study.

Chapter 2 has been formatted for publication in *Quaternary Science Reviews*, and is co-authored by Dr. Joseph I. Boyce. This chapter outlines the specific survey methods, statistical approaches to micro-XRF data processing, paleobathymetric reconstructions, and micropaleontological findings of this thesis, with data interpretation in the discussion. Tynan A. Pringle was responsible for all licensing and permitting, data collection and processing, with supervision and technical review provided by Dr. Joseph I. Boyce. C. Dimaria (McMaster University) assisted with coring and SONAR surveys (May-June, 2017). Age modelling and workflow optimization of the PyTrax code, and Python technical assistance was provided by M.D.M. Dryden (University of Toronto). Additional SONAR data for DBM was contributed by E.P. sonnenburg (Stantec Consulting, Ltd).

Chapter 3 summarizes the thesis results, and outlines areas of potential future work, and adaptations to improve the resolution of non-invasive geoarchaeological surveys in North America.

Chapter 1

Introduction

1.1 Background

The Early and Middle Woodland periods (ca. 3000–1000 BP) in the northeastern North America saw the development of inter-regional trade networks, greater social organization and many significant technological innovations, including the introduction of pottery making, horticulture and significantly, the construction of sophisticated earthwork monuments and burial mounds (Bernardini 2004; Abrams and Freter 2005; Milner 2005; Henry and Barrier 2016; Mueller 2018). Monumental earthworks and burial mound complexes were a distinctive feature of the Early-Middle Woodland Adena and Hopewell cultures of the Ohio River Valley (Kenyon 1986; Burks 2014). It is estimated that more than 10,000 earthwork structures exist in the Ohio Valley alone, including the iconic 400 m long Great Serpent Mound (Adams County, Ohio) (Herrmann et al. 2014). The construction of ceremonial earthworks and burial mounds was also practiced by some Middle Woodland peoples in eastern North America, as a result of the expansion of Hopewell cultural influences beyond the Ohio Valley (Spence et al. 1979; Kenyon 1986; Spence et al. 1990). The so-called Hopewell interaction sphere (Fig. 1.1) enveloped a large region of the midcontinent, extending eastward from Ohio into New York State

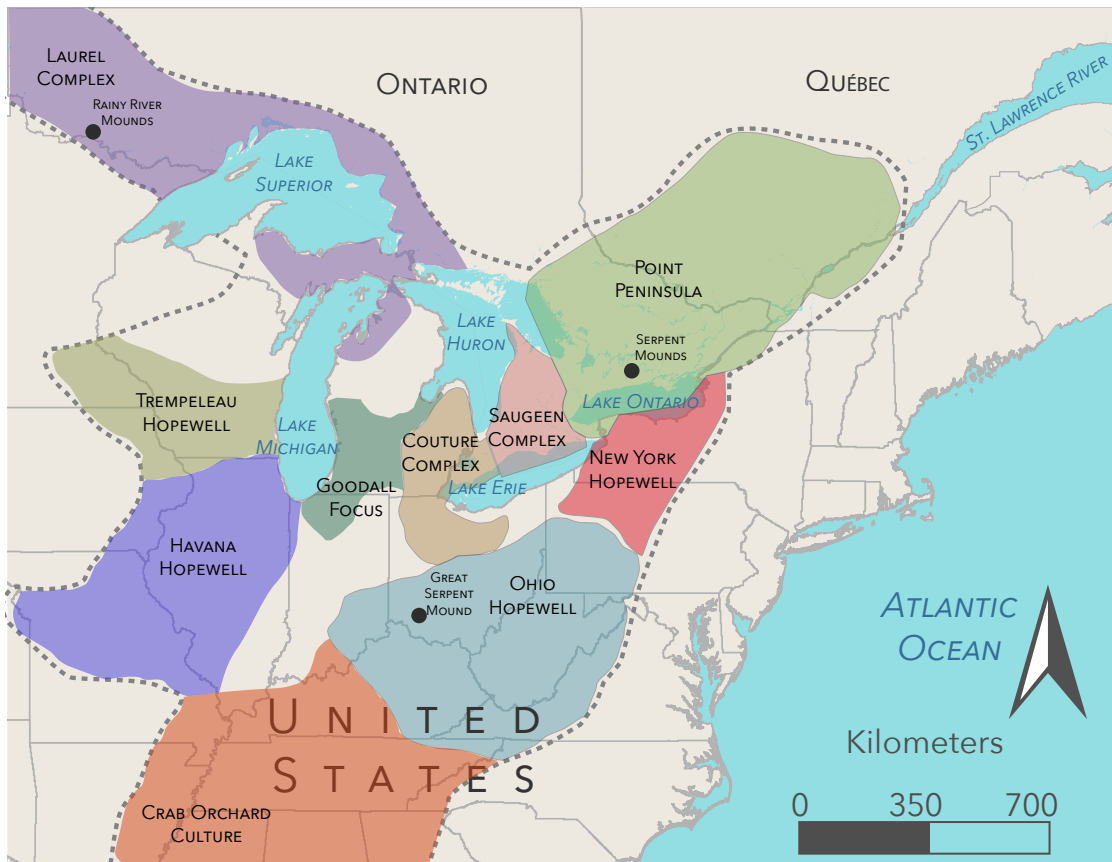


Figure 1.1: Point Peninsula culture range with associated culture regions with Hopewellian influence, in southern Ontario and Québec, and the northeastern United States (dotted line from Boivin et al. (2013))

and southern Québec, to Rainy River in northern Ontario (the Laurel Complex), and southward into the US Gulf States (Fig. 1.1).

In southern Ontario, Canada, mound-building was practiced by peoples of the Point Peninsula Complex (ca. 2400–1300 BP) (Kenyon 1986; Ellis and Ferris 1990; Carr and Case 2006; Walker 2015). The most impressive and archaeologically important burial mound complex is Serpent Mounds, located on the north shore of Rice Lake, Ontario (Fig. 1.2). The mound complex comprises a 60 m-long, 8 m-wide earthen work ridge (the Serpent)(Mound E, Fig. 1.2) and eight smaller, elliptical mounds, up to 14 m in diameter. The Serpent mound rises 1.5–2m above the surrounding topography and has a distinctive sinuous crestline in plan (Fig. 1.2) that has been interpreted as a serpent effigy (Boyle 1897; Kenyon 1986). The mounds occupy a 4.4 ha area on the south slope of a flat-topped drumlin hill (Roach Point) at about 15 m above the present level of Rice Lake (Fig. 1.2B). Serpent mounds was first documented in the late 1800's (Boyle 1897) and the first systematic archaeological excavations were conducted between 1950–1955 by the Royal Ontario Museum (see section 1.4) (Johnston 1957; Johnston 1968; Schwarcz et al. 1985; Ellis and Ferris 1990). The excavations were extensive and resulted in the removal of a total of 159 skeletons from burials in several locations (Harrison and Katzenberg 2003). Johnston (1968) estimated that the mounds were constructed over a span of approximately 170 years, from 120 AD until 290 AD.

The oldest date from the mound, however, represents the age of a burial, and may not indicate the actual onset of the mound construction. Further, the three radiocarbon dates used in this estimate were uncalibrated, leading to age uncertainties which cannot be resolved using ceramic seriation (Johnston 1968).

Although many burial mound complexes are known from this time period in Ontario, Serpent Mounds (Fig. 1.2) stands apart as the only prehistoric serpent effigy earthwork in Canada (Kenyon 1986). The site was designated as a National Historical Site



Figure 1.2: **A.** Aerial photos of the Serpent Mound Group (Foreground: Mound D, Middle: Serpent Mound, Back: Mound H). **B.** Northeast facing view of Serpent Mounds and Roach Point, with East Sugar Island at the top-left of the frame.

of Canada in 1985 (ParksCanada 2018). Following decades of operation as a Provincial park, Serpent Mounds has been closed to the public since 2013 and are now managed by the Hiawatha First Nation (Hiawatha, Ontario). The burial mounds are of significant spiritual importance to the indigenous community and as caretakers of the mounds, they have not permitted further excavation of the site. In recent years, analysis of the mounds has shifted to non-invasive methods. Most recently, Dillane (2010) performed a detailed viewshed analysis of Serpent Mounds using remote sensing and GIS methods, to investigate the function of mounds as territorial markers.

1.2 Objectives

Archaeological excavations conducted at Serpent Mounds in the 1950's and early 1960's significantly expanded understanding of the Point Peninsula Complex and Hopewell cultural influences (Johnston 1968; Kenyon 1986). As outlined in the introduction, there remain significant knowledge gaps with regard to:

1. The timing of mound construction during the Middle Woodland period,
2. The mound construction methods (whether the mounds were built incrementally or in a single event) and the duration over which the mounds were built;
3. The environmental impacts of seasonal site occupation and mound construction activities on the landscape and the lake habitats.

Due to the high cultural value and sacred importance of Serpent Mounds, it is no longer possible to use conventional archaeological excavations or other invasive methods (e.g. coring) to address the above questions. In order to preserve the integrity of the site and to respect the sacred value of the burial ground, future investigations must employ non-invasive techniques. The aim of this thesis is to investigate the potential

for non-invasive investigation of prehistoric landscape modification (i.e. burial mound construction) at Serpent Mounds using lake sediment geochemical and microfossil (thecamoebian) records. The specific objectives are:

1. To examine the geochemical record of land disturbance using micro-X-ray fluorescence (μ -XRF) elemental analysis.
2. To reconstruct changes in the lake paleoenvironments during the Middle Woodland period to the present, including the changes following construction of the Hastings Dam (1838 CE).
3. To determine changes in the lake water levels, paleobathymetry and shoreline positions, from the Middle Woodland to present.
4. To evaluate micro-X-ray fluorescence core scanning (μ -XRF-CS) as a tool for remote detection of land disturbance events in lake sediment records.

A combination of μ -XRF-CS and micropaleontological data (thecamoebians) is used to pursue these objectives. This study is the first attempt to detect geochemical signals of landscape modification using μ -XRF-CS methods, in pre-agricultural, pre-contact North American archaeology. Multivariate statistics (principal component analysis, cluster analysis) classify core chemofacies, to assist in identification of high terrigenous input episodes in the basin. μ -XRF-CS is supplemented by new testate amoebae data, which records ecosystem changes during the previously unevaluated Early Woodland period to Present (Sonnenburg et al. 2013). New radiocarbon dates permit calculation of sedimentation rate changes using bayesian age-depth modelling (Blaauw and Christen 2011), and update the water level reconstructions of Sonnenburg et al. (2012) and Yu and McAndrews (1994). These techniques provide finer spatial and temporal resolution of sediment deposited in the Late Holocene, in a manner which is archaeologically non-destructive.

The large volume of compiled μ -XRF-CS is typically problematic for analysis. Thus, a specialized Python code is developed for work-flow automation and data reduction. PyTrax is a data visualization and multivariate statistical code, written in Python 3.0, to address this problem. Python offers a flexible, and powerful option for customized data handling, which is achieved by few proprietary software packages in the environmental sciences. The capabilities of PyTrax exceed that of many third-party Itrax software packages geared more towards basic data visualization (Croudace and Rothwell 2015a). It offers a streamlined data preparation process, precisely aligning core imagery, radiographs, and XRF data, with further options for normalization and element ratios. It provides easy-to-use principal component analysis (PCA) options, as well as cluster analysis (CA), designed to be paired with the data reduction.

1.3 Setting and Previous Work

1.3.1 Study Area

Rice Lake is located 20 km south of Peterborough, Ontario, is 26 km in length, 3–4km in width, and has a maximum water depth of 10 m. The surrounding area is defined by the Peterborough Drumlin field (North), and the Oak Ridges Moraine (South), with bedrock composed of Ordovician-aged limestone (Fig. 1.3) (Sharpe et al. 1997; Gravenor 1957). The current lake levels were established in 1838 CE by construction of the Hastings Dam, raising water levels by over 2 m and greatly increasing the lake's surface area, inundating much of the original shoreline (Yu and McAndrews 1994). Given the lake's shallow average depth (4 m), the abrupt rise in water level post-dam would have dramatically changed the flow regime of the Indian and Otonabee rivers, which feed the lake from the north through glacial spillways (Gravenor 1957). The Indian River presently drains little more than 1 km north of the study area, and may likely have flowed much further

into the present extent of the lake in antiquity (Dillane 2010). This study is enclosed within a 2 km area, between East Sugar Island, Serpent Mounds, and Harris Island.

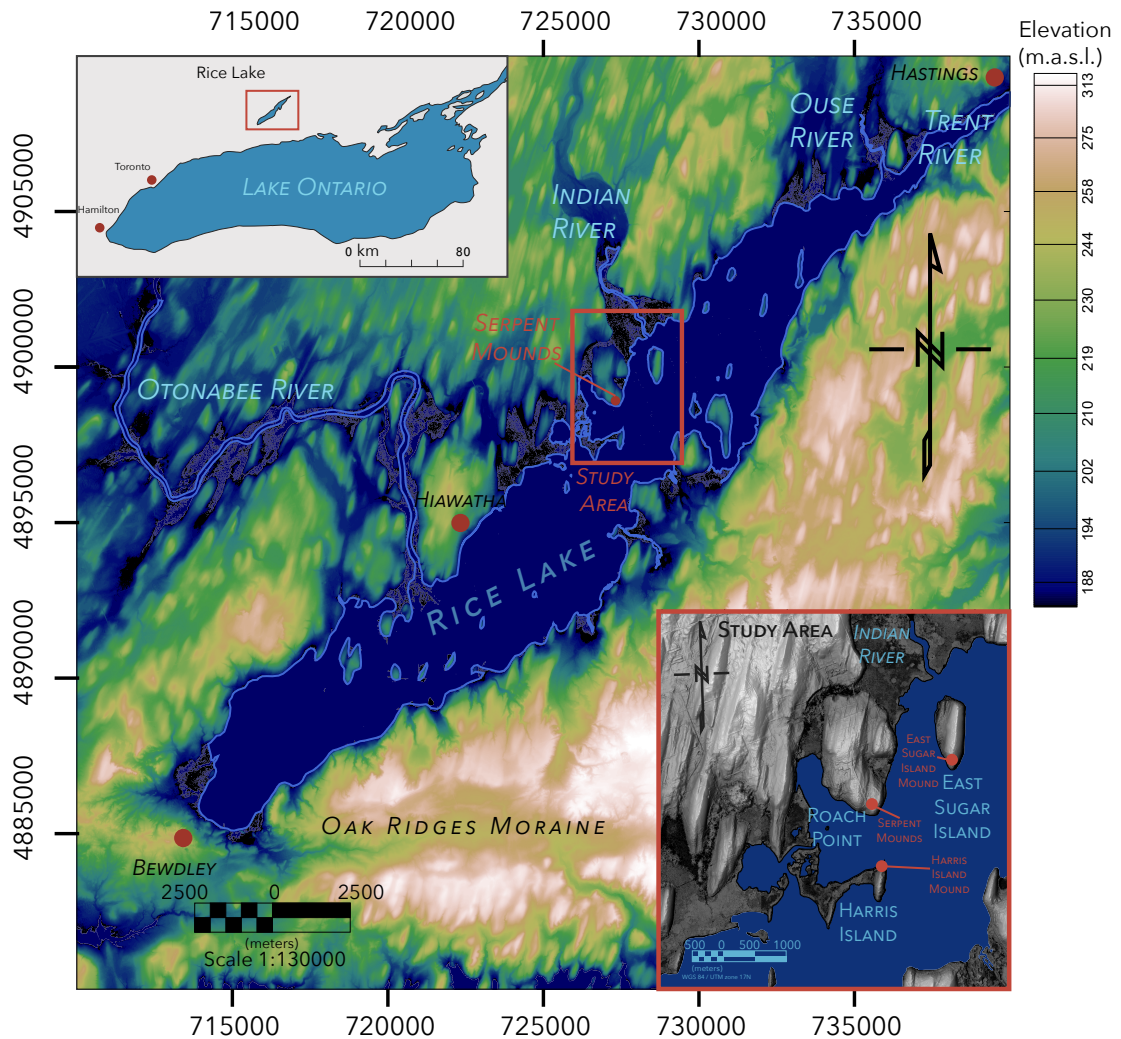


Figure 1.3: LiDAR digital terrain model (DTM) of the Rice Lake area (MNR 2018). Rice Lake is located at the southern extent of the Peterborough drumlin field.

1.3.2 Previous Work

The changes in the Holocene water levels and paleoenvironments of Rice Lake have been documented in a number of previous studies (McAndrews 1984; Yu and McAndrews 1994; Sonnenburg et al. 2011; Sonnenburg et al. 2013). The first pollen records were published by McAndrews (1984), with a more encompassing assessment of water level and vegetation history later described by Yu and McAndrews (1994) and Yu et al. (1996). In the southwest, pollen records estimate Rice Lake, once a tamarack swamp, transitioned to become a more substantial lake from 10,000–8600 BP. Sonnenburg et al. (2012) described several phases of water level changes, including two depositional hiatuses which coincide with the greater regional trends of crustal post-glacial isostatic rebound, and the main highstand (Algonquin phase) and lowstand (Admiralty phase) of Lake Ontario (Anderson and Lewis 2012; Sonnenburg et al. 2012). Many other studies have observed these episodes, and acknowledge their role in determining viability for human habitation in the region (McAndrews 1984; Yu and McAndrews 1994; Yu et al. 1996; Yu and Eicher 1998; Lewis et al. 2005; Anderson and Lewis 2012; Sonnenburg et al. 2013; Lewis 2016). Figure 1.4 summarizes the complex water level history of Rice Lake from the Paleoindian occupations until the Hastings Dam construction.

This major transgressive phase in the southeast part of the lake, occurred asynchronously with the northeast by almost 2000 years (McAndrews 1984; Sonnenburg et al. 2013). The gradual shift in water levels produced a diverse range of environments: fringing wetlands and a resource-rich setting for the first inhabitants of Rice Lake in the Paleoindian period, evidence of whom is present in a peat deposit (9400 BP) 3 km from the present study area (Sonnenburg et al. 2011). During this time, the upland pollen assemblage transitions from a boreal spruce forest, to a pine forest, where steadily rising water levels deposit a thick (1–3m) sequence of laminated marl, observed ubiquitously throughout the basin, although varying in organic inclusions (McAndrews 1984; Yu and

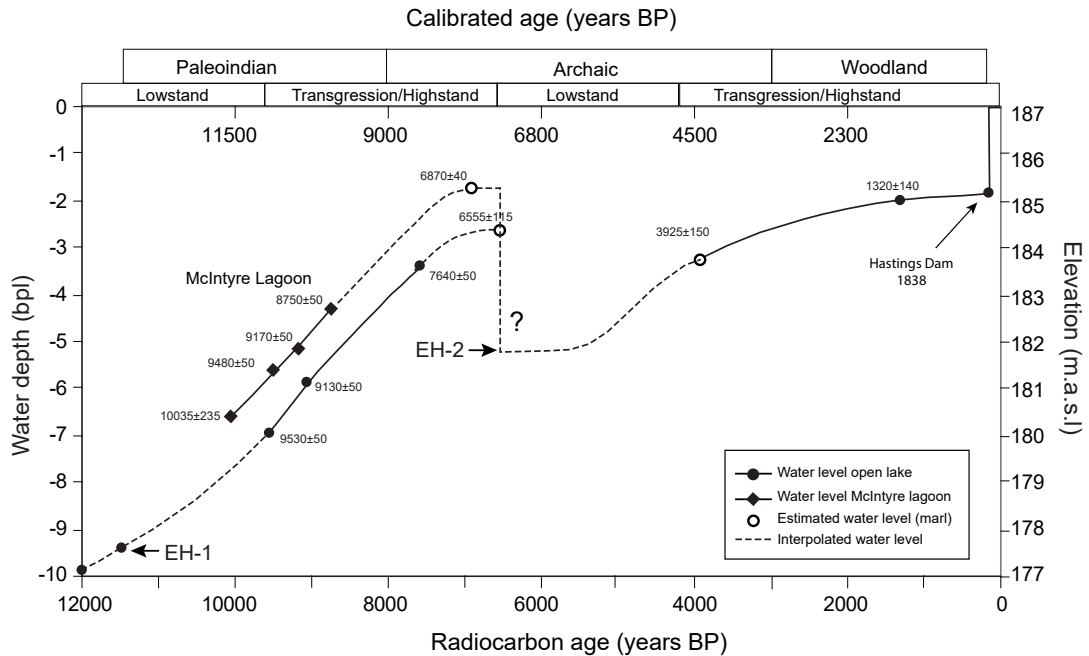


Figure 1.4: Holocene water level curve for Rice Lake and McIntyre lagoon (Sonnenburg et al. 2013). Water levels were corrected for isostatic effects.

McAndrews 1994; Sonnenburg 2010). The carbonate bedrock in the catchment of Rice Lake, acidic Mid-Holocene soils from coniferous upland forests, and an aquatic plant macrofossil assemblage dominant in *Najas flexilis*, propagated marl production (Vreeken 1981; McAndrews 1984). The thecamoebian analysis by Sonnenburg et al. (2013) show a transition to marl facies in an isolated peat bog 3km east of the present study area near the McIntyre archaeological site, dated between 9470–8760 cal BP. The marl succession, present from ca. 9000–6000 BP (Sonnenburg et al. 2011) consists primarily of *C. constricta*, which thrive in oligotrophic conditions. As noted by Wiik et al. (2013), the ability of marl to buffer eutrophication factors such as phosphorus, via co-precipitation with crystalline CaCO_3 , limit its chemical trophic status to nutrient-poor.

A second high-nutrient phase was observed following a basin-wide hiatus in the sediment record, where from the termination of the marl sequence (commonly and roughly averaged to 6000 years BP), a gap in the sediment record of 3000–4000 years

occurs (McAndrews 1984; Yu and McAndrews 1994; Sonnenburg et al. 2013). A discontinuity separates the older marl, and the overlying gyttja. The hiatus, a result of the Holocene climatic optimum (Hypsithermal), is now recognized as the marker for a distinct geological stage: the boundary between the Meghalayan and the Northgrippian Stages (Cohen et al. 2018). The very warm, dry summers that occurred in the Northern Hemisphere, generally understood to have been induced by orbital forcing, produced a period of prolonged drought, with concurrent events observed globally (Clement et al. 2000). A synchronous event has been documented as far west as Elk Lake, Minnesota (Colman et al. 2013). The loss of sediment archive was exacerbated as Rice Lake entered an isostatically-driven, hydrologically-closed phase at the time (Sonnenburg et al. 2013).

Water level recovery after erosional hiatus 2 (EH-2) (Sonnenburg et al. 2012) occurred around 3000 BP in the middle basin and at 4000 BP in the western basin (McAndrews 1984; Yu and McAndrews 1994). Applying an isobase map to the bathymetric profile of the lake, Sonnenburg et al. (2012) concluded that isostatic rebound was a significant factor in the pattern of water level recovery. It was hypothesized by McAndrews (1984) that the warm Mid-Holocene climate concurrently accelerated the depletion of groundwater through evaporative loss, and a regional transition from a coniferous to deciduous forest was less conducive to soil leaching of carbonates. As annual precipitation increased towards the end of the hypsithermal, the main basin and the McIntyre area were abundant in organic nutrients, no longer buffered by high amounts of ionic carbonate.

Following water level recovery, a thick (average 1 m) unit of gyttja is deposited on the erosional contact. The upland pollen assemblage as observed by Yu and McAndrews (1994), reflects a diverse deciduous forest abundant in Beech, Elm, Maple, and Birch, with a wetland pollen assemblage occupied by both emergent and submergent plants. McAndrews (1984) thoroughly investigated the pollen and plant macrofossil

assemblages in the vicinity of the present study area. Although his analysis mainly concerned Archaic Period archaeological occupations and exploitable wetland plants, the data provided insight towards the growth viability of wild rice, which is a known cultivar in the archaeological record (Spence et al. 1984). The period in which it flourished is estimated to have lasted from 3000 to 1400 BP (McAndrews 1984). The thecamoebian biofacies, described by Sonnenburg et al. (2013), show rapid recovery and re-establishment of the nutrient-poor species *A. vulgaris*, as the lake reconnects to the peripheral marsh areas. The lower water levels at this time left substantial marshland around Serpent Mounds and related sites on East Sugar Island and Harris Island, which, if not traversable on-foot, were certainly easily bridged by watercraft.

In 1838 CE, the Hastings Dam construction precipitated rapid environmental changes (Yu and McAndrews 1994; Dillane 2010; Sonnenburg 2010). Water levels were raised nearly 2 m above the bedrock sill in Hastings at the northeast end of the lake, which until that point, had been the only natural flow regulator. As one of the many consequences of dam construction, remaining wild rice populations in the lake became scarce. Wild rice is particularly sensitive to large increases in water level, as it requires specific flow conditions and depth fluctuations (0.5–1m) (Finkelstein and Davis 2006). The rise in *Ambrosia* pollen as observed by Yu and McAndrews (1994), marks the onset of large-scale land clearance by European settlers, who arrived in 1820 CE, and the short burst of *C. tricuspidis* identified by Sonnenburg et al. (2013) in the uppermost gyttja is a likely indicator of dam construction.

1.4 Archaeological Background

The archaeological occupations at Rice Lake extend from the Paleoindian period (11,000 BP) through to the Woodland Period (2750 BP) (Ellis and Ferris 1990; Ellis et al. 2009;

Sonnenburg et al. 2011). One of the unique features of the Middle Woodland period was the construction of large earthen burial mound complexes (Johnston 1968). The construction of the mounds coincides with expansion of Hopewell trade networks and cultural influences in southern Ontario. The highest density of mound structures in the middle Trent Valley is on the north shore of Rice Lake (Carr and Case 2006; Walker 2015). Serpent Mounds is a substantially larger mound complex than those on neighboring islands. The Serpent burial mound structure is 60 m in length 10 m wide and rises up to 2 m above the surrounding topography. The complex is located at the southern end of Roach Point (Johnston 1957; Johnston 1979). Several other oval-shaped burial mounds are also present at the Serpent Mounds site, adding to its complexity (Fig. 1.6).

The bay above which Serpent Mounds sits, is ringed by several contemporaneous sites: East Sugar Island (BbGm-11), with several burial structures and a coastal shell midden to the west, and Harris Island (sites BbGm-3 and BbGm-27), with a mound, midden, and other site components south across the water (Curtis 2002; Curtis 2014). One additional mound at the Rainy Point site (BbGm-4) is also located on Harris Island, but facing to the south, across the modern lake (Fig. 1.5) (Richardson 1968).

While the highly visible burial mound structures that dot the landscape of the Middle-Trent Valley have been subject to years of looting and have been the primary focus of many archaeological excavations, shell middens, containing a substantial volume of ceramic and faunal material, have been relatively undisturbed (Johnston 1968; Curtis 2002; Dillane 2010; Walker 2015). In fact, the site identified at Prison Island (BbGm-34), was described as an apparent large shell midden by Richardson (1968), but was ultimately left untouched following test excavation due to water infiltration and poor quality of artifacts. While overlooked, this site could prove far more significant in the context of Rice Lake's shoreline evolution, given that a larger area would have been exposed in the pre-Hastings landscape. The shell midden at Serpent Mounds is no different in that

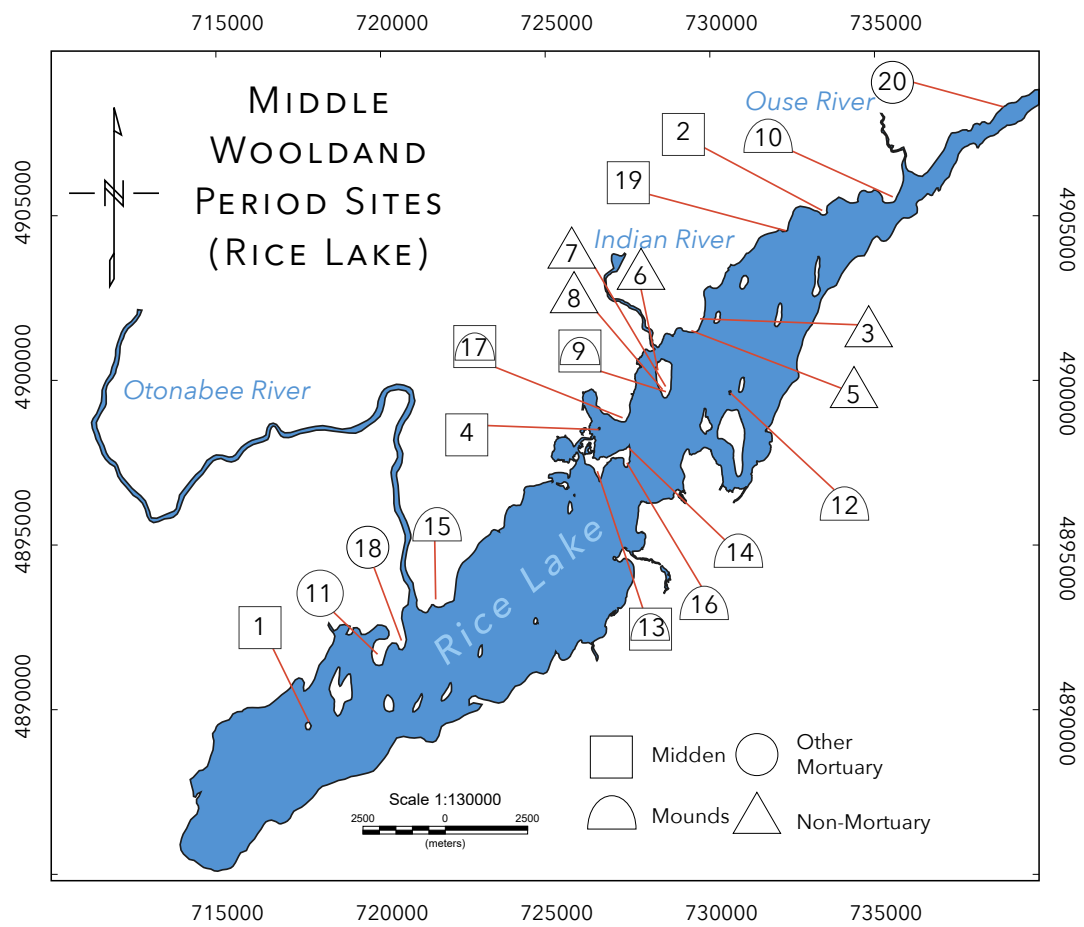


Figure 1.5: Map of Middle Woodland Period sites on Rice Lake related to the Point Peninsula occupations. Site numbers are referenced from Table 1.1 (Data compiled from Ontario Ministry of Tourism, Culture, and Sport (2016))

Table 1.1: Middle Woodland period sites at Rice Lake, with Borden identification and site contents. Index numbers correspond to locations on the map of Fig. 1.5

Index	Borden Number	Site Name	Contents	Sources
1	BaGn-7	West Grape Island	Midden	Richardson (1968)
2	BbGm-13	Spillsbury Bay	Shell midden	Richardson (1968)
3	BbGm-14	Foley Point	Described as village	Richardson (1968)
4	BbGm-34	Prison Island	Large shell midden	Richardson (1968)
5	BbGm-6	Loucks Point	Multi-component	Johnston (1968)
6	BbGm-22	Poison Ivy	East Sugar Island Complex	Johnston (1968)
7	BbGm-23	Island Centre	East Sugar Island Complex	Johnston (1968)
8	BbGm-20	Corral	East Sugar Island Complex	Johnston (1968)
9	BbGm-11	East Sugar Island	Mounds and Shell Midden	Johnston (1968)
10	BbGm-1	Cameron's Point	Mound group	Kenyon (1986)
11	BaGn-8	Cow Island	Multiple burials	Roberts (1978)
12	BbGm-9	East Grape Island	Mound group	Johnston (1968)
13	BbGm-3	Harris Island (West)	Mound and Midden	Roberts (1978)
14	BbGm-27	Harris Island Mound	Mound	MTCS (2017)
15	BaGn-2	Miller Mound	Mound group	Kenyon (1986)
16	BbGm-4	Rainy Point	Mound	MTCS (2017)
17	BbGm-2	Serpent Mounds	Mound group	Johnston (1968)
18	BaGn-3	Jubilee Point	Multi-component	Curtis (2002)
19	BbGm-12	Godfrey Point	Midden	MTCS (2017)
20	BbGm-24	Scriver	Burials	MTCS (2017)

respect (Johnston 1968; Ellis and Ferris 1990). Shell middens are not uncommon at Rice Lake, with several others at sites on the mouths of the Indian and Otonabee rivers. Inquiries regarding the function of these sites have been intensively explored: whether for long-term occupation with relatively few individuals, short term feasting episodes with many participants, or the product of prolonged ritual activity associated with funerary traditions at the mounds (Spence et al. 1984; Ellis and Ferris 1990; Wilson 1993; Curtis 2002; Dougherty 2003; Dillane 2010; Curtis 2014).

At Serpent Mounds, the shellfish content of the midden consists entirely of two species: *Elliptio complanata* and *Lampsilis radiata 'siliquoides'*, with other faunal remains limited to the long-bones of deer, and a non-faunal excess of ceramic refuse (Johnston 1968; Dillane 2010). The lack of *Anodonta grandis* agrees with the descriptions of Rice Lake's Woodland Period shoreline, discerned by Sonnenburg et al. (2012). In absence of this species, the harvested shells reflect a riverine or deltaic or shallow lake habitat

(Johnston 1968; Clarke 1981). These middens, and the activity of shell harvesting are essential to the notion of the mounds as territorial markers, as suggested by Dillane (2010).

As populations expanded during the Middle Woodland period, the abundance of wild rice stands and the shellfish resources would have provided impetus for asserting territorial control through visual means; this may explain why the mounds at Rice Lake are situated atop the many drumlin-islands. Dillane (2010) also remarks on the relationship of population size to the shell middens, postulating only occasional use, for years when wild rice harvests were insufficient. Otherwise, if annually used, the shell beds would quickly become depleted, given maturation times and life cycles (Clarke 1981). While the shell middens may have gradually accumulated, this does not explicitly infer that the population sizes of these Middle Woodland sites were small, rather, that the exploitation of shellfish was occasional, with a probable link to burial activity. This link is evident by the lenses of shells which were reported to line the graves in Mound “C” at Serpent Mounds (Johnston 1968).

Serpent Mounds was first excavated in the late 19th century (Boyle 1897), until the mid 20th century, with a large volume of research directed at the high density of burials within and around the mounds (Schwarcz et al. 1985; Ellis and Ferris 1990; Ellis et al. 2009). However, not all remains exhumed from the site were for academic purposes, as grave-robbing, looting, and desecration of the site was documented before first investigations by David Boyle in 1897 (Johnston 1968; Dillane 2010). A more formal investigation during the early 20th century by Henry Montgomery (1909), produced the first, albeit dubious, estimate of their age at 1000 years before that year, which was derived from observing the ‘state of decay’ in skeletal remains (Dillane 2010).

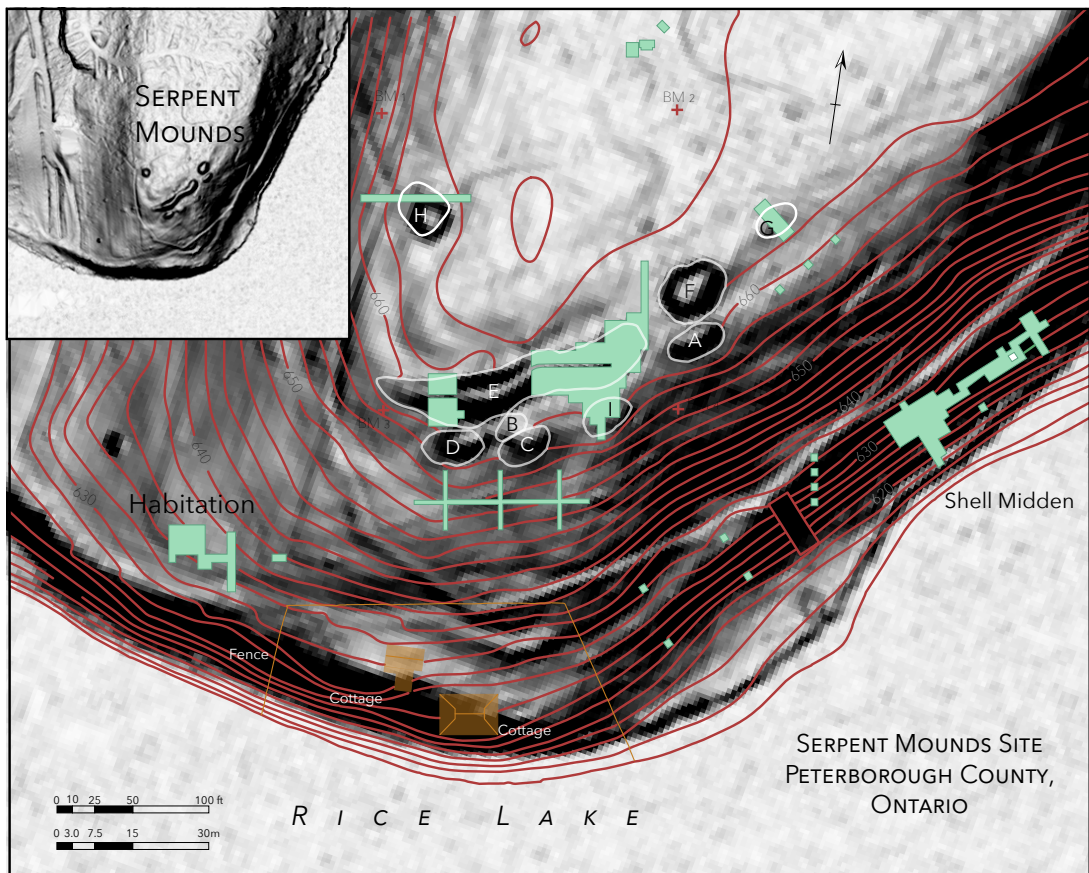


Figure 1.6: The 1968 excavation map (Figure 2 in Johnston (1968)) superimposed over a slope-shaded LiDAR map (MNR 2018), with serpent mounds visible. Contour units are in feet. Inset image is the LiDAR map without annotations

The first systematic investigations were conducted by the Royal Ontario Museum between 1950–1955 (Johnston 1968). The excavations covered a total area of 460 m, and included several mounds, as well as the shell midden near the shoreline (Fig. 1.6). Though unconfirmed, mound construction is suggested to have multiple stages, with additions appended to an original, smaller structure (Johnston 1968; Ellis and Ferris 1990). The site consists of nine mounds (A-I), one elongate shell midden, parallel to the southeastern shore, and a small habitation area to the west of the mounds (Fig. 1.7). The western habitation site, unfortunately, had been partly disturbed by agricultural activity on Roach Point, but a great many features remained intact, offering sufficient material to identify it as an Early Woodland camp (Dillane 2010). The shell midden returned a radiocarbon date from a charcoal fragment much older than the others sampled by Johnston (1968) (1355–2158 cal BP). This was taken as the oldest date for site occupation, but does not explicitly inform the age of the mounds themselves. Rather, this suggests there are possibly older burial episodes in the history of Serpent Mounds, before the oldest burials recorded from the Johnston (1968) excavations.

The initial examination of the Serpent Mounds skeletal remains, conducted by Anderson (1968), provides a thorough report of the physical anthropology, however, it was only in 1985 (Schwarcz et al. 1985), and again in 2003 (Harrison and Katzenberg 2003), that any sophisticated analyses were performed to address diet using stable isotopes. In addition, several new radiocarbon dates were produced, which aligned to the mound chronology of Johnston (1968). Katzenberg (2006) acknowledges maize was, in some capacity, a dietary component at Serpent Mounds from carbon isotope analysis of remains within Mound E (the Serpent). Although, the origin of this signal may have been introduced from trade as opposed to horticulture (Dillane 2010). Unfortunately, no study has noted shellfish as being substantially consumed. Ultimately, a comparison between the Serpent Mounds burials and remains from a group of adjacent Late Woodland Iroquoian ossuary pits (Johnston 1979) show a chronological move towards

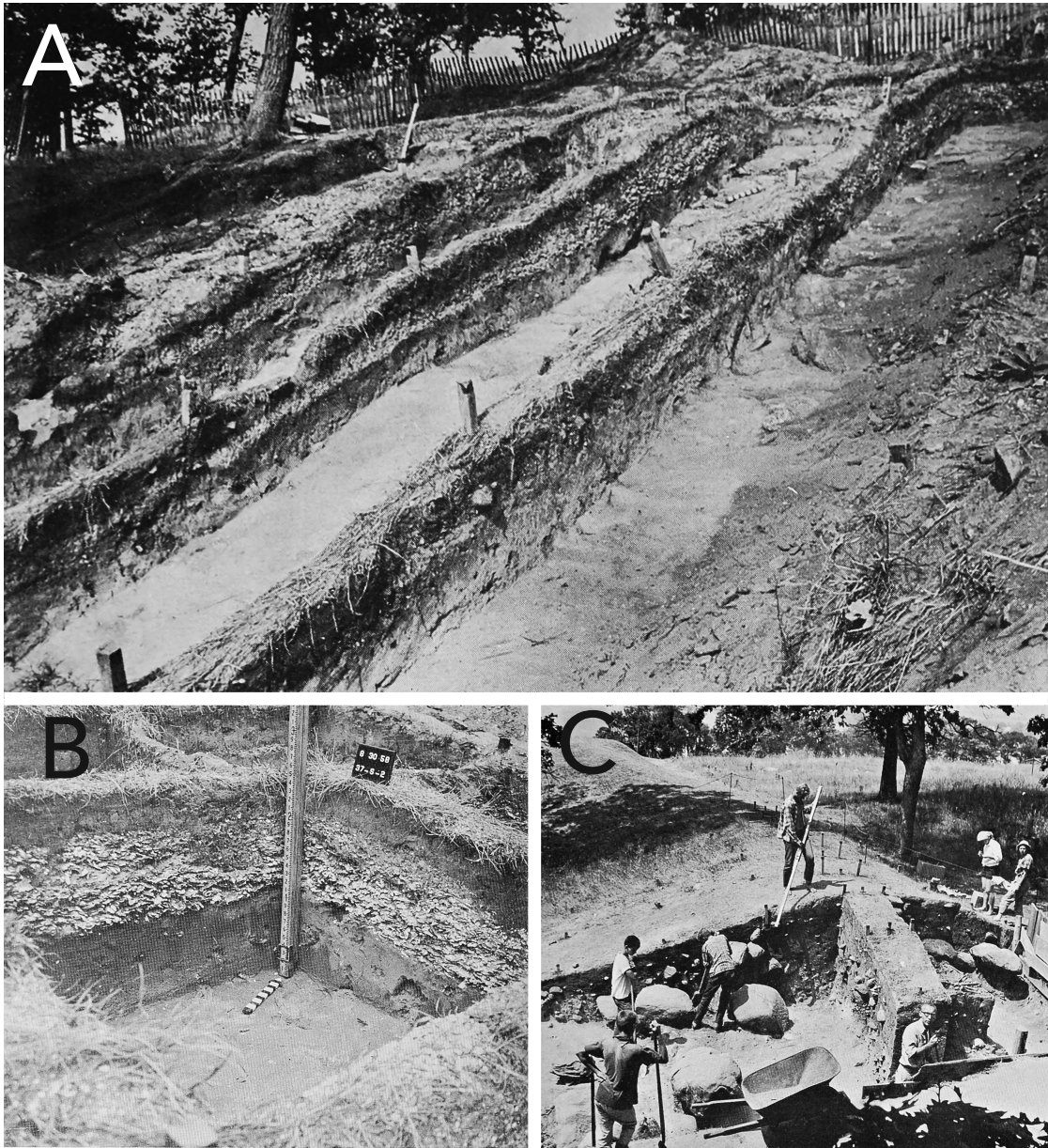


Figure 1.7: **A.** Down-slope profile of the shell midden through excavation transects (Plate 50 in Johnston (1968)). **B.** Typical shell midden stratigraphy (Plate 48 in Johnston (1968)). **C.** Excavation of Serpent Mounds (Plate 5 in Johnston (1968)).

a maize-dominated diet by 1000 AD. This dietary shift between populations, and different cultures, coincides with the decline of extensive wild rice marshes near the McIntyre Site (BbGn-2) observed by McAndrews (1984), and the eventual discontinuation of mound construction at Rice Lake. Dillane (2010) suggests this subsistence change made the mounds unimportant for territorial control of once-exploited wetland resources.

Despite what is known of Rice Lake's climate history (Yu and McAndrews 1994; Yu et al. 1996; Sonnenburg et al. 2013), no study has addressed the environment in a Middle Woodland archaeological context. Given that terrestrial excavation is no longer an option at Serpent Mounds, it is imperative that remote sensing, and peripheral geophysical and geoarchaeological techniques are implemented if more is to be discovered about this ancient monument. The view-shed analysis performed by Dillane (2010) attempted to reconstruct visibility parameters of several Rice Lake mounds using limited paleogeographic data, and synthesized many previous theories regarding the purpose of the mounds in the context of territorial markers (Johnston 1968; Spence et al. 1984; Wilson 1993; Dougherty 2003). However, one overlooked element of the GIS models, was the use of an intermediate vegetation parameter, accounting for potential land clearance. Visibility was instead tested under total vegetation, and no-vegetation coverage instances. Understanding the extent of land clearance in mound construction and site occupation is needed to discern how these sight-lines could have been augmented.

1.5 Methods

1.5.1 X-ray Fluorescence (XRF) and Core Scanning

Chemical analysis using X-ray fluorescence (XRF) has long been a favoured method of analysis for its rapid elemental characterization of samples, bridging many fields, both

commercially and academically (Van Grieken and Markowicz 2001). The principles of XRF are simple: within an evacuated X-ray tube, electrons are fired from the cathode towards an anode of a pure metal where they decelerate on interaction with the electromagnetic field of the encountered atomic nuclei. The deceleration of these charged particles produces Bremsstrahlung (“braking radiation”), which forms the continuum spectra of measured X-ray intensity, and is projected towards the sample surface (Beckhoff et al. 2007). The Bremsstrahlung X-rays interact with and excite the inner-shell electrons of the sample. An electron from a higher orbital will descend to fill the void, causing fluorescence, and the emission of characteristic X-rays, which adhere to the general principles of ionization energies. The emission spectra unique to each element, is represented by *K*, *L* and *M* shells (ionization energy in KeV decreasing respectively), with the energy intensity of each *K*, *L* or *M* ‘line’ represented by the suffix α , β , and γ (greatest to least detectable energy, respectively). An exhaustive description of XRF physics can be found in Beckhoff et al. (2007).

In XRF spectroscopy, two analysis methods are commonly employed: energy-dispersive (ED-XRF), and wavelength-dispersive (WD-XRF). In ED-XRF, all spectra are simultaneously collected from the sample emissions, such that all peak area energies are stored, without a significant degree of mechanical filtering, which WD-XRF achieves through the use of an intermediate crystal and monochromator. ED-XRF allows a large volume of spectral data to be expediently collected for most elements, at the expense of significant overlap in line intensities (Beckhoff et al. 2007). WD-XRF, conversely, mechanically orders the emitted X-rays into characteristic wavelengths, negating spectral overlap, but at a much slower analysis time, and has an elemental range which is limited to the crystal employed for wavelength analysis. For this reason, WD-XRF, although more quantitative, is not incorporated in μ -XRF-CS.

The rapid analysis provided by ED-XRF is ideal for many applications in geoscience

and has enabled the development of XRF scanning technology. The acquisition of thousands of chemical measurements allows the analyst to progress beyond conventional sediment core interpretation, and offers a sample resolution unattainable through manual techniques (Croudace and Rothwell 2015b). XRF core scanners have been used to explore paleolimnological records for over a decade, and are invaluable to high-resolution sediment analysis, but the devices are far from flawless. A multitude of issues persist regarding processing and quantifying inherently semi-quantitative XRF data through calibration. First among these is the achievable limit of energy that may be directed at the sample: the Duane-Hunt limit (Beckhoff et al. 2007). Thermodynamics regarding the limit of Bremsstrahlung energy, and the detection of elements are described by Jarvis et al. (2015). The anode tube selected also determines the range of detected elements, and suffers from shifts in measurement accuracy with tube age, which is investigated thoroughly by Ohlendorf et al. (2015). In this study, a Cr anode tube was selected for its good detection of light elements which may coincide with anthropogenically induced erosion.

Other obstacles to the analyst come in the form of scattering, which are measured by the Itrax core scanner as inelastic (Compton or incoherent) and elastic (Rayleigh or coherent) particle interactions. Hoffmann (2006), Boyle et al. (2015), Jarvis et al. (2015) and Rothwell et al. (2015) provide an encompassing description of the nature of scattering, and how it impacts the acquisition and interpretation of core scanner data. In addition to scattering, it is also critical to discuss peak artifacts common to XRF: internal fluorescence, sum, escape, and diffraction peaks. The former of these is less an issue with modern semiconductors. These scattering parameters are measured by the Itrax, and must be corrected for in the process of data-fitting and batch analysis. The Itrax core scanner maintains a constant distance from the target, with consistent measurement width, mitigating many of the issues regarding differences in measurement values from varying sensor elevation (Croudace and Rothwell 2015b; Cuven et al. 2015).

Acknowledging the underestimated shortcomings of XRF is an essential preamble to the core scanning methodology employed in this study. In many cases, calibration of core scanner data is becoming frequently utilized (Weltje and Tjallingii 2008; Lyle et al. 2012; Weltje et al. 2015), but the nature of this study does not require quantification of data.

1.5.2 Itrax μ -XRF Core Scanner

Elemental analysis was conducted using an Itrax core scanner (Cox Analytical Systems). Its capabilities include μ -XRF, with a minimum 200 μm step size (at a 0.2 mm \times 4 mm surface area), millimeter-scale magnetic susceptibility, high-resolution 16-bit optical imagery (47 $\mu\text{m pixel}^{-1}$), and line-scan X-radiography, producing radiographs at 20 μm resolution. The sample bed can accommodate a split sediment core, up to 1.8 m in length, progressing through the machine via leadscrew to achieve small step sizes with a minimum number of moving components. All instruments are housed in a central tower, and remain stationary with the exception of z-axis elevation control for the flat-beam scanning head. Further information on the scanner configuration can be found in Figure 2 of Croudace (2006). The sensor used by the Itrax is a 1024-channel silicon drift detector (SiDD), which has the dual benefit of low mechanical noise, and peltier cooling, as opposed to liquid nitrogen cooling (Croudace 2006). 16-bit high-resolution .TIF images were used for image analysis in this study, and processed for improved visibility. Effectively, at a maximum resolution of 47 $\mu\text{m pixel}^{-1}$, sedimentary features are resolved at a scale which surpasses that of conventional core logging. Default power settings were set for each core scan, based on a single measured point within the gyttja of each split sediment core, and optimized to limit variability between scans. The energy response was tuned to the gyttja, avoiding the top area of the core, where pore-water attenuation of X-rays would be problematic. Settings were fine tuned and measured

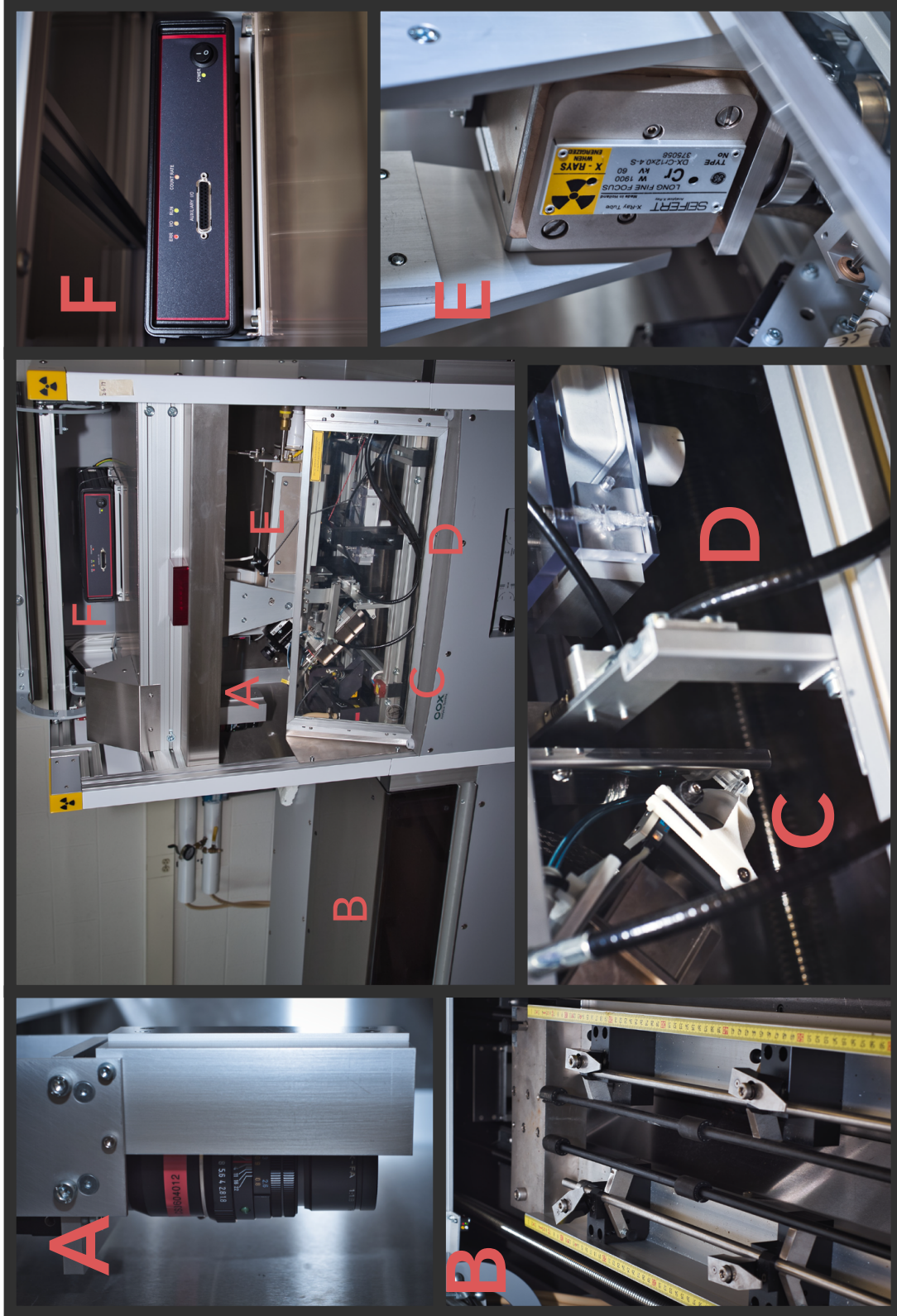


Figure 1.8: The Itrax multi-parameter sediment core scanner by Cox Analytical Systems: A. Lens for line scan CMOS image sensor. B. Loading bay and bed for split sediment cores. C. Flat-beam scanning port and sensor assembly for XRF. D. Bartington MS-3 magnetic susceptibility probe. E Cr X-ray anode tube. F. Digital X-ray processor.

against a background reading to establish an acceptable output count rate (OCR) prior to scanning .

1.5.3 μ -XRF Key Elements and Matrix Effects

Two suites of elements were selected from the raw spectra of each core: one representing elements of terrigenous origin, and one for organic productivity, represented by a combination of biogenic and authigenic mineralizations.

1.5.3.1 Terrigenous Elements

Elements most easily indicative of runoff events, are those associated with minerals which either have low mobility, or no primary origin within the catchment. Al, Fe, Ti, K, Si, and Zr are ideal for this reason (Cuven et al. 2010; Kylander et al. 2011; Moreno et al. 2011; Arnaud et al. 2012; Balascio et al. 2015). Although Al was not recorded with sufficient signal strength to be viable in this study, Ti provides an equivalent conservative alternative. Ti, commonly derived from titanomagnetite minerals (Marshall et al. 2011), is largely non-reactive following transport into the lake, making it preferential for use as a denominator when expressing ratios of elemental abundances (Koinig et al. 2003; Boës et al. 2011; Löwemark et al. 2011; Shala et al. 2014; Chawchai et al. 2016). This works well for normalization purposes, and in doing so, other elements are effectively normalized to a primary sediment contributor. Complications may arise, however, when Ti shows a strong covariance to other elements, which indicate runoff, where a ratio between the two will be less informative. K is a common indicator of clay minerals (Cuven et al. 2010; Cuven et al. 2011), found in association with finer-grained sediments (Chawchai et al. 2016). Fe, although commonly used as a terrigenous input indicator, may become convoluted due to its essential role in biological systems, and in

redox activity, commonly associated with Mn (Lyle et al. 2012; Chagué-Goff et al. 2016). In lakes, Fe is often found in the sulfide mineral pyrite (FeS_2), which may be an indicator of organic productivity, and thus warrants caution for use as a terrigenous input indicator (Chagué-Goff et al. 2016). Before progressing to any advanced statistical analyses, all elements should be represented in some form of correlation matrix, to discern relationships prior to assigning a linkage to environmental process. Si has also been used as an accurate representation of grain size, and detrital input (Marshall et al. 2011; Chawchai et al. 2015; Chagué-Goff et al. 2016). It has also been a useful indicator of biogenic silica production, tracking organic productivity of lakes (Brigham-Grette et al. 2013). This overlap between proxies is problematic if the intent of using an XRF proxy relies on the signal having a discrete origin. Chawchai et al. (2016) stress the importance of independently testing proxies where overlap in source material is concerned with XRF data.

At their study site in a tropical, organic-rich lake, the Si/Ti ratio was observed to be mainly driven by sand-sized particles, and less by the percentage of biogenic silica. It was rationalized that the sand, composed of quartz and plagioclase grains, were substantially larger than the phytoliths and diatom frustules, and thus have a higher likelihood of detection during scanning. Zr, although somewhat low in abundance in the Rice Lake cores, is a strong indicator of flooding surfaces, and coarser-grained material, with favourable conservative properties (Boës et al. 2011; Chawchai et al. 2016). Ideally, Zr will track the transgressive horizon covering the marl/gyttja contact observed ca. 4000–3000 years BP. This is hypothesized, as the transgressive horizon, usually removing a small amount of material from the sediment, will often produce a fractionation effect on the grain size of the sediment. Minerals which are heavier, like detrital zircon, will be left behind as a geochemically identifiable lag deposit, physically observed as a lens of coarse-grained material (Cuven et al. 2010; Cuven et al. 2011; Marshall et al. 2011).

1.5.3.2 Organic Productivity Markers

Elements, such as S, Sr, Ca, Ni, and the ratio of Compton to Rayleigh scattering (inc/coh), are often used to represent biological productivity, and endogenic mineral production (Koinig et al. 2003; Martín-Puertas et al. 2011; Foerster et al. 2012; Elbert et al. 2013). S may represent a variety of processes in organic-rich settings like Rice Lake. It may be an indicator of increasing biological productivity, strongly associated with Fe during Pyrite formation (Moreno et al. 2007), or it may indicate the precipitation of evaporitic sulfates (gypsum) (Martín-Puertas et al. 2011). It is critical that S and Fe be tested at the very least in a correlation matrix, to test for the strongest element associations, whether to Fe, or Ca and Sr. The generation of Sr and Ca, is dependent on sediment type and associated environment in the case of Rice Lake. Sr and Ca are likely components of authigenic minerals in the marl unit (Burn and Palmer 2014), which precipitate as carbonate and sulfate minerals during periods of drought. In the gyttja, however, both Ca and Sr are delivered primarily through runoff. Moreno et al. (2007) and Kylander et al. (2011) confirm there is a strong change in the correlation coefficient between Ca/Ti and Sr/Ti, dependent on lithology, related to higher or lower water levels at their respective study sites. Sr may be present as a co-precipitate in CaCO₃ as aragonite, or in events of high carbonate saturation and lower water levels, as strontianite (SrCO₃). In contrast, heightened water levels, and thus dilution of carbonates, showed a stronger correlation of Sr to allochthonous elements (Kylander et al. 2011). The marl deposits of Rice Lake contain a substantial number of shelled organisms (ostracodes, gastropods, etc), which incorporate calcite and aragonite as a structural material, and contribute these elements to the sediment record without the necessity of carbonate-saturated lake water (Sonnenburg et al. 2013).

Ni was difficult to frame within the context of Rice Lake, as it is usually associated with mining byproducts and other contaminants (Lintern et al. 2015). In the absence of

human industry, and a feasible bedrock source, Ni is commonly found as a micronutrient in all higher-order plants, essential to many enzymatic processes (Brown et al. 1987; Hänsch and Mendel 2009; Yusuf et al. 2011). Furthermore, an XRF-based study of metals in aquatic plants from Chuparina and Azovsky (2016) point to higher accumulation of Ni when compared to terrestrial plant reference materials for XRF. In this study, Ni was observed in abundance during periods of low terrigenous input, but it is uncertain whether μ -XRF-CS is capable of detecting Ni from plant matter, and has never been assessed for this purpose. A more likely scenario, and one which adheres to the observed relationship between Ni and high organic productivity, is the adsorption of Ni to organic colloids or calcite in the sediment.

Ni interaction with aqueous CaCO_3 crystal lattices show Ni-hydrates do not co-precipitate as other metals (Mn and Co) do, but will remain a hydrated adsorbed compound until they are incorporated in solid solution via calcite re-crystallization. Alternatively, heterogeneous precipitation occurs when aqueous metal concentrations, maintained by surface-exchange reaction, exceed the ion activity product of the Ni adsorbent (Zachara et al. 1991). This is significant for explaining correlation of Ni and Ca within marl lithofacies, as Ni abundance should increase proportionately to Ca.

As a proxy for organic matter, the inc/coh (ratio of Compton to Rayleigh scatter) values from each scan track the change in light elements (specifically, organic carbon) according to Moseley's Law. Several studies have positively correlated this proxy to total organic carbon (TOC) (Burn and Palmer 2014; Chawchai et al. 2016).

1.5.3.3 Matrix Effects

As XRF data is semi-quantitative, it carries significantly less interpretive weight when the water content, scattering factors, tube aging, and changes in lithology are not considered. A thorough review of these issues was conducted by Ohlendorf et al. (2015). The findings show that tube aging, and sediment heterogeneity (in water content, organic matter, and grain size) were the greatest contributors to the issue of measurement inconsistency and signal loss in long sediment core records. These can be corrected for easily in shorter sequences, under the condition these measurements are normalized to instrument parameters, or element ratios are used.

Several methods have been popularly implemented to address the issue of sample inhomogeneity and instrument error, conveniently using parameters provided in the Itrax data output. Data are often normalized to the coherent scatter (Ladwig et al. 2017; Poraj-Górska et al. 2017), the incoherent scatter (Marshall et al. 2011), the sum of the incoherent and coherent scatter (Kylander et al. 2011; Berntsson et al. 2014; Berntsson et al. 2015), and the counts per second (cps) (Bouchard et al. 2011; Shala et al. 2014; Chagué-Goff et al. 2016).

As organic-rich sediments comprise the majority of sediment analyzed at Rice Lake, water content and organic matter must be accounted for. Thus, all data is normalized to the incoherent scatter prior to visualization. To separate any variations in chemical trends resulting from lithological contrast between carbonate-rich marl, and gyttja, all statistical operations are performed on a dataset representing the full core, and the gyttja, following the rationale of Schreiber et al. (2014). The isolated gyttja data contain the chronological period of interest for this study, and if subtle trends are to be revealed therein, a comparison between the full core and gyttja data must be made.

1.5.3.4 Post-processing of Spectra

Before analysis, raw spectra must undergo further processing to ensure accuracy, and is done so through the Q-Spec software package provided with the Itrax core scanner (Croudace 2006). Peak fitting using Q-spec is performed through a batched, iterative procedure, where n iterations are made, stopping once the minimum mean squared error (MSE) has been achieved (Ohlendorf et al. 2015).

In this study, the sum-spectra of all measurements in a core scan were used for peak-fitting procedures, and the number of iterations was set to 100. The inclusion of contrasting lithologies was unavoidable, and the marl-gyttja interface was of interest for the purposes of paleoclimatic reconstructions. The sum-spectra file was chosen out of compromise, although the sensitivity defaults of the Itrax were always set within the gyttja. The objective of the fitting procedure is to reduce the MSE of each measurement.

The process of batch analysis requires a suite of elements be added or removed in order to place a line of best-fit close to the fluorescence peaks of the desired elements. Elements with a total count across all measured samples of 0 to ≤ 1000 were removed, and elements which were observed to improve the fit of target elements in this study, were added. Inclusion of tungsten (W) accounted for W fluorescence peaks, which originate in the filament of the X-ray tube, and intensify with tube age (Ohlendorf et al. 2015). As a final step, the sum and diffraction peaks were accounted for in the batch analysis procedure, adjusting until optimal MSE was achieved (arbitrarily < 2). Including spectral artifacts accounts for unfit peaks which cannot be improved through the adjustment of Q-Spec parameters (Croudace 2006; Rodríguez-Germade et al. 2015).

1.5.4 Bathymetry Surveys

Single-beam sonar was previously employed by Sonnenburg et al. (2012) at Rice Lake, and using the same methodology with finer line spacing, was used to map the study area. The new digital bathymetric model (DBM), provides a detailed bottom profile adjacent to Serpent Mounds, revealing submerged features, which may have been exposed during the Early and Middle Woodland period. Interpreting these features is critical to the strategic selection of core locations. Bathymetry-informed coring ensured sampling was conducted in areas which likely experienced continuous sedimentation, even during the Mid-Holocene Hiatus.

Mapping was carried out in calm-water conditions using a Knudsen 320BP single-beam echosounder with a 200 kHz transducer, which produces an 8° conical beam at a width of 1 cm. This transducer was mounted on a pontoon craft, with a Trimble Ag132 differential GPS system, synchronized to the ping rate of the transducer for accurate positioning. sonar data were processed using Geosoft Oasis Montaj, where measurements were corrected for transducer draft, and heightened water levels on Rice Lake at the time of sampling (Parks Canada Water Management InfoNet, 2018). Processing followed the guidelines of Sonnenburg and Boyce (2008), with additional tie-line levelling to the survey data of Sonnenburg et al. (2013) (Fig. 1.9), for enhanced bottom visibility for the 2 km² area adjacent Serpent Mounds. The sonar data was overlapped by a 2 m resolution SCOOP DTM from MNR (2013), to which a 3-pass Hanning filter was applied for interpolation artifact removal.

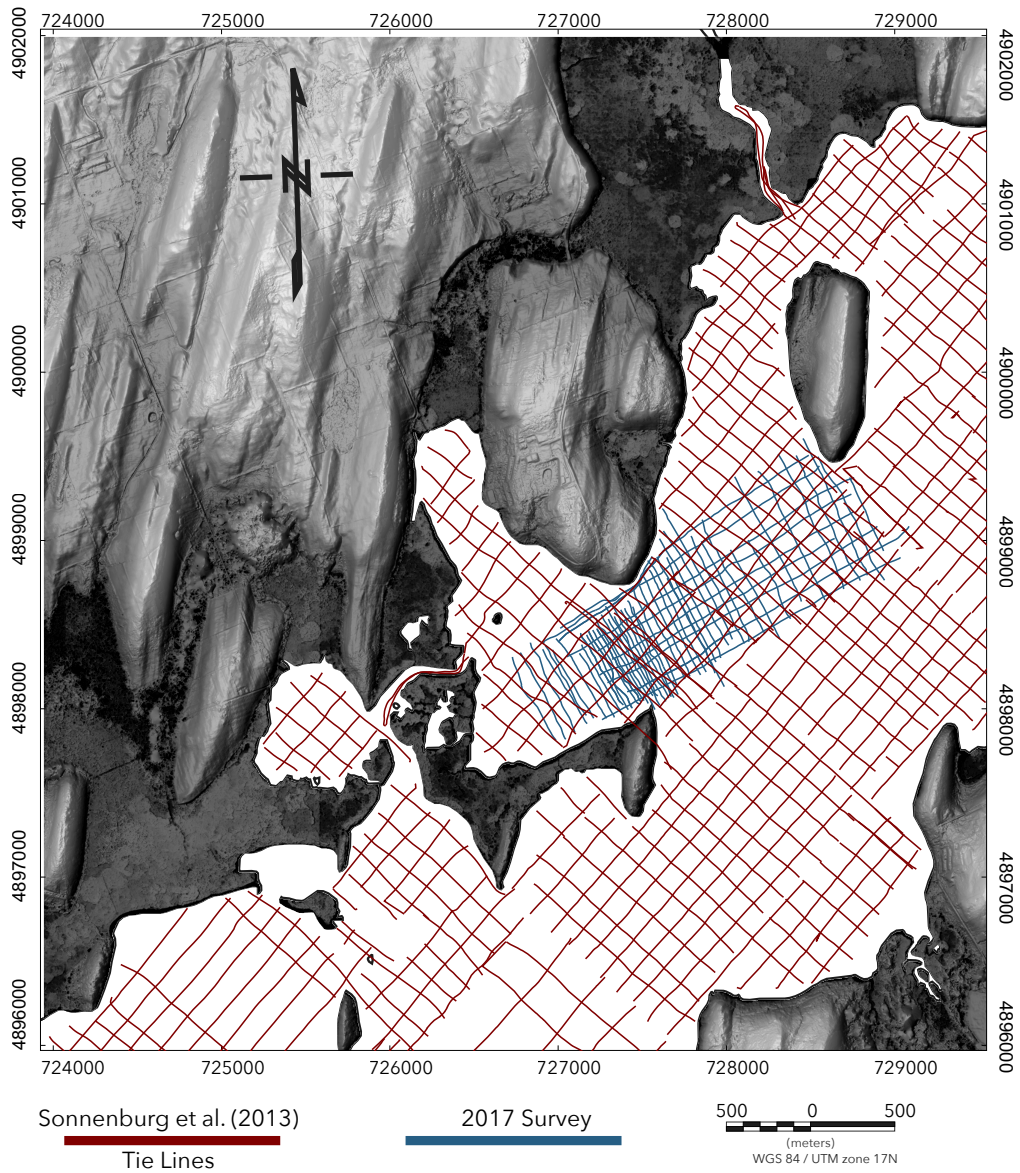


Figure 1.9: Survey lines for the sonar data used in this study, including new lines, and those from (Sonnenburg et al. 2013). Terrestrial component of map is a 2 m resolution DTM from the 2013 South Central Ontario Orthophotography (SCOOP) survey (MNR 2013)

1.5.5 Core extraction, sampling, and analysis

12 cores (1–2.5m length) were extracted using a combination of 10 percussion cores and two vibrocores. The polycarbonate percussion cores (68 mm diameter) were extracted using an Aquatic Research Instruments universal percussion device, and the aluminum vibrocores (70 mm diameter) were extracted with a gas-driven vibrocorer. The cores were cut into 1 m lengths for transport, with percussion cores extruded into plastic troughs on-site. Cores were halved in-lab, with percussion cores sampled every 5 cm for 5 cm³ volumes, at 1 cm widths, as one half was unable to be preserved to the same quality as the archive. SRPM-02 and SRPM-12 were sampled at 2.5 cm intervals for 1.25 cm³ volumes, at a sample width of 0.25 cm. Vibrocores were split into archive and working halves and all cores were stored at 5 °C to inhibit microbial growth, and preserve the cores.

A total of 11 radiocarbon samples were sent to A.E. Lalonde accelerator mass spectrometer (AMS) lab in Ottawa for dating. Samples were chosen to avoid hardwater and old-wood effects, and included mostly leaves, and seeds from discrete depths from five cores. Processing of radiocarbon samples followed the protocols of Crann et al. (2017).

1.6 μ -XRF Data Processing and Analysis: PyTrax

The large data output generated by the Itrax is difficult to manage with conventional spreadsheet software, and requires a specialized approach to improve efficiency. Very few software packages tailored to μ -XRF-CS exist, many lacking integration of rigorous statistical analysis (Schlolut et al. 2012; Croudace and Rothwell 2015a). This is fortunately beginning to change, with the introduction of combined calibration and statistical packages like Xelerate (Weltje and Tjallingii 2008; Bloemsmas 2015; Weltje et al.

2015). In the past decade, core scanner studies are put to more rigorous standards for data processing, and require more than just the display of raw counts to be acceptable for publication (Weltje and Tjallingii 2008). Incorporation of data normalization, calibration, and multivariate analyses like PCA and CA are imperatives for robust Itrax data analysis (Harff et al. 2011; Schreiber et al. 2014; Shala et al. 2014; Weltje et al. 2015; Chagué-Goff et al. 2016; Chawchai et al. 2016; Ladwig et al. 2017; Poraj-Górska et al. 2017).

At its core, PyTrax offers data visualization with minimal preparation required from the user. This has evolved to incorporate automated facies identification through the use of PCA, CA, and image analysis functionalities. Several Python libraries in the Anaconda distribution (Continuum Analytics) are used, including: Pandas (McKinney 2015), Pillow (Python Imaging Library Fork) (Clark et al. 2010–), Matplotlib (Hunter 2007), SciPy (Jones et al. 2001–), Scikit-Learn (Pedregosa et al. 2011), and Seaborn (Waskom et al. 2014). While lacking a user interface, the implementation of this code has enabled a great deal of flexibility in the treatment of Itrax core scanner data. The order of operations are simple, and are designed to visualize data with minimal user interference.

PyTrax automatically reads the metadata, results, and image files from three respective folders, and is designed to process and concatenate multiple scans of long sediment records, without the need for user intervention. The image files, if chosen to be displayed, are cropped with to-the-pixel accuracy based on the millimeter equivalent of the image height (in pixels), aligned to the start and stop of the XRF data, eliminating the need for manual alignment. Images may be adjusted to user specifications in any photographic post-processing software, but do not require cropping. The images are scaled using a Lanczos interpolation, when specific viewing windows are stratigraphically selected.

Improving upon one of the features of RediCore, the native visualization software

for the Itrax, a dataframe of RGB pixel data is produced in PyTrax when the final image is compiled. A narrow window (1000 pixels for high-resolution images) along the middle of the core is used to eliminate non-sediment areas of the image. The user decides whether to use the mean, median, or mode of the red, green, and blue channel values, which are read from each row to provide a single value for each channel. A moving average is then applied down-core to a desired window and aligned with the Itrax data. Further image analysis can be obtained through the application of PCA, which through the first principal component, as demonstrated in Chapter 2, will provide a relative value of image brightness. These data may then be clustered, which has the potential to break clusters along lithological boundaries, and is available in the dataframe representation of the image.

PyTrax can support any number of displayed elements, and if no elements are specified, will plot all elements present in the provided result files. A moving average may also be plotted to a user-specified window, and is displayed over the elemental spectra. Processing and basic mathematical operations (sum, difference, product and quotient), with additional automatic calculations of the incoherent/coherent ratio, and sum (incoherent + coherent) of scattering parameters can be used for data normalization. Many other normalization options are readily available, such as normalization to the counts per second (cps), logarithmic transformation, or normalization to any element desired by the user on a per-element basis, or for all elements under consideration.

Filtering unwanted data is made easy through the implementation of Boolean arguments, where the user can null measurements from a specific depth, value, or range thereof. Filtering out measurements deemed invalid by the Itrax is simplified through this procedure. Data may be clipped, such that all values outside a minimum and maximum depth are nullified, which may be useful for preprocessing of data for PCA. A non-destructive re-scaling of data allows for the user to select a minimum and maximum

depth for the plot boundaries, providing discriminate viewing of core image sections with associated XRF and RGB data.

Multivariate analysis is simplified, and allows for the plotting of one set of PCA results, with associated cluster visualization, or a second paired analysis which accounts for only a specific section of the core as a comparative record (Schreiber et al. 2014). Optional plotting of a colour-mapped representation of clusters is provided, with overlapping, or separately-plotted principal component value lines. The steps for multivariate analysis used in this study are described in Chapter 2.

PyTrax stores all pertinent variables within the environment which it is executed, so all raw dataframes are made available to the user, and can be optionally stored as .csv files for inspection. PyTrax is non-destructive, so additional values are only appended to the input result file, without altering results. If an age model is incorporated using CLAM (Blaauw 2010) or BACON (Blaauw and Christen 2011), data can be plotted by age estimates, corresponding to depth. If an age model is present, but retaining the regular sampling pattern of the Itrax data is preferable, a secondary y-axis can be plotted, with major ticks at the sampled depths, and minor ticks, set to a user-defined frequency (in years), plotted between each major tick. The minor tick spacing changes respective to the depth-equivalent age, thus visualizing increasing or decreasing sedimentation rate. As a preliminary option, linear core compaction correction can be automatically performed, to which any age-model data will be adjusted, accordingly.

A summary of functions is provided in Appendix A1.1. The flexibility of PyTrax leaves the user free to perform additional processing of their data, as the dataframe used is available following graphical generation. Using PyTrax, the data of six cores is statistically processed, and rapidly plotted in a manner standardized to the best suited protocols for this study.

1.6.1 Processing Protocols

This study followed consistent protocols for scanning and data preparation. Acceptable output count rate (OCR) was reached at 30 kV, 30 mA, and 20 seconds exposure. Additional parameters (keV/channel, energy offset, Full Width at Half Maximum (FWHM) function settings, exposure and tail slopes and offsets) were automatically optimized during the batch analysis process for each core in Q-Spec. All Cores were batch analyzed with the same elements selected, however, sum and diffraction peaks were fit on an individual basis during batch analysis, resulting in an MSE which was deemed acceptable (< 2). Pruning of data was performed automatically by PyTrax, removing erratic measurements at the partitioning site of cores required to be sectioned for multiple scans, and removing measurements deemed invalid by Q-Spec.

All data was normalized to the incoherent scatter, compensating for X-ray attenuation in the highly organic gyttja section (Marshall et al. 2011). PCA was applied using a bulk dataset of six of the eight scanned cores. SRPM-03 and SRPM-09 were removed to improve clustering accuracy in the final data product. SRPM-03 consisted of channel deposits and as such, surface roughness, woody inclusions, reworking of sediment, and substantially less clear incoherent scatter response excluded it from study. SRPM-09 shared a similar lithology to the other cores, but contained an anomalous upper-gyttja, which did not match the general elemental trend observed in the other cores.

Following removal of aberrant cores, the data was further log transformed to improve comparability between cores (Ladwig et al. 2017). A moving average, equivalent to 1 cm, was applied to each core for smoothing. The data was then standard-scaled (z-scores), such that for each element, the mean was subtracted, and the measurement was divided by its standard deviation. Thus, each element profile will have a mean of 0 and a standard deviation of 1. These individual cores were then concatenated into a

single hierarchical dataframe for PCA. Individually standardizing each core eliminated potential extreme variance, which would arise from standardizing all cores in one concatenated dataframe. As per the findings of Schreiber et al. (2014), a second PCA, following the same initial processing steps was conducted. In this comparative analysis, only the gyttja was considered, and each core was truncated to exclude the marl before the application of the moving average. The comparative PCA, provided as an option in PyTrax, allows for a closer examination of principal component loadings in a single lithological context, where observing the entire core would potentially experience complications from vastly different element origins in the marl. An agglomerative hierarchical CA was applied using Ward's Method and a Euclidean Distance metric, where clusters were selected arbitrarily to enhance chemofacies groupings to a reasonable extent. Data was plotted both by depth, and for SRPM-02, by age, to investigate elemental trends through time, and correlate events across the study area using the individual radiocarbon samples taken strategically based on element profile observations.

1.7 Thecamoebian Analysis

While Itrax data exceeds the resolution of many other paleolimnological techniques, it cannot be used in exclusion to other ecological proxies. The employment of micropaleontological data is a staple of paleolimnological analysis, and pairs well with XRF datasets to enhance interpretations (Wiik et al. 2015). Testate amoebae are a group of fresh, brackish water, and sometimes terrestrial protists which build hardened shells ('tests') around themselves in an autogeneous manner, or through agglutination of local particulates (Scott et al. 2001). Thecamoebians (testate amoebae) are specifically useful, but under-used in geoarchaeology, which provide highly localized data of subtle environmental change (Patterson et al. 2002; Gearey and Caseldine 2006; Sonnenburg et al. 2011; Volik et al. 2016). Archaeologically-focused paleoenvironmental analysis often

utilize pollen, plant macrofossil, or diatom datasets to visualize a broad image of wetland and terrestrial floral assemblages through time, and has been used extensively at Rice Lake (McAndrews 1984; Yu and McAndrews 1994; Yu et al. 1996). While essential, pollen and diatoms lack the specificity suited to disentangling the environmental history of Rice Lake, which had a wide range of peripheral wetland and lacustrine sub-environments (Sonnenburg et al. 2013).

The conditions which favour the success of one thecamoebian population over others is progressively better understood through the examination of modern environments, both natural and anthropogenically influenced (Patterson et al. 1985; Reinhardt et al. 1998; Reinhardt et al. 2005; Roe et al. 2010; Watchorn et al. 2013). Previous thecamoebian analysis at Rice Lake by Sonnenburg et al. (2013) provided a detailed description of the biofacies within and before the Archaic Period marl, but did not provide as detailed a record for the gyttja.

This study improves on the resolution of the gyttja, with thecamoebian abundances calculated at 5 cm intervals (volume and sample widths described in section 1.5.5) for the same core on which age modelling was performed. Samples were randomly wet-split into 1/8th fractions, then refrigerated to inhibit microbial growth (Scott et al. 1993). Samples were sieved through a 43 µm mesh to remove clay and fine organic matter. Specimens were counted using an Olympus SZX-12 trinocular microscope under 80–116 × magnification, and were identified using type samples from the McMaster University Micropaleontology Lab, and the identification key of Kumar and Dalby (1997). Statistically significant populations were determined according to Patterson and Fishbein (1989). Using a Boolean test, species with a standard deviation greater than fractional abundance in more than 50% of samples were excluded from further statistical analysis. Species and stratigraphic associations were determined using agglomerative hierarchical clustering, with Ward's method and a Euclidean distance metric. Relative

indication of ecosystem health was explored using the Shannon-Weaver diversity index (Shannon 1948). All data processing was performed using Python, in an extension of the PyTrax code.

Chapter 2

Micro-XRF geochemical and micropaleontological evidence for prehistoric land disturbance: construction of the Middle Woodland (ca. 300 BCE–700 CE) Serpent Mounds complex, Rice Lake (Ontario, Canada)

2.1 Abstract

Serpent Mounds is a prehistoric (Middle Woodland Period, ca. 2000–1000 BP) burial mound complex located on the north shore of Rice Lake, in southern Ontario, Canada. The complex includes a 60 m long and 10 m wide sinuous earthwork ridge and eight smaller (up to 14 m diameter) oval mound structures interpreted as a serpent effigy. Archaeological excavations conducted in the 1950's determined the mound complex was built by peoples of the Point Peninsula Complex who occupied the site on a seasonal basis to harvest wild rice and shellfish and to conduct mortuary rites. The timing of mound construction and site occupation is poorly constrained by a limited number of radiocarbon dates on human burials. The site is of high cultural importance as the only known effigy mound structure in Canada and is a sacred First Nations burial ground; no further excavations are permitted onsite and all future work must employ non-invasive techniques.

High-resolution μ -XRF-CS and micropaleontologic analysis (testate amoebae) of 12 lake sediment cores was employed to investigate the timing of mound construction and to assess sediment geochemical records of prehistoric land disturbance. The lithostratigraphy consists of a 1–2 m thick organic-rich gyttja overlying interbedded peat and marl. Land disturbance is indicated by an increase in the abundance of minerogenic elements (K, Ti, Zr, Si, Fe) within a distinctive silt-rich gyttja unit, signaling an increase in the influx of detrital sediments to the lake. The event is also recognized by a shift to a thecamoebian assemblage dominated by *D. oblonga*, *C. tricuspis*, *D. proteiformis*, indicating a more eutrophic, turbid lake environment. PCA and CA of μ -XRF data identifies the event as a distinctive chemofacies across several cores. AMS ^{14}C dates for the land disturbance event correspond with the Point Peninsula occupation of sites around Serpent Mounds, indicating a protracted occupation over a period of about 750 years (2050–1300 cal BP) with two major peaks in soil erosion at ca. 2200 and 1350 cal BP. The sediment accumulation rate ($> 1.5 \text{ mm yr}^{-1}$) during the Middle Woodland phase of enhanced erosion was comparable to that during the 1838 CE dam construction. The reconstructed Middle Woodland paleoshoreline and water levels indicate shallow lake and wetland and environments, which provided suitable habitats for the growth of wild rice stands and shellfish resources. The results demonstrate that μ -XRF-CS and micropaleontological methods are important tools for the investigation of culturally-sensitive archaeological sites, including sacred burial grounds where conventional archaeological excavation or onsite coring cannot be undertaken.

2.2 Introduction

The construction of monumental earthworks and megaliths was a hallmark of many Neolithic cultures and coincided with the emergence of agriculture and permanent settlements with greater social organization and communal division of labour (Sherratt

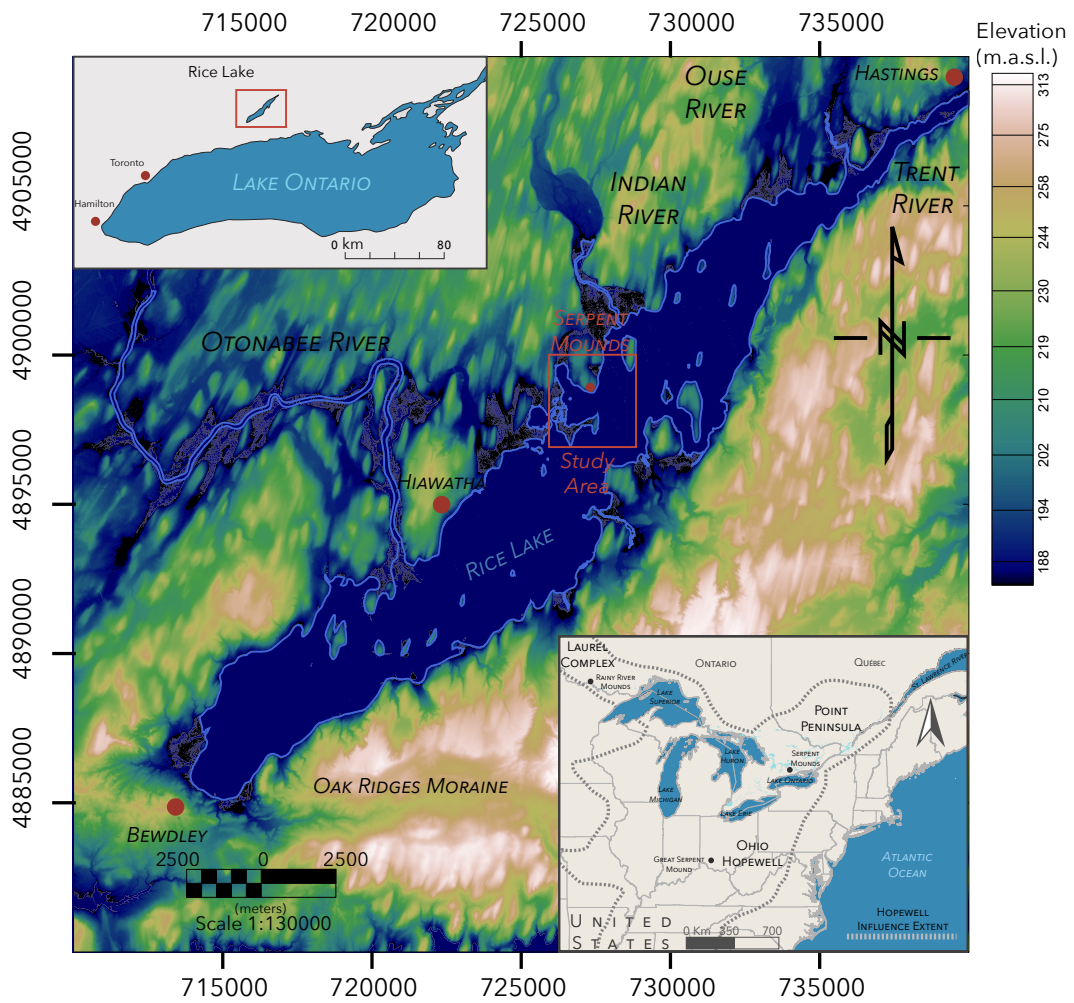


Figure 2.1: Regional map of Rice Lake. Lower-right inset displays the Hopewell cultural extent and significant mound sites related to this phase of Middle Woodland mound building (modified from Boivin et al. (2013))

1990; Bradley 1998; Artursson et al. 2016). In North America, engineered earthworks were an important innovation of the Early Woodland (ca. 800 BCE–10 CE) Adena and Middle Woodland (ca. 100–500 CE) Hopewell cultures of the Ohio Valley (Bernardini 2004; Milner 2005; Brown 2014; Henry and Barrier 2016). Adena-Hopewell peoples built a diverse range of earthworks, including monumental effigy mounds (e.g. Great Serpent Mounds, Adams County), expansive burial mound complexes, and other architectural features (ditches, earthen embankments, enclosures) constructed as ceremonial centres and for defensive purposes (Abrams and Freter 2005; Pederson Weinberger 2006; Mueller 2018). Due to the expansion of Hopewell trade networks and cultural influence during the Middle Woodland period, Hopewell mound-building methods and mortuary practices were adopted by other cultures in eastern North America (Kenyon 1986). The so-called Hopewell ‘interaction sphere’ enveloped a large area of the midcontinent, extending northeastward from Ohio into Ontario and Quebec and into the southeastern United States (Fig. 2.1).

In southern Ontario, Canada, mound-building was adopted as a burial practice by Middle Woodland peoples of the Point Peninsula Complex (ca. 2400–1300 BP) (Kenyon 1986; Walker 2015). The most impressive and archaeologically important earthwork from this culture group is Serpent Mounds, located on the north shore of Rice Lake, near Hiawatha, Ontario (Fig. 2.1, 2.2). The mound complex comprises a 60 m-long, 8 m-wide earthwork ridge (the Serpent) (Mound E, Fig. 2.2) and eight smaller, roughly elliptical mounds, up to 14 m in diameter. The Serpent mound rises 1.5–2m above the surrounding topography and has a sinuous crestline in plan that has been interpreted as a serpent effigy (Boyle 1897; Kenyon 1986). Archaeological excavations conducted in the 1950’s, determined that the site was occupied on a seasonal basis by Point Peninsula peoples for rice and shellfish harvesting beginning in the 1st century CE (Johnston 1968; Dillane 2010). While the excavations were extensive and yielded much information on Point Peninsula culture and burial practices, the mounds remain enigmatic; the age of the

mound structures and the duration over which they were constructed, are poorly constrained by a limited number of radiocarbon dates from burials at different levels in the mound fill (Table 2.1). Based on the spread of the radiocarbon ages, Johnston (1968) estimated that the mounds were constructed over a period of about 170 years, from 120 to 290 CE, but there is large uncertainty as to the onset of mound building and whether the earthworks were built incrementally or during a single phase of construction (Johnston 1968). Serpent Mounds provides one of the best documented archaeological records of the Point Peninsula culture in southern Ontario (Johnston 1968; Kenyon 1986) and was designated as a National Historic site of Canada in 1982 (ParksCanada 2018). The mounds are also of importance to indigenous communities as a sacred burial ground and have been protected since 1990 under the stewardship of the Hiawatha First Nation (Hiawatha, Ontario). Due to their cultural value, archaeological excavations are no longer permitted on the mound site; all future work must employ non-invasive techniques and be conducted in consultation and collaboration with First Nations stakeholders.

In this study, we evaluated the potential for non-invasive investigation of Serpent Mounds using sediment geochemical and micropaleontologic proxies from 12 lake sediment cores extracted from the littoral zone adjacent to the site (Fig. 2.2). A primary objective was to determine whether mound construction and seasonal human activities (shellfish harvesting, burials) at Serpent Mounds could be recognized in the lake sediment geochemical and micropaleontological record. Downcore changes in elemental abundance were measured using μ -X-ray-fluorescence core scanning (μ -XRF-CS) in order to identify land disturbance events and lake paleolimnological conditions determined by analysis of lacustrine and wetland thecamoebian taxa. μ -XRF data identify a marked increase in several minerogenic elements (Si, K, Fe, Ti) indicating an increase in the flux of detrital sediment during the Middle Woodland Point Peninsula occupation. Changes in thecamoebian abundance and diversity also indicate a shift to a

more eutrophic and turbid lake environment during the occupation phase. We interpret the increase in detrital sediment flux and attendant changes in lake trophic conditions as a land disturbance signal, recording the increased erosion of soils from the burial mound site and increased turbidity of the lake environment due to seasonal shellfish and rice harvesting. The reconstructed Middle Woodland water levels and paleogeography demonstrate that the coastline was dominated by wetlands and shallow (< 1 m) littoral environments that would have favourable for the growth of wild rice.

Several recent studies have documented land use impacts stemming from prehistoric indigenous agriculture and deforestation in North America (Burden et al. 1986; Ekdahl et al. 2004; Munoz et al. 2010; Stinchcomb et al. 2011). This paper is the first to document pre-agricultural prehistoric land disturbance, resulting from burial mound construction and seasonal resource gathering. The approach described here has broader applications for detecting prehistoric landscape disturbance at other archaeological sites where conditions favour the deposition and preservation of anthropogenic sediment in local deposcenters such as wetlands and lagoons (e.g. Ekdahl et al. (2004); Sonnenburg et al. (2011)).

2.3 Study Area

2.3.1 Physical Setting

Rice Lake (125 km²) is located 20 km southeast of Peterborough, Ontario and is part of the 386 km-long Trent-Severn Waterway connecting Georgian Bay with Lake Ontario (Fig. 2.1). The lake is about 26 km in length, 3-4 km in width, and has a maximum water depth of 10 m (Sonnenburg et al. 2012). Rice Lake receives inflow along its north shore from the Otonabee, Indian, and Ouse rivers and drains southeastward into Lake Ontario

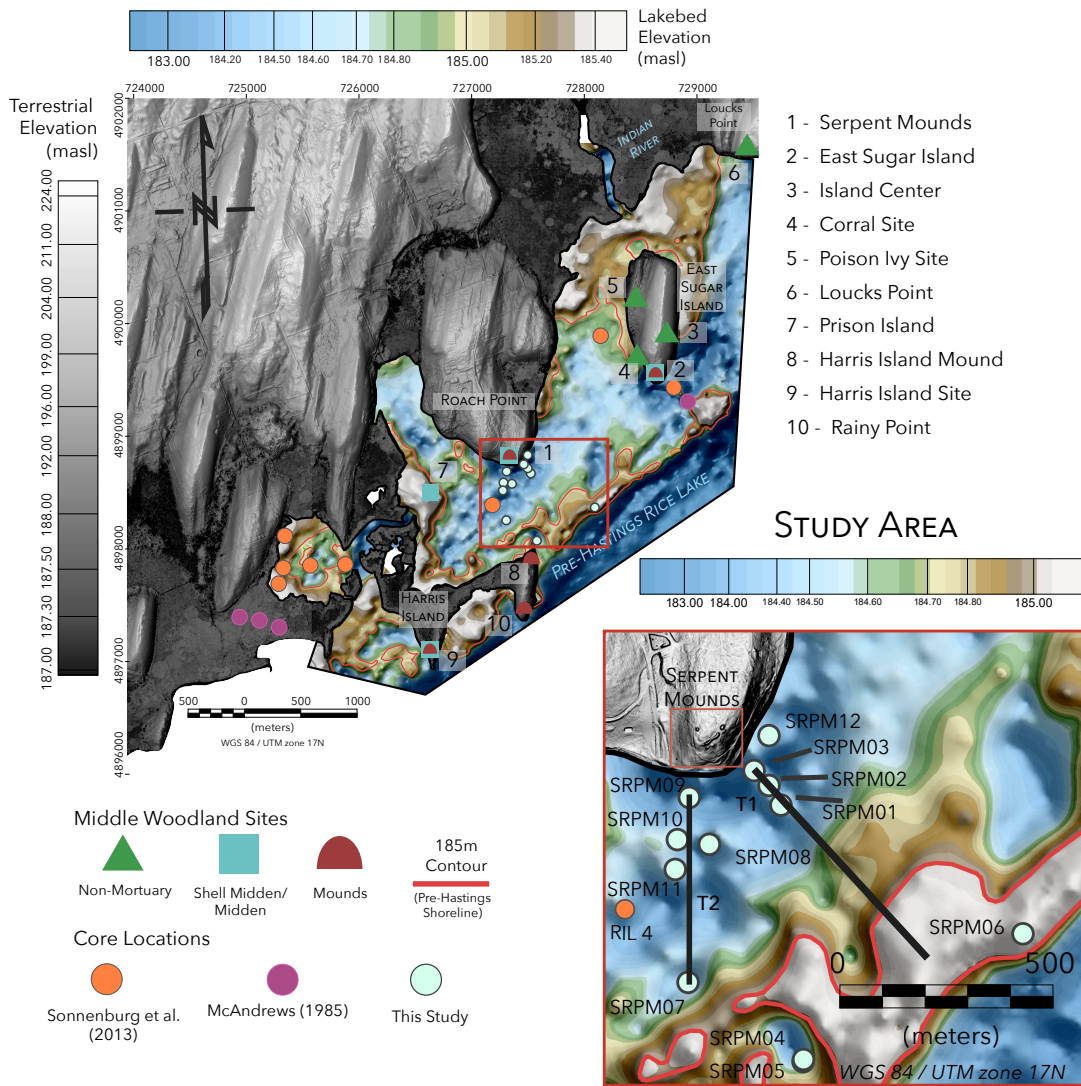


Figure 2.2: Study area map digital bathymetric map and elevation using composite data from this study and Sonnenburg et al. (2013), and DTM from South Central Ontario Orthophotography Project (SCOOP) (MNR 2013), showing the locations of Point Peninsula associated sites within proximity to the study area, and core locations from this study and others.

via the Trent River (Fig. 2.1). Serpent Mounds lies within the Indian River watershed (210 km²) and is located about 1 km east of the mouth of the Indian River (Fig. 2.1).

Rice Lake occupies a flooded glacial valley within the Peterborough Drumlin field, a 70 km wide belt of glacial terrain that extends from the Precambrian Shield southward to Lake Ontario (Fig. 2.1) (Gravenor 1957; Boyce and Eyles 1991; Maclachlan and Eyles 2013). The southern shore is defined by high relief kame topography of the west-east trending Oak Ridges interlobate moraine (Fig. 2.1) (Duckworth 1979; Gorrell and Brennand 1997; Shaw et al. 2010). Serpent Mounds complex occupies a 4.4 ha area on the south slope of a flat-topped drumlin hill (Roachs Point) at about 15 m above the present level of Rice Lake (Fig. 2.2). Many of the islands in Rice Lake are 'drowned' drumlin features that have been inundated by rising post-glacial water levels and dam flooding (Fig. 2.2) (Gravenor 1957; Yu and McAndrews 1994).

The bedrock below the lake is composed of Ordovician limestone and shales of the Trenton Group (Gravenor 1957; Carson 1980). The Paleozoic rocks overlie Late Proterozoic igneous and metasedimentary rocks of the Canadian Shield, which are exposed at surface about 40 km to the north of the study site (Gravenor 1957). The local soils consist of a silty to sandy loam derived from the Late Wisconsin-age Newmarket Till, which is the predominant surficial sediment type across the study area (Gorrell and Brennand 1997). The till has a silty carbonate-rich matrix with abundant granule to cobble-sized clasts that are a mixture of local bedrock (dominantly limestone and shale) and far-transported Precambrian granitic and gneissic lithologies. Locally, the till is draped by thin lacustrine clay and sand deposited in high-level glacial Lake Iroquois (Gorrell and Brennand 1997; Sonnenburg et al. 2013).

2.3.2 Water Levels and Paleoenvironments

The Holocene water level history and paleoenvironment of Rice Lake have been documented in several previous studies (McAndrews 1984; Yu and McAndrews 1994; Yu et al. 1997; Sonnenburg et al. 2011; Sonnenburg et al. 2012; Sonnenburg et al. 2013). The lake basin was formed during deglaciation (ca. 12.5 Ka BP) as rising water levels in glacial Lake Iroquois flooded river valleys and embayments to the south of Peterborough (Fig. 2.1) (Gravenor 1957; Muller and Prest 1985). Following the drainage of Lake Iroquois (ca. 11.7 Ka BP), water levels fell to a maximum lowstand (~10 m bpl) and had begun to recover by 9.5 Ka BP due to isostatic uplift of the eastern lake outlet at Hastings and a shift to a cooler, wetter climate (Yu et al. 1997; Sonnenburg et al. 2012). By 8 Ka BP water levels were close to the modern, pre-dam level (~185 m asl) and laminated marl was deposited basin-wide in an oligotrophic lake environment with an aquatic plant macrofossil assemblage dominated by *Najas flexilis* (Vreeken 1981; McAndrews 1984; Yu and McAndrews 1994).

During the mid-Holocene (ca. 6–4 Ka BP) water levels fell to a second lowstand phase as recorded by a basin-wide erosional hiatus (unconformity surface) between the marl sequence and overlying detrital mud and gyttja (Sonnenburg et al. 2013). The lowstand coincided with a period of warmer and drier climate in central and eastern North America (Dean et al. 1996; Yu et al. 1997). The lake basin was likely hydrologically closed during this phase as water levels were below the Hastings outlet bedrock sill (~185 m asl) (Sonnenburg et al. 2013). After 4 Ka BP, water levels in Rice Lake rose gradually, owing to a wetter, cooler Neoglacial climate (McAndrews 1984; Sonnenburg et al. 2013). Pollen records indicate a diverse deciduous forest abundant in Beech, Elm, Maple, and Birch and a wetland pollen assemblage indicating both emergent and submergent plants (McAndrews 1984). By 3 Ka BP water levels had begun to stabilize, resulting in the expansion of wetlands and establishment of abundant wild rice stands

in Rice Lake (McAndrews 1984). Wild rice was an important resource for Woodland peoples but was diminished significantly in abundance following the construction of the Hastings Dam (Sonnenburg et al. 2012).

The Hastings Dam, was constructed in 1838 at Rice Lake's outlet as part of the Trent-Severn waterway canal and lock system. It was engineered to provide alternative shipping routes between Lake Ontario and Lake Huron, bypassing the Welland Canal (Fig. 2.1). Subsequently, the dam raised the water levels by 1.8–2 m, inundating large tracts of coastal wetlands (Yu and McAndrews 1994; Dillane 2010; Sonnenburg 2010). The dam construction phase is recorded by an increasing sedimentation rate and a rise in the abundance of *C. tricuspis* in the uppermost gyttja unit, indicating a more nutrient-rich environment (Sonnenburg et al. 2013). Due to the shallow average water depth (~4 m), the abrupt post-dam rise in water levels dramatically altered shoreline positions and drowned the mouths of major river systems feeding Rice Lake (Sonnenburg et al. 2013). At the beginning of the Middle Woodland phase water levels the lake shoreline and the mouth of the Indian river would have been further lakeward of their present position; reconstructing the position of the lake shoreline and water depths during the Middle Woodland period was an objective of the present study.

2.3.3 Site Archaeology

The human settlement of Rice Lake began in the Paleoindian period (ca. 11,000 BP) with the arrival of small bands of hunter-gathers and populations increased significantly during the Archaic and subsequent Woodland periods (Ellis and Ferris 1990; Sonnenburg et al. 2011). The region around the lake contains a high density of prehistoric archaeological sites (Fig. 1.5) and there is high potential for submerged sites due to flooding of wetlands and coastline following the construction of the Hastings Dam (Sonnenburg et al. 2011; Sonnenburg et al. 2013). The Serpent Mounds complex was first documented

at the end of the 19th century (Boyle 1897; Montgomery 1910) and the first systematic archaeological studies were conducted between 1955 and 1960 by the Royal Ontario Museum (Johnston 1957; Johnston 1968; Schwarcz et al. 1985; Ellis and Ferris 1990). The excavations conducted by Johnston (1968) were extensive and provided a wealth of information on Point Peninsula culture and burial practices but were also extremely invasive; the Serpent mound was excavated to its base along one-half of its length and 159 human skeletons were exhumed for study (Harrison and Katzenberg 2003). The excavations yielded abundant Point Peninsula pottery and lithics, and also far-transported marine shells and metal beads that are indicative of a far-reaching Hopewell trade network (Johnston 1968; Walker 2015). The mounds are associated with an extensive, 30 cm-thick shell midden that extends 90 m along the southeastern shoreline of Roach Point (Fig. 2.2). The midden contained large quantities of freshwater mussel shells (*Elliptio complanata*, *Lampsillis siliquoidea*), interbedded with ash layers and minor animal bone and pottery refuse (Johnston 1968). A radiocarbon date obtained on charcoal from the base of the midden yielded an age of 1820–2153 cal BP, which is a few hundred years older than the date obtained for the base Serpent Mound E (Fig. 2.2)(Table 2.1), indicating that mussel harvesting had taken place possibly before mound construction.

Archaeological evidence indicates that the Serpent Mounds was occupied on a seasonal basis, beginning in the 1st century CE, for shellfish harvesting and feasting, and to conduct burial rites (Johnston 1968; Dillane 2010). The onset of mound-building and the duration over which the mounds were constructed, however, is not well constrained. Using ceramic seriation and radiocarbon dates obtained on three burials, Johnston (1968) estimated that the mound complex was constructed over a span of about 170 years, from ca. 120 CE to 290 CE. Johnston (1968) interpreted shell debris layers between adjacent burials as evidence for multiple stages of mound construction, with additions appended to an original, smaller structure, possibly related to feasting events (Johnston 1968; Ellis and Ferris 1990). The burials sampled for radiocarbon dating were

intrusive in the mound and post-date its construction. The age estimate was based on uncalibrated beta-scintillation radiocarbon dates, which adds additional chronological uncertainty as to the timing of burials and relation to mound building (Johnston 1968).

Serpent Mounds is the largest burial mound complex in Rice Lake, covering about 4 ha, but several other burial mound sites are in close proximity. East Sugar Island (site BbGm-11), located 1 km east of Serpent Mounds (Fig. 2.2), contains two large (> 9 m diameter) oval mounds and a shell midden (Fig. 2.2) (Curtis 2002). Several other known archaeological sites are also present on the island (Sonnenburg et al. 2012)(Fig. 2.2). A radiocarbon date taken by Stothers (1974) from the base of the East Sugar Island "Prince Mound" yielded an age of 1890 ± 60 BP (see Table 2.1). On nearby Harris Island, two additional mounds and an extensive midden deposit are situated at the north, and south end of the island (Fig. 2.2). The high density of burial mounds and shell middens in the vicinity of the Serpent Mound complex indicate the north shore of Rice Lake was a major locus for human activity during the Middle Woodland period.

As noted by Johnston (1968), the lower portion of the Serpent Mounds site was partly submerged by the Hastings Dam flooding in 1838 CE (Fig. 2.2). The flooding rapidly inundated large areas of low-lying coastal wetlands around Rice Lake, preserving a submerged landscape that has a high archaeological potential for discovery of underwater prehistoric sites (Sonnenburg et al. 2011; Sonnenburg et al. 2012). The flooding also provided favorable conditions for preservation of wetland and lake sediment archives that can be used to reconstruct water levels and environmental changes in the period prior to dam construction (Yu and McAndrews 1994; Sonnenburg et al. 2013).

2.4 Methods

2.4.1 Bathymetric mapping

Detailed bathymetric mapping was conducted over a 2 km inshore area around Serpent Mounds to aid in selection of coring locations and to allow reconstruction of water levels and paleoshoreline positions (Fig. 2.2). Water depth was recorded using a 200 kHz single-beam echosounder (Knudsen 320BP) operated from a small boat with a differential GPS navigation system. A total of 52-line-km of bathymetric data were collected along north-south lines with a nominal line spacing of 25–50m and orthogonal tie lines at 100 m intervals. Depth soundings were corrected for seasonal water level variations and transducer draft, and processed using the scheme outlined by Sonnenburg and Boyce (2008). The new survey data were compiled with the pre-existing bathymetric data for Rice Lake (Sonnenburg et al. 2013) and grid interpolated to 10 m grid cells using a kriging algorithm. The bathymetric grid was overlaid on available 2 m resolution digital terrain model (Central Ontario Orthophotography Project; SCOOP) to produce a combined digital bathymetric elevation model (DBEM) for the study site. A high-resolution slope shaded digital terrain model (DTM) was also produced for Serpent Mounds using 1 m resolution light detection and ranging (LiDAR) data (MNR 2018) (Fig. 2.2).

The DBEM was used to construct a series of paleobathymetric maps showing changes in water depth and shoreline positions between 4500 BP to present. A water level curve was constructed using AMS ^{14}C dates and their compaction-corrected depths obtained on the transgressive shoreline deposits that truncate the marl sequence in Rice Lake. AMS radiocarbon dates within the gyttja units above the marl-gyttja boundary provided constraints on minimum lake levels during the Middle Woodland period, as no direct water level indicators (e.g. shoreline deposits, wetland sediments) are available for this time period. Paleobathymetry maps were constructed for three time intervals

by subtracting (back-stripping) the isopach thickness of sediment accumulated in the period following each time step from the modern bathymetric surface (see Sonnenburg et al. (2012)). The isopach thicknesses maps were obtained by interpolation of sediment thickness from the 12 cores and assuming zero sediment thickness at the modern shoreline. Corrections were not applied for post-depositional sediment autocompaction (Allen 2000; Bird et al. 2004) as bulk density data were not available for samples; only coring compaction was factored into sediment thickness calculations. In a final step, the paleoshoreline positions were estimated by intersecting the modelled minimum and maximum water plane elevation for each time with the back-stripped paleobathymetry map.

2.4.2 Coring and sediment chronology

A total of 12 cores (1–2.5m length) were extracted from the shallow littoral zone south of Roach Point using a percussion corer (68 mm diameter polycarbonate tubes) or a gas-driven vibrocorer (70 mm diameter aluminum tubes) (Fig. 2.2). Vibrocores were cut into 1 m lengths for transport and percussion cores were extruded on-site and preserved in plastic troughs. Cores were split in the lab and the sediment texture, composition and lithofacies were logged in detail (Fig. 2.4). Cores were refrigerated at 5 °C to limit oxidation and microbial growth prior to core scanning and micropaleontological analysis. A linear compaction correction was applied to all cores using the ratio of the recovered core length to the core tube penetration depth. Sediment compaction values ranged from 2% to 55% of the recovered core length.

Core chronology was obtained by AMS radiocarbon dating of 11 organic matter samples (seeds, plant fragments) selected where changes in sediment texture, composition and element profiles indicated the presence of lithofacies and chemofacies boundaries. Samples were pre-treated using the protocols of Crann et al. (2017) and AMS ¹⁴C dated at

the A.E. Lalonde AMS Laboratory, Ottawa. The new dates and several existing ^{14}C ages available from previous work (Johnston 1968; Stothers 1974; Schwarcz et al. 1985; Yu and McAndrews 1994; Harrison and Katzenberg 2003; Sonnenburg et al. 2013) were calibrated to 2σ using IntCal13 (Reimer et al. 2013) (Table 2.1). A Bayesian age-depth model and sediment accumulation curve were constructed for a single core (SRPM-02; Fig. 2.4) using the R age-modelling package BACON (Blaauw and Christen 2011)(Fig. 2.5).

Table 2.1: Radiocarbon dates from this study and others.

Lab ID	Sample/Core Depth (cm)	Source	Material	^{14}C yr BP	cal BP (2σ)	
UOC-5729	SRPM02-RC1 (97)	This Study	twig	1720 \pm 27	1561 – 1700	(95.4%)
UOC-5730	SRPM02-RC2 (57)	This Study	twig	1157 \pm 27	1045 – 1175	(68.3%)
					983 – 1035	(27.1%)
UOC-5731	SRPM02-RC3 (173)	This Study	wood	3783 \pm 27	4085 – 4243	(95.4%)
UOC-5732	SRPM02-RC4 (126)	This Study	seeds	2689 \pm 27	2755 – 2846	(95.4%)
UOC-5733	SRPM11-RC5 (72.5)	This Study	seeds	2477 \pm 28	2432 – 2720	(95.1%)
UOC-5734	SRPM12-RC6 (73)	This Study	bark	3934 \pm 28	4287 – 4440	(90.4%)
UOC-5735	SRPM10-RC7 (64)	This Study	twig	1743 \pm 27	1569 – 1713	(95.4%)
UOC-5736	SRPM09-RC9 (124.5)	This Study	woody organics	3151 \pm 27	3337 – 3447	(90.2%)
UOC-5737*	SRPM12-RC11 (31)	This Study	charcoal	4291 \pm 27	4826 – 4880	(93.2%)
UOC-5738	SRPM12-RC12 (53.5)	This Study	wood	1159 \pm 27	1047 – 1176	(72.1%)
					985 – 1033	(23.3%)
UOC-5739	SRPM02-RC15 (221)	This Study	leaves	5820 \pm 34	6529 – 6729	(94.3%)
Beta274140a	RIL2C (213.5-215.5)	Sonnenburg et al. 2013	peat	7640 \pm 50	8378 – 8540	(95.0%)
Beta274141a	RIL2D (381.5-383.5)	Sonnenburg et al. 2014	plant	9020 \pm 50	10 133 – 10 254	(85.1%)
					9940 – 9990	(6.1%)
I-7222b	E (140-150)	McAndrews, 1984	bulk (gyttja)	3890 \pm 130	3973 – 4645	(92.2%)
I-7223b	E (183-200)	McAndrews, 1984	bulk (marl)	6555 \pm 115	7262 – 7619	(95.0%)
M-850c	Mound "E" East	Johnston, 1968	carbonized log	1830 \pm 200	1355 – 2158	(93.4%)
M-1104c	Shell Midden Base	Johnston, 1968	charcoal	2020 \pm 75	1820 – 2153	(94.1%)
M-1105c	Mound "E" South	Johnston, 1968	charcoal	1660 \pm 75	1388 – 1726	(95.0%)
UGA-2487d	Serpent Pits OP1	Johnston, 1979	bone	905 \pm 60	726 – 929	(93.2%)
UGA-2489d	Serpent Pits OP3	Johnston, 1979	bone	660 \pm 60	543 – 687	(95.0%)
DIC-56e	Prince Mound Sub-floor	Stothers, 1974	charcoal	1890 \pm 60	1701 – 1951	(93.5%)
**	Rib Fragment (TO-8708)	Harrison and Katzenberg, 2003	bone	**	1410 – 1635	(95.5%)
**	Mound G&I	Schwarcz et al. 1985	bone	1550 \pm 100	1292 – 1626	(93.3%)

** Not provided in source

2.4.3 μ -XRF core scanning

Eight cores were selected along two transects for μ -XRF-CS (Fig. 2.2). Split cores were scanned on an Itrax μ -XRF core scanner (Cox Analytical Systems) using a 3 kW Cr target (Croudace 2006) with constant exposure time of 20 seconds and 30 kV, 30 mA power settings. Cores were scanned at a 500 μm sample interval, with the exception of SRPM-02, which was scanned at 1 mm intervals. High-resolution RGB optical scans of each core were acquired with 0.047 mm pixel $^{-1}$ resolution. RGB scans detected subtle changes

in the gyttja appearance, due to composition and texture, which were often not discernible by visual inspection of the split cores. XRF spectra were batch analyzed using the Q-Spec software package, after correcting for sum, escape, and diffraction peaks, in addition to optimizing element selection (Rodríguez-Germade et al. 2015; Bloemsmas et al. 2018). Only elements that were appreciably free of noise were plotted and any measurements deemed invalid by the Itrax were removed from further analysis. The suite of selected elements included Fe, Ti, K, Si, Zr, S, Ca, Sr, and Ni.

The incoherent to coherent scattering ratio (inc/coh) was plotted to assess downcore changes in organic matter content (Guyard et al. 2007; Burnett et al. 2011). Element peak areas were normalized using the incoherent (Compton) scatter in order to minimize matrix effects produced by downcore changes in sediment porosity, density, organic matter and moisture content (Nielson 1977; Thomson et al. 2006; Marshall et al. 2011; Fortin et al. 2013; Ohlendorf et al. 2015).

2.4.3.1 Statistical analysis

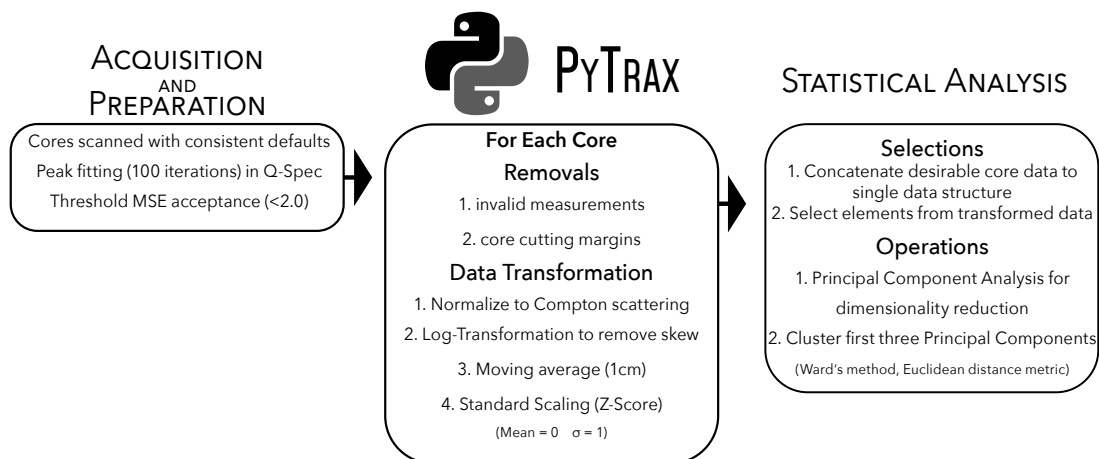


Figure 2.3: A flowchart showing steps in processing and statistical analysis of μ -XRF data

Multivariate statistical methods (e.g. PCA, CA) are employed increasingly in the analysis of μ -XRF-CS data as tools for data exploration and quantitative evaluation of chemofacies (Metcalf et al. 2010; Schreiber et al. 2014; Lintern et al. 2015; Ladwig et al. 2017; Pérez et al. Article In Press; Poraj-Górska et al. 2017). In this study, PCA and CA was performed on six cores using the processing flow shown in Figure 2.3. Cores SRPM-03 and SRPM-09 were excluded from the analysis as they showed evidence of sediment reworking or anomalous element profiles. Plotting of element profiles and statistical analysis was performed using the Python package PyTrax (Pringle, 2018), implementing tools from several libraries, including, Sci-Py (Jones et al. 2001–), Matplotlib (Hunter 2007), Pillow (Python Image Library Fork) (Clark et al. 2010–), Scikit-Learn (Pedregosa et al. 2011), Seaborn (Waskom et al. 2014), and Pandas (McKinney 2015). Prior to statistical analysis, the normalized element profiles were log transformed to mitigate skew and improve inter-core comparisons (Ladwig et al. 2017). Element profiles were smoothed using a 1 cm moving average and standardized as z-scores by subtraction of the sample mean (\bar{x}) and division by the standard deviation (σ):

$$\frac{x - \bar{x}}{\sigma} \Rightarrow \bar{x}_a = 0; \sigma_a = 1 \quad (2.1)$$

where the resultant dataset will have a new mean of 0 (\bar{x}_a) and a standard deviation of 1 (σ_a) (2.1). To determine the relationships of these elements to one another, a standardized heatmap of pairwise correlations was generated using Pearson's correlation coefficient. In addition, an R-Mode dendrogram (Ward's method, Euclidean distance metric) was appended, using the smoothed and standardized, normalized element profiles (Fig. 2.7).

Two separate PCAs were run for each core: one on the whole core (including both the marl and gyttja units) and a second analysis on the upper gyttja portion, following

the approach of Schreiber et al. (2014). This was required as the marl and gyttja lithofacies had highly contrasting composition and geochemistry and the inclusion of marl elemental data in the PCA limited the discrimination of distinct clusters in the gyttja unit, which was of primary interest in this study.

The loadings of the first three principal components in each analysis were plotted and hierarchically clustered using Ward's method (Euclidean distance metric) (Fig. 2.6) and plotted as colour-representative intervals. PCA was also applied to the RGB core scans, to assist in the discrimination and correlation of lithologic units. Core images were cropped to exclude non-sediment pixels and the median RGB value of each pixel row in the image was calculated. A 215-sample moving average (~1 cm) was performed down the length of the median RGB values, then standardized according to (2.1), and PCA was performed in PyTrax. The PCA determined that 98% of the variance in colour values was explained by PC1, with loadings displaying an equal, positive contribution from all three channels (A2.1). PC1 can be interpreted as being the 'brightness' of the image, and was overlaid on a lithology-colour-coded representation of a Ward's Euclidean Distance agglomerative cluster.

2.4.4 Micropaleontology

Micropaleontological analysis examined changes in thecamoebian (Arcellacea) abundance and diversity in core SRPM-02 (Fig. 2.4). Thecamoebians are testate protists with both agglutinated and autogenous shells, are abundant in lacustrine and wetland environments and are useful indicators of a wide range of environmental conditions including lake trophic status, water depth, pH, oxygenation, eutrophication, and pollutant levels (Patterson et al. 1996; Reinhardt et al. 1998; Patterson and Kumar 2000; Patterson et al. 2002; Roe et al. 2010; McCarthy and McAndrews 2012). Several studies have employed thecamoebians to identify land disturbance events (e.g. deforestation, dam

construction) associated with European settlement (Patterson et al. 2002; Reinhardt et al. 2005; Sonnenburg 2010). For microfossil analysis, 1.25 cm³ sediment samples were collected at 5 cm intervals from the gyttja units in core SRPM-02 (0–180cm; Fig. 2.4). The underlying marl facies were not analyzed as they are of mid-Holocene age and pre-date the Middle Woodland period (Sonnenburg et al. 2013). The samples were rinsed through a 43 µm mesh to retain thecamoebian tests, and remove clay and fine organic particles. Samples were divided into 1/8 fractions using a wet splitter and refrigerated to prevent microbial growth (Scott et al. 1993). Thecamoebians were counted using an Olympus trinocular microscope under 80–116× magnification and species were identified using type samples and the identification key of Kumar and Dalby (1997). A total of 33 thecamoebian species and strains were identified and 15 statistically-significant taxa were used for the analysis. Raw counts were converted to specimens per cc and the relative fractional abundance F_i of each taxonomic unit for each sample was calculated:

$$F_i = \frac{C_i}{N_i} \quad (2.2)$$

where C_i is the number of species and N_i is the total of all species counted in that sample. The standard error S_{x_i} for each taxon was calculated to 2σ following Patterson and Fishbein (1989):

$$S_{x_i} = t \cdot \sqrt{\frac{X_i(1 - X_i)}{N_i}} \quad (2.3)$$

Species were considered statistically insignificant and removed from further analysis if $X_i < N_i$ in more than 50 percent of samples. The Shannon-Weaver Diversity Index (SDI) was calculated for each sample as an indicator of faunal diversity and ecosystem

health (Shannon 1948; Peet 1974; Patterson et al. 2002; Sonnenburg et al. 2013):

$$SDI = - \sum_{i=1}^S \left(\frac{X_i}{N_i} \right) \cdot \ln \left(\frac{X_i}{N_i} \right) \quad (2.4)$$

where S is the species richness of the sample. SDI values of 2.5–3.5 indicate a stable environment, 1.5–2.5 are transitional, and values between 0.1 and 1.5 indicate stressed environments (Magurran 1988; Patterson and Kumar 2000). Micropaleontological analysis was conducted on a single core (SRPM-02) as it contained the most complete sediment record, with only 2% sediment compaction.

Statistical analysis of thecamoebian data employed Q-mode clustering to group statistically similar populations (Ward's minimum variance method) and R-mode clustering to determine closely-related species and species assemblages (Fishbein and Patterson 1993). The Q- and R-mode cluster analysis was performed on 15 statistically significant thecamoebian taxa. A colour-mapped representation of the sample clusters was plotted against core depth and compared with the PCA cluster analysis for core SRPM-02.

2.5 Results

2.5.1 Core lithofacies

Seven distinctive lithofacies were identified based on sediment texture, composition, and brightness changes detected by RGB image analysis (Fig. 2.4). A Bayesian age model incorporating five AMS ^{14}C dates from core SRPM-02 is shown in Figure 2.5. The lithostratigraphy consists of an uppermost package of organic-rich muds (gyttja) (Units 1-4) up to 2 m in thickness, overlying interbedded marl and peat units (Unit 6, 7; Fig. 2.4).

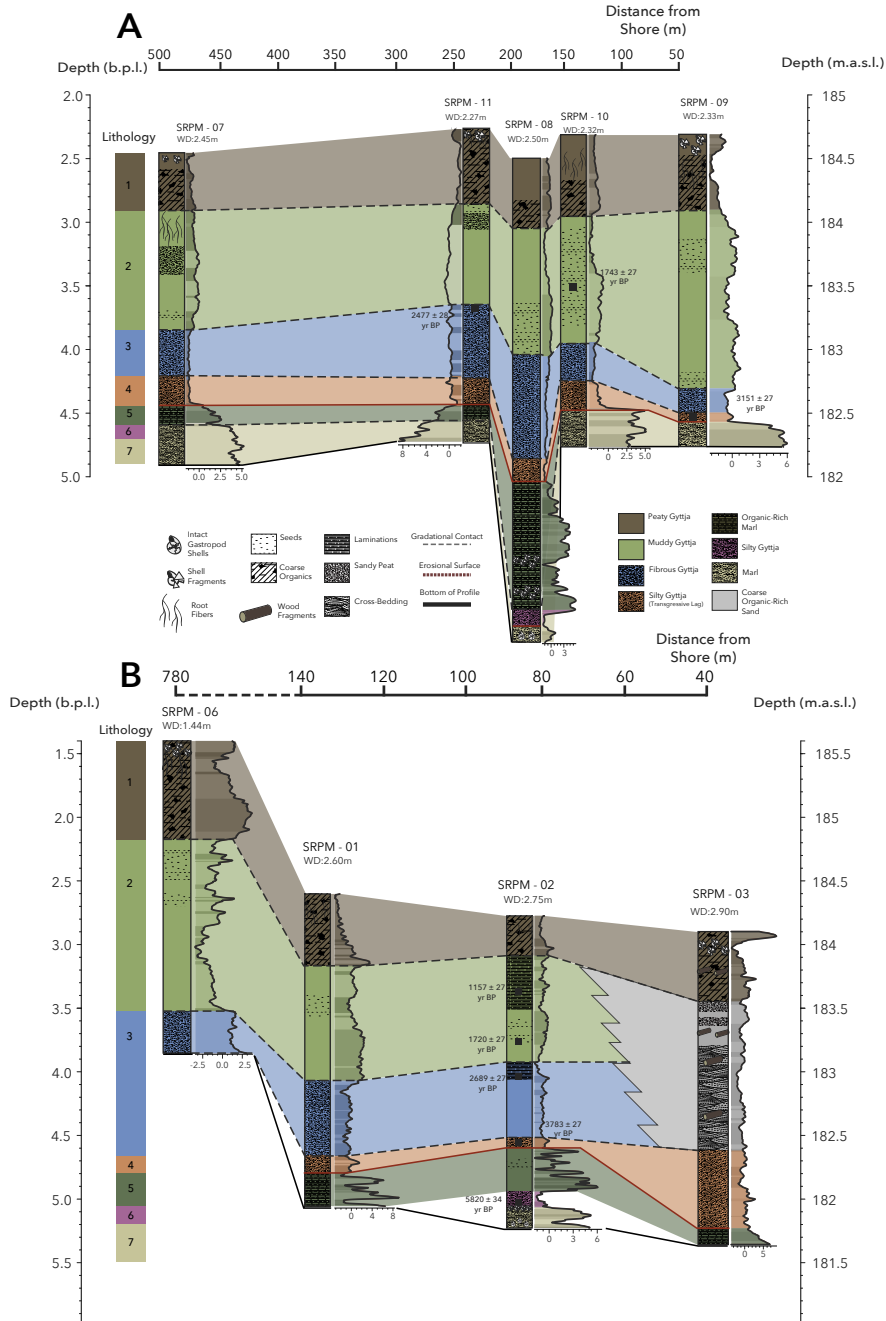


Figure 2.4: Core lithostratigraphy and AMS ¹⁴C chronology: **A.** north-south profile (T1). **B.** southeast-northwest profile (T2). RGB image brightness (Principal Component 1) plotted beside, and colorized to lithologic log for comparison. RGB PC1 has the largest magnitudes in marl deposits and within silt-rich portions of the gyttja (e.g. Unit 4), which have high optical brightness. Profile locations shown on Fig. 2.2. Water depth is relative to modern lake level at 187 m asl.

The lowermost lithofacies Unit 7 consists of a calcareous silty marl with thin peat interbeds and abundant gastropod shells (Fig. 2.4). The shells were mainly whole and intact and more numerous in the marl interbeds. Unit 7 is sharply truncated above by a silty gyttja (Unit 6) with abundant plant matter and organic fragments. Unit 6 is observed only in SRPM-02 and SRPM-08. A single radiocarbon date from Unit 6 (SRPM-02-RC15; 221 cm depth) yielded an age of 5820 ± 34 BP (6630 cal BP).

Unit 5 consists of inter-laminated marl and gyttja, with increasing organic matter up-core. This unit was observed in all cores but was absent in SRPM-09 and SRPM-10, where it was non-deposited or removed by erosion. Unit 5 is overlain by a silt-rich gyttja (Unit 4) with coarse organic matter.

The contact between Units 4 and 5 was sharp and marked a disconformity that has been identified in previous studies as a basin-wide erosional hiatus formed by shoreline transgression following the mid-Holocene lowstand phase (Sonnenburg et al. 2012; Sonnenburg et al. 2013). Radiocarbon dates from Unit 4 yielded an age range of 3151 ± 27 BP (3393 cal BP), similar to a date obtained at the marl/gyttja boundary by McAndrews (1984) (see Table 2.1). Unit 4 transitions above to a fine laminated, silty gyttja (Unit 3) with grass plant fragments. A single radiocarbon date (SRPM-02-RC3; 173 cm) at the base of Unit 3 returned a date of 3783 ± 27 BP (4163 cal BP). Unit 2 is massive, gyttja with a silty to muddy matrix and abundant seeds. Unit 2 coincides with the estimated age range of the Serpent Mounds occupation (2158–1292 cal BP), using the 2σ confidence limits for the re-calibrated dates from Johnston (1968) and Harrison and Katzenberg (2003) to bracket the interval (Table 2.1). The top-most Unit 1 is composed of a peaty gyttja with shell fragments and abundant rootlets of modern aquatic plants in the upper 5–10 cm. The upper portion of Unit 1 represents gyttja that was deposited after the construction of Hastings Dam (1838 CE).

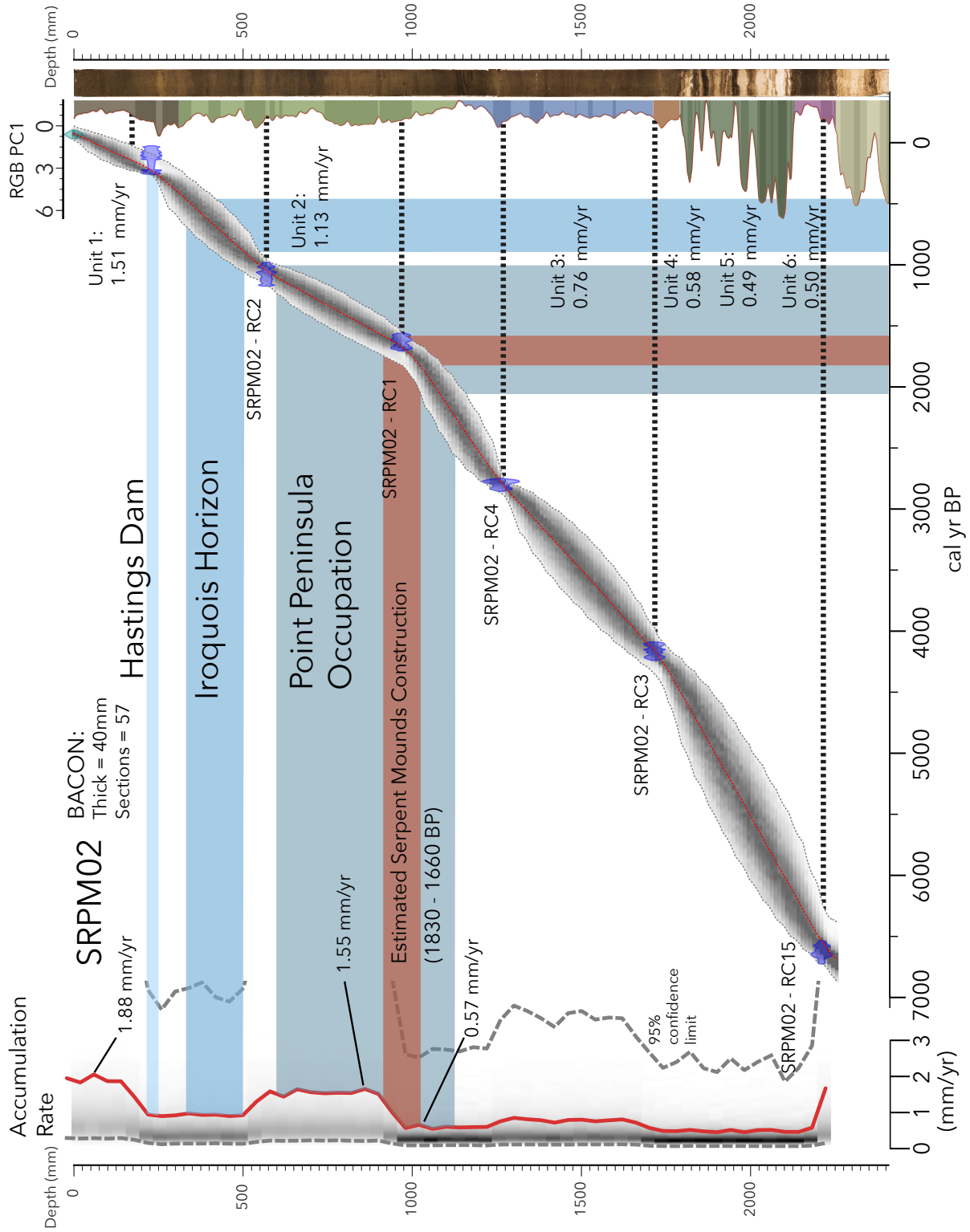


Figure 2.5: Bayesian age-depth model and accumulation rates for core SRPM02 constructed using BACON (Blaauw and Christen 2011).

2.5.2 Itrax element profiles

Element profiles for core SRPM-02 are shown in Figure 2.6 and correlation matrices and R-mode cluster dendrogram in Figure 2.7. The R-mode cluster analysis yielded two main element groupings for both the full-core model (FCM) and gyttja-only model (GOM) (Fig. 2.7). The first group consists of the minerogenic elements K, Si, Fe, Ti, Zr, which are derived chiefly from terrigenous weathering of aluminosilicate minerals and the second group, including Ca, Sr, S, are elements produced by biogenic (production of aragonite and calcite) and authigenic processes. Sr shows stronger covariance with terrigenous elements in the GOM, and clusters distinctly with Zr ($r = 0.49$). The covariance between Zr and Sr in the FCM was weaker ($r = 0.35$), as Sr in the marl likely originates from biogenic (mollusc, gastropod shells), rather than detrital sources (Murphy and Wilkinson 1980).

K, Si, Zr and Ti are commonly used as indicators of terrestrial weathering and soil erosion (Cuven et al. 2010; Balascio et al. 2011; Kylander et al. 2011; Moreno et al. 2011). At Rice Lake these elements are most likely derived from erosion of surficial sediments, which consist mainly of glacial deposits (till, glaciofluvial sediments) and lacustrine sediments (sand, silt, clay). Ti and K show strong covariance (FCM: $r = 0.96$, GOM: $r = 0.98$) (Fig. 2.7). The former is a stable element of terrigenous origin, and the latter abundant in clay minerals (Moreno et al. 2011). The primary source of Ti and K is likely the weathering of igneous and metamorphic clasts present in the till deposits, and soil-derived clay minerals. Zr, is often used as a proxy for relative grain size, as it is abundant in the coarse silt fractions of lake sediment (Oldfield et al. 2003; Turner et al. 2015). Zr, and Si are most abundant within Unit 4, where high counts of both are a geochemical marker for the basin-wide transgressive episode at the end of the Mid-Holocene (EH-2) (Sonnenburg et al. 2013), and have been recognized elsewhere in rapid water level rise and flooding events (Cuven et al. 2010; Marshall et al. 2011). Although the presence

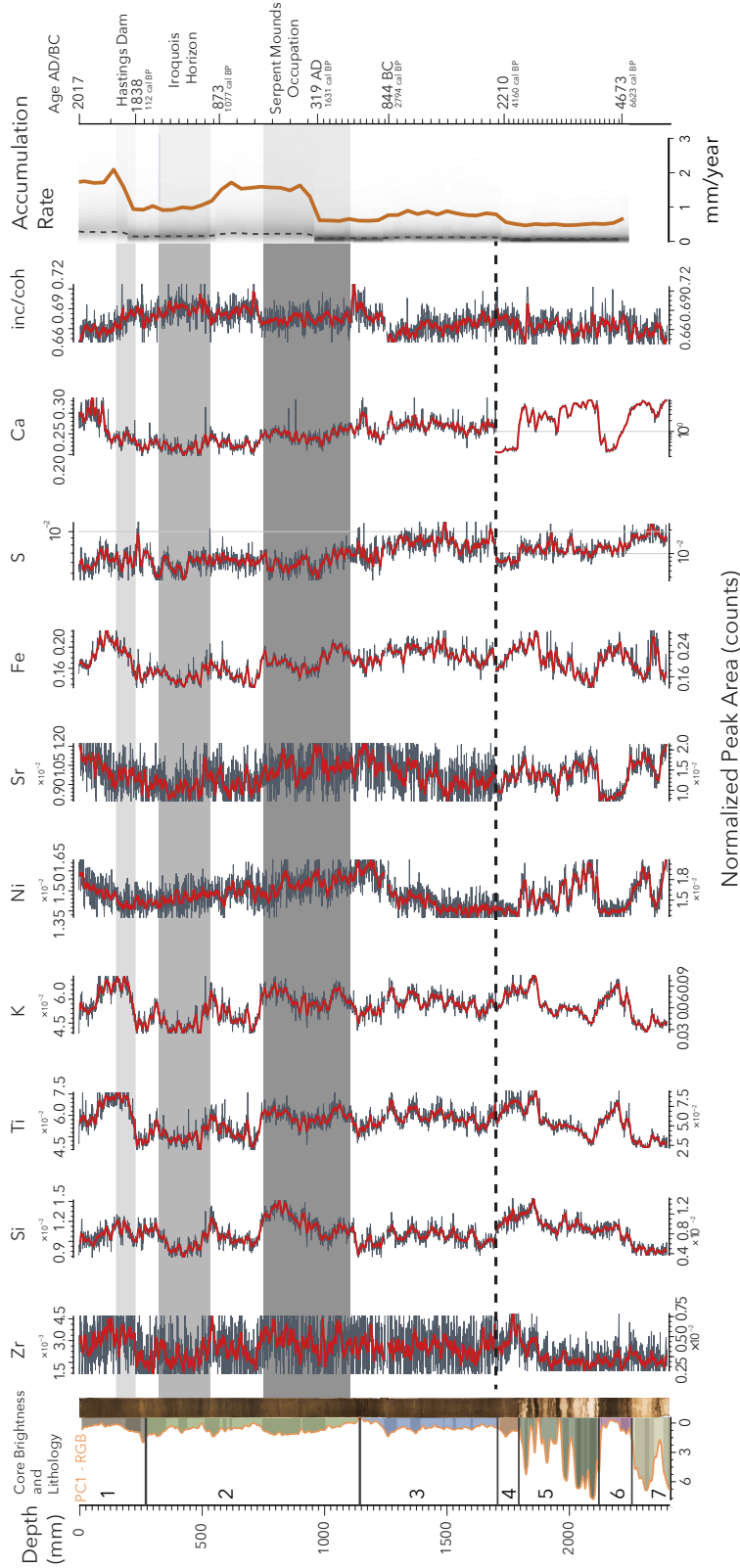


Figure 2.6: μ -XRF element profiles and RGB core scans for SRPM02. XRF peak areas are normalized to incoherent scattering. Red line overlapping element traces is a 1 cm moving average of normalized count values. Dashed line indicates change in XRF scales (for improved visibility of trends) - scales for measurements above and below the dashed line are displayed at the top, and bottom of the plot, respectively. RGB image brightness (PCI) and BACON accumulation rates (Blaauw and Christen 2011) also shown. Right axis shows AMS ^{14}C dates on non-linear time scale (minor ticks are 100-year increments) with age ranges for site occupation phases and Hastings Dam construction.

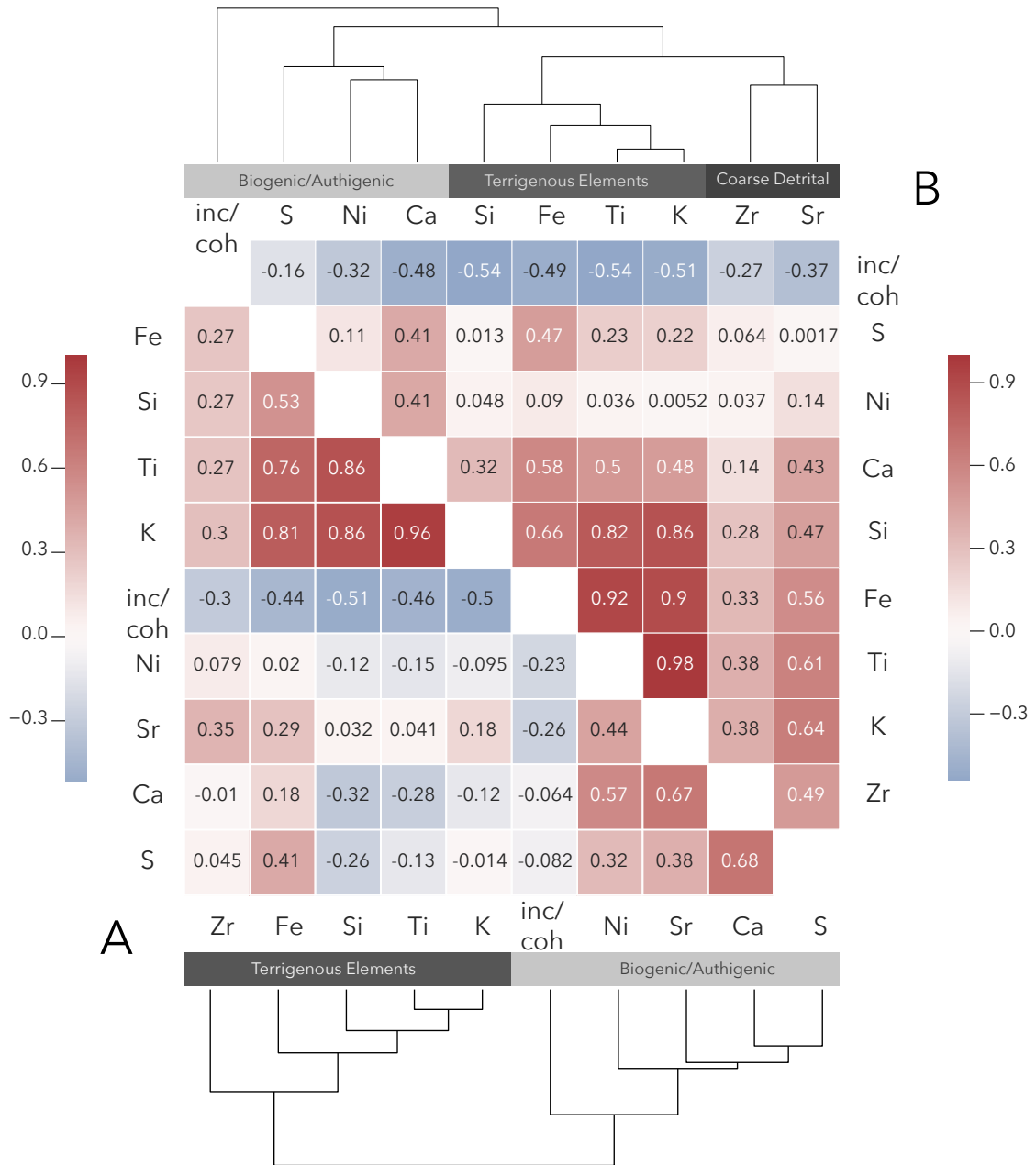


Figure 2.7: Correlation matrices for elemental abundances in full-core **A** and gytija **B** for six cores selected for analysis. Pearson's r values are plotted as a colour map and elements grouped using R-mode cluster analysis (Ward's Method with Euclidean distance metric). R-mode clustering yielded two major element groupings associated with mineralogenic (detrital) sources (Si, Fe, Ti, K, Sr) and biogenic sources (Ni, Sr, Ca, S).

of diatoms in the gyttja was noted by Sonnenburg et al. (2013), biogenic silica likely contributes little to the XRF record. Chawchai et al. (2015) emphasize that the size of diatoms, irrespective of abundance, would not be favoured for XRF detection, in the presence of much larger sand and silt-sized siliciclastics.

The second group of elements in Figure 2.7 A and 2.7 B are a product of biogenic and authigenic processes. The moderately strong covariance of S with Fe (FCM: $r = 0.41$, GOM: $r = 0.47$) suggests the authigenic production of iron sulphide minerals (pyrite, greigite), as observed by Moreno et al. (2007). The FCM shows a strong relationship between Sr and Ca ($r = 0.67$) but is considerably weaker in the gyttja ($r = 0.43$). The FCM Sr-Ca correlation indicates the presence of biogenic calcite and aragonite within the marl, including shell fragments. Within the GOM, it is likely that Sr signal is produced by autochthonous, eroded shell materials originating from the underlying marl, within the Unit 4 transgressive deposit. The ratio of Compton to Rayleigh scattering (inc/coh) can be used as a qualitative indicator of organic matter, as X-rays are attenuated proportionate to the water content and by association, the colloidal organic matter, within the core (Burnett et al. 2011; Löwemark et al. 2011).

In the FCM, S has a moderate correlation with Ni ($r = 0.32$), Sr ($r = 0.38$) and Ca ($r = 0.68$). These associations are a result of high S count values observed in marl lithofacies (Fig. 2.6). In the GOM, S has negligible associations with Sr ($r = 0.0017$) and Ni ($r = 0.11$), but a more significant positive correlation with Ca ($r = 0.41$). In both models, Ni has no significant correlation to Zr (FCM: $r = 0.079$; GOM: $r = 0.037$) and shares almost no relationship with Ti (FCM: $r = -0.15$; GOM: $r = 0.036$) and K (FCM: $r = -0.095$; GOM: $r = 0.0052$). In a modern context, Ni is often associated with anthropogenic contaminant inputs to lakes, as it is not readily introduced to lake systems in nature. The association with S in the FCM, suggests that at Rice Lake it is likely derived from the weathering and leaching of nickel-bearing sulphide minerals (eg. pentlandite, millerite) present

in igneous and metamorphic rock fragments in the surficial till deposits (Lintern et al. 2015).

Though six cores were chosen for chemostratigraphic analysis, SRPM-02 provides the most continuous and complete sediment record and was selected for detailed AMS radiocarbon chronology and thecamoebian analysis (Fig. 2.6). The trends observed within other cores of this study are also in agreement with the chemostratigraphic behavior of SRPM-02. Within Unit 7, Sr, S, Ca, and Ni are most dominant, diminishing sharply upward with a corresponding increase in Ti, K, and Fe within Unit 6, around 6600 cal BP. Unit 5 is characterized by a resurgence of marl minerogenic indicators (Ca, Sr, S), a low sedimentation rate (average 0.49 mm yr^{-1}), with evidence of waning carbonate production approaching the Unit 5–Unit 4 boundary (EH-2). Terrigenous elements increase, as the organic inter-beds thicken up-core, reaching peak intensities at EH-2. Marl facies (high Ca values) are replaced with progressively more organic sediment at 4600 cal BP, and terminates by 4400 cal BP. This is likely a result of diminishing forest litter acidity, observed by the slight decrease in pine pollen, and the rise in oak pollen from the nearby core 'E' of McAndrews (1984).

The Unit 4 transgressive shoreline deposit has the highest relative abundance of terrigenous elements, particularly Zr and Sr, consistent with the silt-rich gyttja observed in both the core brightness and lithofacies analysis. Sedimentation rate across this boundary increases to an average 0.58 mm yr^{-1} .

Unit 4 occupies roughly 300 years of the sediment record containing significant changes to elemental sources, best discussed using the gyttja correlation model (Fig. 2.7B). Ca becomes more strongly associated with terrigenous elements ($r = 0.32$ to $r = 0.58$), positively correlating with Si, Ti, and K, which were negatively correlated in the FCM (Fig. 2.7A). It is most likely allochthonous, and present in runoff from the limestone-bearing glacial till. S is more positively correlated to Ti ($r = 0.23$) and K ($r = 0.22$), but

still most likely complexing with Fe to form pyrite during times of greater nutrient input via erosion.

Sedimentation rates are heightened in Unit 3, averaging 0.76 mm yr^{-1} , and show oscillatory behavior in the terrigenous element profiles at centennial scales (Fig. 2.6). Nearing 3000 cal BP (1.36 m in SRPM02), there is a decrease in terrigenous input intensity, and an increase in the inc/coh ratio and Ni values, and the highest Ca peak within the gyttja, accompanied by an increase in coarse organic matter and no ephemeral laminations observed lower in Unit 3. Around this time, water levels at Rice Lake were approaching their pre-Dam levels, and the lower terrigenous input with slightly lower than average sedimentation rates ($\sim 0.6 \text{ mm yr}^{-1}$) could indicate a plateau in the water level trajectory of the lake (Sonnenburg et al. 2013).

The gradational Unit 2–Unit 3 contact is sharply punctuated geochemically by an increase in detrital elements, but with no proportionate increase in S to Fe. The inc/coh ratio sharply declines, with an increase in core brightness, within a muddy, massive gyttja. Average sedimentation rate exceeds 1 mm yr^{-1} (1.13 mm yr^{-1}), greater than immediately post-EH-2 sedimentation rates. The lower section of Unit 2 coincides with the Serpent Mounds occupation (2200–1300 BP), with two distinct peaks in terrigenous input: a smaller one at the beginning (2200 cal BP; 1.14 m) and larger at the end (1350 cal BP; 0.78 m). This potentially reflects landscape modification for burial mound construction, with intensity which increases proportionate to duration of site usage. After this interval, sedimentation declined to approximately 1 mm yr^{-1} , with a corresponding drop in terrigenous element values.

Unit 1 closely reflects the Serpent Mounds event in Unit 2, in magnitude but not duration. The construction of the Hastings Dam in 1838 CE is marked by a spike in S, and the highest terrigenous element values since the Middle Woodland. This occurs at approximately the same depth as the *Ambrosia* horizon observed by Yu and McAndrews

(1994). Euro-Canadian land modification is distinctly rapid, and as the dam construction flooded Rice Lake, sedimentation rates increase to an average of 1.51 mm yr^{-1} . The high Ca values within the top 5 cm of SRPM-02 are due to modern shell fragments.

2.5.3 Chemofacies

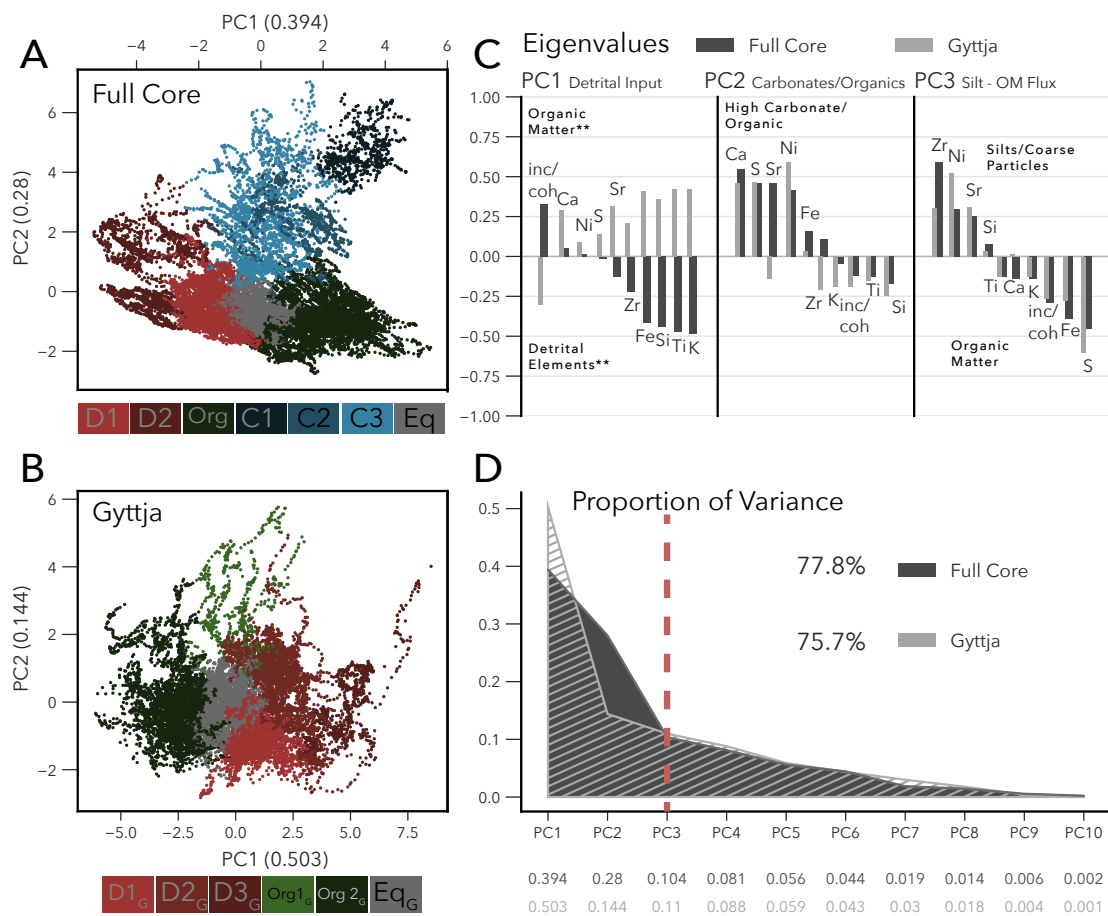


Figure 2.8: Results of principal component analysis (PCA) of elemental data for core SRPM02. **A.** Biplot plot of PC1 and PC2 for full-core model. **B.** Biplot of PC1 and PC2 for full-core for gytija only. **C.** PCA eigenvalues of the first three PCs ranked and plotted in descending order of the full-core model. **D.** Scree plots showing proportion of explained variance for full-core model (77.8%) versus gytija model (75.5%). Explained variance is the proportionate values of eigenvectors, where the variance contribution of each PC to the entire dataset is displayed as a ratio. **The sign of loadings for PC1 are inverse between the full-core and gytija models

The PCA and CA performed on six cores for both full-core and gyttja partitions, found most of the variance to be contributed within the first three PCs: 78%, and 76%, respectively (Fig. 2.8). Component selection was made arbitrarily, excluding variance contributions under 10%. Biplots of the two most contributing PCs (PC1 and PC2) are presented for visualization of cluster divisions (Fig. 2.8A and B). Figure 2.8C displays the eigenvalues of each element within the three respective principal components, in descending order of the FCM, with comparative GOM loadings superimposed. The loadings plots explain the largest contributing elements, and what influence they have on the values (positive or negative) of principal components with values given in standard deviations. Figure 2.8D shows the scree plot of the ten components. Substantially greater explanatory weight is placed on PC1 (50.3%) of the GOM, and less on PC2 (14.4%). Within the FCM, PC2 explains almost twice as much variance (28%).

PC1 is interpreted as terrigenous (minerogetic) element input, and shows significant negative loadings from terrigenous elements in the FCM, with minimal influence from Ni, S, and Sr, and negative loadings from the inc/coh ratio. The sign of the loadings are inverse for the GOM, and Ca and Sr contribute significantly more to the terrigenous fraction (Fig. 2.8C).

PC2 reflects the change in elements associated with biogenic and authigenic minerals and organic matter, with significant positive loadings contributed by Ca, S, Sr, and Ni, and weak negative loadings from terrigenous elements. The GOM shows similar trends, with the exception of Sr, which is weakly negative, and shares a loadings magnitude with the terrigenous indicators.

PC3 is interpreted as the flux between weathered and eroded aluminosilicate minerals in soil, and organic productivity. The former is represented as strong positive loadings of Zr (0.6), Ni (0.28), and Sr (0.5), and the latter by strong negative loadings of Fe (-0.34), S (-0.45), and the inc/coh ratio (-0.28). Ni shows much stronger positive

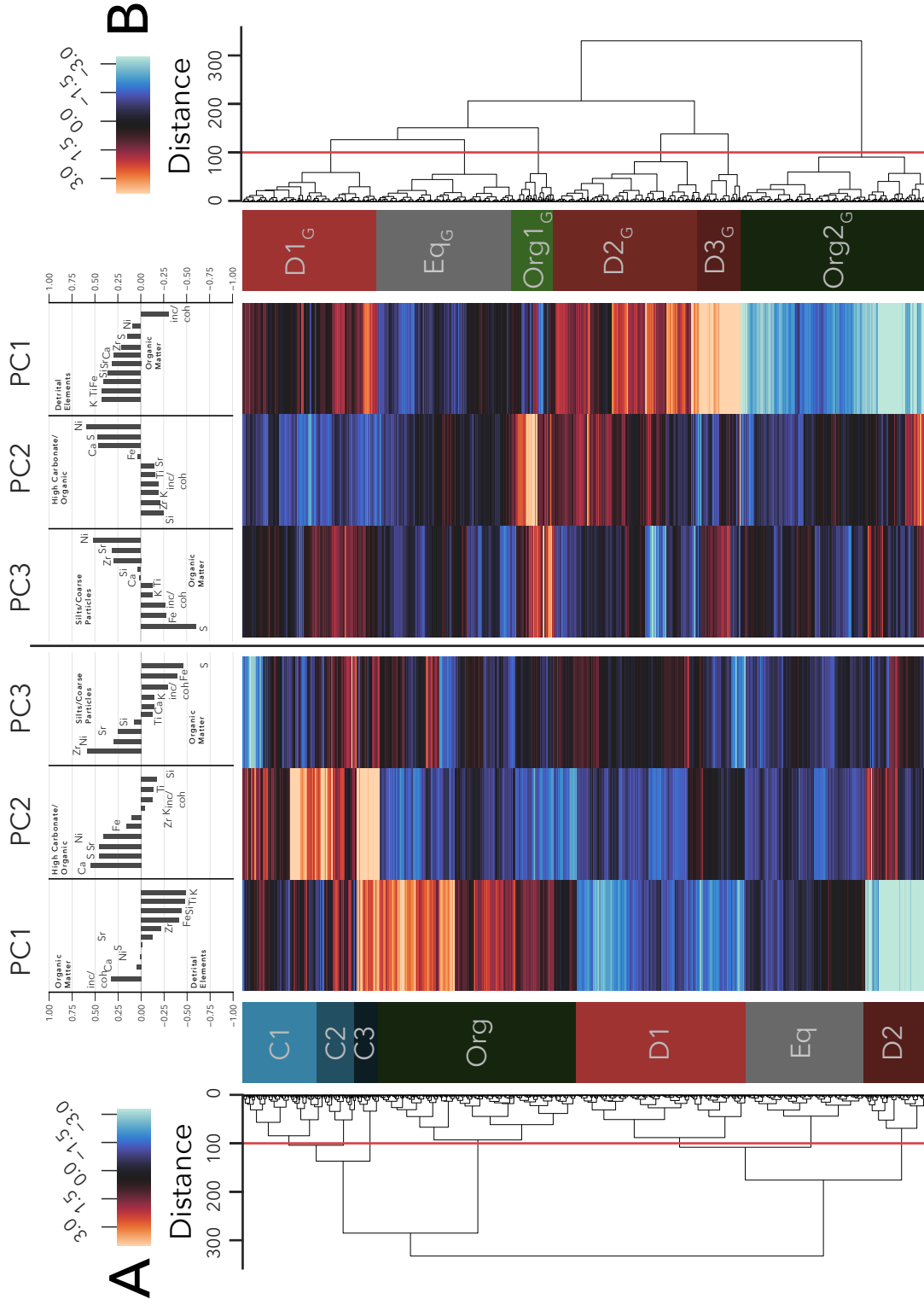


Figure 2.9: Heatmap and Q-mode Euclidean Distance cluster (Ward's method) of the first three PCs of both full-core model A. and gytjja model B..

loadings in the GOM (0.51). Fe and S in PC3 represent pyrite production, which will increase with greater values of Compton scattering representing core organic matter.

These PCs were used to determine 7 distinct clusters within the FCM, and 6 within the GOM. Clusters were grouped into broader classifications related to environmental processes. Clustering principal components eliminates covariance issues, and provides a dimensionally reduced dataset, restricted to only the most important explanatory variables of the data (Fig. 2.9). Figure 2.10 displays the standardized elemental data used in the PCA, grouped by chemofacies.

2.5.3.1 FCM Chemofacies

2.5.3.2 Detrital Input

Chemofacies D1 and D2 indicate increasing intensity of detrital input, primarily determined through the magnitude of negative loadings in PC1 ($\bar{x} = -1.55\sigma$ and -3.60σ respectively). The element profiles of D1 show large positive values for terrigenous elements ($\bar{x} = 0.5 - 0.8\sigma$), and low values for biogenic elements ($\bar{x} = -0.29\sigma - -0.49\sigma$). Chemofacies D1 coincides with estimated age range of the Serpent Mounds occupation (Fig. 2.11). D1 differs from D2 primarily in the abundance of Zr ($\bar{x} D1 = 0.35\sigma$; $\bar{x} D2 = 1.12\sigma$) and Sr ($\bar{x} D1 = -0.1\sigma$; $\bar{x} D2 = 1.11\sigma$), which is of higher count values in D2. All terrigenous element values for D2 are substantial ($\bar{x} 1.12\sigma - 1.69\sigma$) (Fig. 9A), and as such, D2 is mostly representative of Unit 4 lithofacies, with some presence in the Point Peninsula zone (Fig. 2.11A).

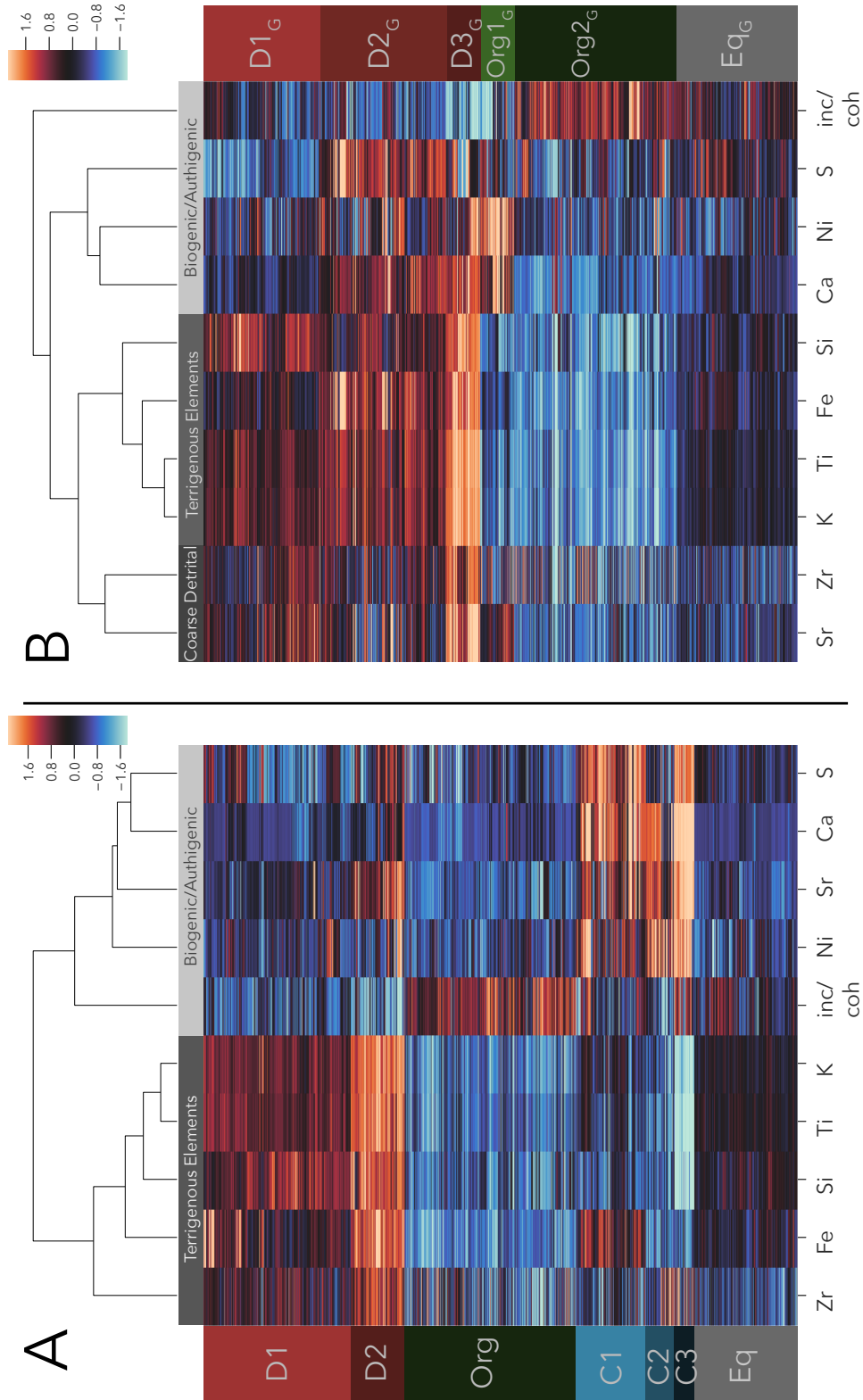


Figure 2.10: Heatmap and R-mode cluster (Ward's Method with Euclidean distance metric) for elements in the full-core model **A**, and gytija model **B**, sorted by chemofacies affiliation.

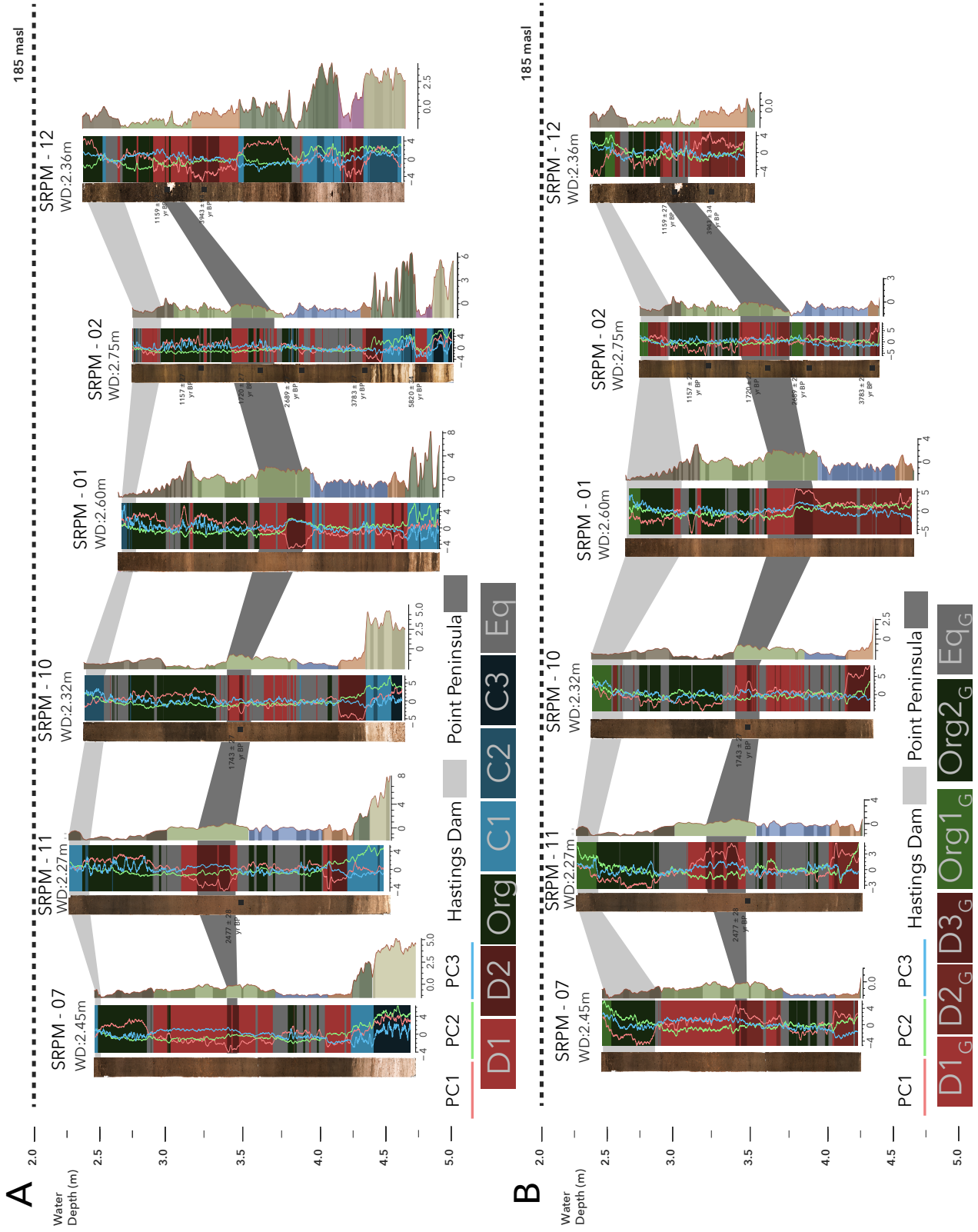


Figure 2.11: Chemofacies clusters plotted for full-core model **A**. and gyttja model **B**. Line plots show contributions of three principal components for each core.

2.5.3.3 Organic Productivity (Org)

These chemofacies reflect periods of low sediment input, and increasing organic matter (inc/coh \bar{x} = 0.83σ). As such, this cluster was discerned for consistently positive PC1 values (\bar{x} = 1.96σ), and includes all sediment where the inc/coh ratio was distinctly high (Fig. 2.9A). The carbonate content of this facies however is deemed to be low, as PC2 values \bar{x} -1.04σ , and sparse Ca (\bar{x} = -0.5σ) and Sr (\bar{x} = -0.7σ) (Fig. 9A). The Organic facies is most common in the uppermost Unit 2 and Unit 1, following the Point Peninsula occupations.

2.5.3.4 Carbonate Facies (C1, C2, C3)

These facies divide the marl lithologies, and are almost exclusive to Unit 7 and Unit 5, with some exceptions for shell fragments captured within the top gyttja (Fig. 2.11A). C1 has values of PC1 (\bar{x} = 0.11σ) near the sample mean, and PC3 (\bar{x} = -0.8σ) values which suggest greater organic productivity. PC2, however, is very high, with an average of 2.35σ . C2 has slightly lower \bar{x} PC2 values (1.94σ) but is indicative of higher organic content, and detrital input within the marl, with an \bar{x} PC1 of 1.02σ and \bar{x} PC3 of 1.55σ . The positive average values for all three principal components indicate C2 may be linked to wetter periods, with larger volumes of runoff bringing both organic matter, and aluminosilicate minerals rich in Zr (0.43σ) and Ni (1.56σ). C3 is the most carbonate and organic-rich of the three, with a much larger average PC1 (3.18σ), and PC2 (4.59σ), but the closest \bar{x} PC3 value to 0 at 0.79σ , indicating little flux between organic productivity and weathered detrital elements. The average Ca and Sr values of C3 are the highest of the three, at 2.38σ and 2.28σ , respectively. C2 was not present in SRPM-07, and C3 was not present in SRPM-11 and SRPM12 (Fig. 2.11).

2.5.3.5 Geochemical Stasis (Eq)

All core segments with no marked increase in either organic productivity, or terrigenous input were allocated to the 'Eq' facies, representative of intervals which experience roughly equal magnitude and sign from all three principal components. These facies hold average values which are weakly negative ($\bar{x}PC1 = -0.12\sigma$; $\bar{x}PC2 = -0.82\sigma$; $\bar{x}PC3 = -0.44\sigma$), but in most profiles as seen in Figure 2.11A, PC values remain around $\bar{x}_a(0)$. Intervals characterized by this chemofacies are prominent in Unit 3, appearing above the Unit 4 transgressive deposit in all cores except SRPM-01 and SRPM-12.

2.5.3.6 GOM Chemofacies

2.5.3.7 Detrital Input

Eliminating marl lithologies from the analysis allowed for better cluster discrimination within the gyttja, specifically between facies of increasing sediment input. D1_G shares many of the same attributes to its full-core counterpart, but contains less of a sediment excursion, with an $\bar{x}PC1$ of 0.90σ . Average values for all elements of D1_G in Figure 2.10B remain within 1σ of the mean. D2_G contains substantially higher average values of PC1 (1.87σ), but is distinct for its high average S (1.02σ) and Fe (0.98σ) content and low $\bar{x}PC3$ (-0.67σ) suggesting Fe from pyrite production plays a significant role in this chemofacies. D3_G, much like D2 is found in few places other than the bottom gyttja in Unit 4 (Fig. 2.11B). Average values for PC1 in D3_G are the highest of the three detrital facies at 4.70σ , but there is negligible contribution from PC2 ($\bar{x} = -0.15\sigma$). A moderate contribution from PC3 ($\bar{x} = 0.78\sigma$), is a consequence of heightened Zr ($\bar{x} = 1.31\sigma$), Sr ($\bar{x} = 1.99\sigma$) and Ni ($\bar{x} = 0.66\sigma$) within the transgressive deposit, but also appears strongly within SRPM-10 and SRPM-11 within the Middle Woodland aged deposits.

2.5.3.8 Organic Productivity

Two organic-rich chemofacies were discerned in the GOM. Org1_G is found in the uppermost 10–15 cm of Unit 1 (Fig. 2.11B), and is distinguished by lower average inc/coh values than Org2_G (-1.08σ versus 0.87σ), high average Sr (0.46σ), Ca (1.24σ), and Ni (1.84σ) (Fig. 2.10B). The location of Org1_G in the upper section of Unit 1 geochemically relates it to C1 and C2 of the FCM, but without marl lithologies to obscure chemofacies relationships, the sources of these high elemental values may be discerned. The Ca and Sr is likely from shell fragments observed in Unit 1 which post-date the Hastings Dam construction. Chronologically, this means that the high Ni values may be related to the presence of Euro-Canadian settlers in the late 19th century. Org2_G is similar to Org in the FCM, such that it encompasses all intervals of high inc/coh ratio ($\bar{x} = 0.87\sigma$). Likewise, it also has very low input from terrigenous elements ($\bar{x}PC1 = -2.7\sigma$). In Figure 2.11B, it is observed in roughly the same lithological positions as occupied by Org in Figure 2.11A.

2.5.3.9 Geochemical Stasis

The GOM also contains areas of geochemical equilibrium, where the values of all three PCs are close to \bar{x}_a , indicating little change in either detrital input or organic productivity (Fig. 2.9B). Again, a slight negative trend in average PC values is observed (PC1 = -0.49σ ; PC2 = -0.13σ ; PC3 = -0.51σ). Divergence from the FCM are observed in the lower average values of Ti (-0.06σ) and K (-0.07σ), but higher average S (0.13σ) (Fig. 2.10B).

2.5.4 Thecamoebian biofacies

The results of R- and Q-mode cluster analysis are shown as a heat map in Figure 2.13. In this plot, the colour scale indicates the fractional abundance. The R-mode clustering divided the taxa into two major groups, one containing 7 taxa which are in low abundance (< 8%), and a second containing 8 abundant taxa that account for 10–50% (Fig. 2.13). The group of rare and less abundant taxa showed a very close relationship between all species, with the exception of *P. compressa*, which clustered separately. Within the abundant taxa, three distinct sub-clusters were formed. The first sub-cluster contains three Centropyxids (*C. constricta* 'aerophila', *C. aculeata* 'aculeata' and *C. constricta* 'spinosa'), often associated with stressed conditions, and the most abundant species in the Unit 4 transgressive shoreline deposit (Fig. 2.12) (Dallimore et al. 2000; Sonnenburg et al. 2013).

The second sub-cluster contains *D. oblonga*, *C. aculeata* 'discoides', and *C. tricuspis*, all of which are indicators of eutrophic conditions (Reinhardt et al. 2005; Roe et al. 2010).

The remaining two taxa in the dominant cluster, comprising the third sub-cluster, are *A. vulgaris* and *D. proteiformis* 'amphoralis'. The latter is relatively ubiquitous throughout the core, except in Unit 4, but of greatest abundance in clusters B4 and B5 (Fig. 2.13). *A. vulgaris* has two prominent spikes in abundance (20–50%) which correspond to major transitions identified in the elemental PCA clustering: one ca. 2713 cal BP, and one coinciding with the construction of the Hastings Dam. *A. vulgaris* is most dominant in B1 and B2, where *D. proteiformis* 'amphoralis' is diminished. Q-mode clustering identified five distinct thecamoebian biofacies which include: transgressive shoreline (B1), turbid shallow lake (B2), post-dam eutrophic lake (B3), marginal wetland (B4) and pre-contact eutrophic lake biofacies (B5) (Fig. 2.13).

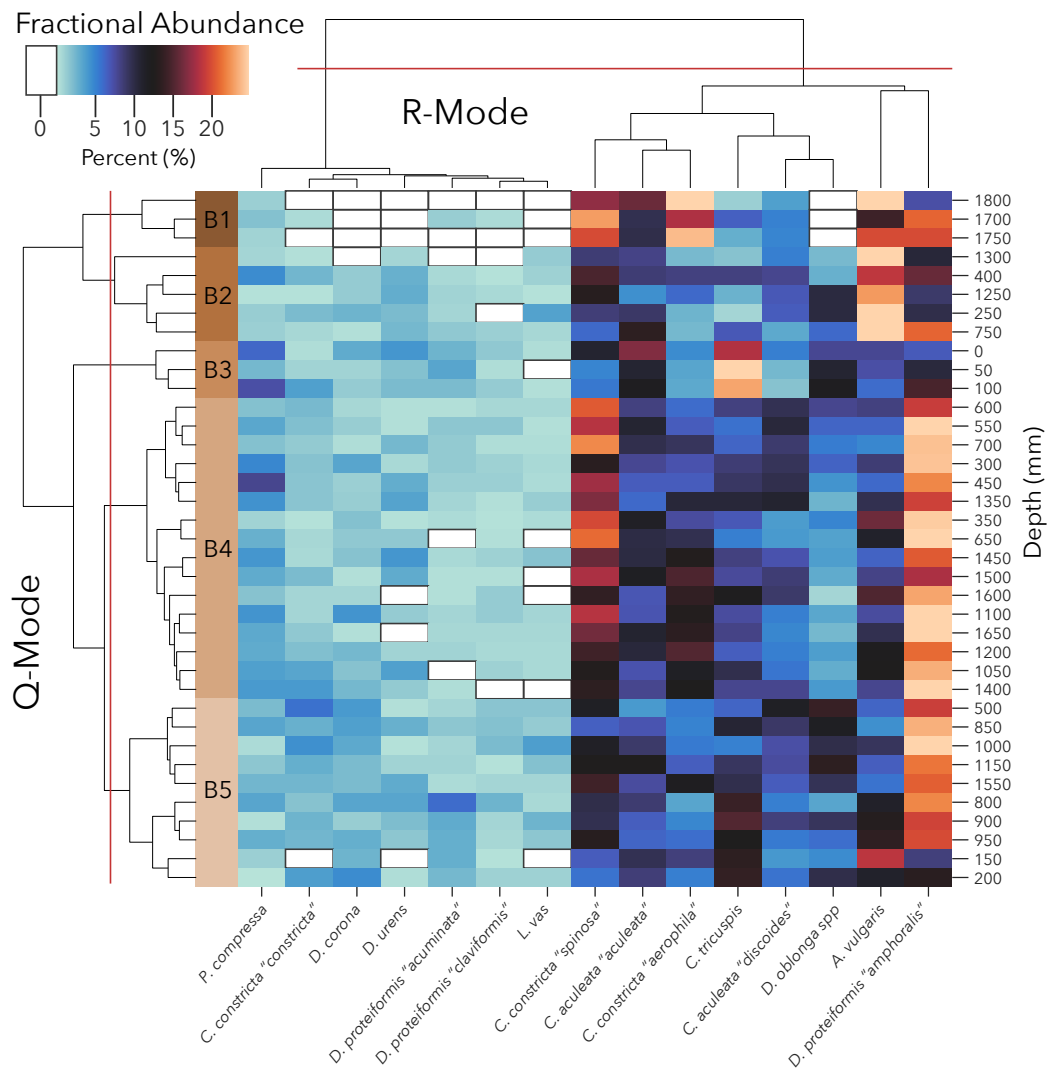


Figure 2.13: Thecamoebian biofacies clusters identified by Q- and R-mode cluster analysis (Ward's Method with Euclidean distance metric). Fractional (%) abundances are shown as heatmap.

Table 2.2: Summary of average fractional abundance and their standard deviations for each of the biofacies.

Biofacies	B1		B2		B3		B4		B5	
	mean	$\pm 2\sigma$								
Counts per cc	276	38	959	295	1091	273	485	93	645	133
Diversity (SDI)	1.88	0.08	1.99	0.27	2.26	0.11	2.25	0.13	2.31	0.06
<i>A. vulgaris</i>	18.61	3.48	32.69	12.06	6.95	0.77	9.32	3.15	9.82	4.09
<i>C. aculeata</i> "aculeata"	11.59	2.78	9.63	2.08	12.95	2.49	8.88	1.85	7.86	2.10
<i>C. aculeata</i> "discoides"	5.04	0.14	5.69	1.72	3.12	1.44	7.27	2.27	7.01	2.05
<i>C. constricta</i> "aerophila"	22.33	3.35	3.89	2.47	3.73	0.64	10.75	2.80	6.13	2.25
<i>C. constricta</i> "constricta"	0.21	0.30	1.49	0.87	1.70	1.37	1.71	0.93	2.90	1.45
<i>C. constricta</i> "spinosa"	19.65	2.07	9.34	3.16	7.02	2.66	16.46	2.77	9.98	2.78
<i>C. tricuspis</i>	4.53	1.42	4.43	3.11	24.04	5.64	7.92	1.74	10.77	3.14
<i>D. corona</i>	–	–	1.12	1.02	1.80	0.92	1.70	1.03	2.99	0.91
<i>D. oblonga</i>	–	–	5.33	3.11	10.05	1.72	3.80	1.38	9.02	3.31
<i>D. proteiformis</i> "acuminata"	0.42	0.60	0.80	0.57	2.74	0.48	0.81	0.48	2.23	1.53
<i>D. proteiformis</i> "amphoralis"	15.85	5.74	14.01	4.35	10.45	3.19	22.79	2.49	19.01	4.70
<i>D. proteiformis</i> "claviformis"	0.50	0.37	0.39	0.49	1.13	0.46	0.83	0.47	1.28	0.75
<i>D. urens</i>	–	–	2.09	0.71	2.77	0.95	1.78	1.36	1.53	1.19
<i>L. vas</i>	–	–	1.70	1.08	0.32	0.23	0.61	0.50	1.59	1.00
<i>P. compressa</i>	1.25	0.47	2.02	1.50	5.27	2.06	3.53	1.51	1.84	1.12

2.5.4.1 Transgressive Shoreline (B1)

Biofacies B1 is dominated by *C. constricta* 'aerophila' (22.3%) and *A. vulgaris* (18.6%). *C. tricuspis* (4.5%) and *D. oblonga* is absent, indicating a low nutrients conditions in the environment (Reinhardt et al. 2005). The total number of specimens in B1 was the lowest of the five assemblages identified ($\bar{x} = 276$ per cc) and had the lowest diversity (average Shannon diversity index (\bar{x} SDI) = 1.88), indicating a low nutrient environment with a moderate degree of ecosystem stress (Patterson and Kumar 2000). Biofacies B1 occurs within Unit 4, identified as a transgressive shoreline deposit that records the rise in water levels following the mid-Holocene lowstand (Yu and McAndrews 1994; Sonnenburg et al. 2012).

2.5.4.2 Turbid shallow lake (B2)

B2 is composed of large numbers of *A. vulgaris* (32.9%), followed by *D. proteiformis* 'amphoralis' (14%), and *C. aculeata* 'aculeata' (9.6%) and *C. constricta* 'spinosa' (9.3%). Taxa within the minor R-mode cluster, are in very low abundances with the exception of *D. urens*, reaching a maximum of 2% (Table 2.2). *D. urens* has been found in great abundance in the surface sediments of shallow (1.5–3.5m) Midway Lake (Nova Scotia), where sedimentation rates were noted to be substantial by Patterson et al. (1985). The mean sedimentation rate during the B2 intervals is 0.97 mm yr^{-1} , which is considerably high (Fig. 2.12).

Biofacies B2 is associated with turbid conditions, and appears to coincide with lithological unit divisions in SRPM-02. B2 marks the boundaries of Unit 2–Unit 3 (1295 cal BP), and Unit 1–Unit 2 (~1838 CE). Additional occurrences coincide with the end of the Point Peninsula occupation (75 cm) with an additional spike along a seed-rich interval at 40–42.5 cm in Unit 2 of SRPM-02. These zones are characterized by a drop in \bar{x} SDI (1.99), and a rise in total specimens per cc (959) (Table 2.2). The drop in *D. proteiformis* 'amphoralis' is key, as this species forms the 'background' species of the assemblage, and preferably inhabits muddy substrates with an abundance of pennate diatoms, which is typical of Rice Lake gyttja (Patterson and Kumar 2000). The B2 intervals, which punctuate SRPM-02, coincide with periods of increasing PC3 (Fig. 2.12) which infer a textural change toward coarser silts may be present, which is not conducive to 'amphoralis' growth. Another indication of shoaling conditions is the decreased abundance of *D. proteiformis* 'claviformis' (0.39%) which is noted to inhabit deeper waters in modern contexts (Reinhardt et al. 1998).

2.5.5 Post-Dam eutrophic lake (B3)

Biofacies B3 contains the highest average abundance of *C. tricuspis* (24%) in the assemblage (Table 2.2). B3 also contains the highest average abundance of *P. compressa* (5.27%) (Table 2.2), a forest soil-dwelling species, further indicative of Euro-Canadian land clearance activity (Hawkes et al. 2005; Sonnenburg and Boyce 2008). *C. aculeata* 'aculeata' (12.95%) and *D. oblonga* (10%) also play a dominant role in this biofacies. B3 has the highest counts per cc (1091) and \bar{x} SDI (2.26) (Table 2.2).

B3 is found at the top 15 cm of SRPM02, follow the flooding of Rice Lake, and the inundation of much of the past shoreline. Typical of lakes eutrophied by European settlement, *C. tricuspis* reaches peak abundance only slightly after the *Ambrosia* horizon found in Core E (see Fig. 5 in McAndrews (1984)), nearby (Fig. 2.2) (Yu and McAndrews 1994; Reinhardt et al. 2005). Land clearance, forestry, and agriculture in the area compounded the environmental stress from flooding, increasing sedimentation rates substantially (1.82 mm yr⁻¹ in upper Unit 1).

2.5.5.1 Marginal Wetland (B4)

Biofacies B4 comprises a diverse assemblage dominated by *D. proteiformis* 'amphoralis' (22.8%), *C. constricta* 'spinosa' (16.5%), and *C. constricta* 'aerophila' (10.8%). B4 contains the next lowest average counts per cc after B1, at 485, but with the second highest \bar{x} SDI of 2.25 (Table 2.2).

B4 occurs twice within SRPM-02: immediately following the transgressive horizon above EH-2, and after the Point Peninsula occupation. Minor taxa make their first appearance, and several nutrient-loving species, formerly scarce in Unit 4, gain a foothold. The presence of B4 does not appear restricted by chemofacies, as it occupies D2_G, Org1_G

and Eq_G. The rapid establishment of *D. proteiformis* 'amphoralis' during this time aligns with textural changes transitioning from the silt-rich Unit 4, to muddier Unit 3.

2.5.5.2 Pre-colonial Eutrophic Lake (B5)

B5 is distinguished by abundant *D. oblonga* (9%), a rise in *C. tricuspis* (10.7%) which is second highest to abundances observed in B3, and the most dominant species is *D. proteiformis* 'amphoralis' (19%). The mean specimens per cc is slightly higher than B4, at 645 per cc, but with a lower \bar{x} SDI of 2.31 (Table 2.2).

B5 coincides with the prolonged interval of chemofacies D1_G and D2_G which mark the onset and end of the Serpent Mounds occupation (Fig. 2.13). The increase in *C. tricuspis* and *D. oblonga* during this time indicate an increase in nutrient input, shifting towards eutrophic conditions at a time before European settlement. Sedimentation rates concurrently increase to an average 1.3 mm yr⁻¹, which if attributed to nutrient loading from soil erosion, would explain the elevated abundance of eutrophic-tolerant species. B5 also appears around the time of European arrival at Rice Lake, and is synchronous with the ragweed pollen zone identified by McAndrews (1984) (Fig. 2.12).

2.6 Discussion

2.6.1 Late Holocene Water Levels and Paleogeography

The reconstructed water level curve and paleogeographic maps showing the lake paleobathymetry and shoreline positions for three selected time periods are shown in Figure 2.14. The maps show the estimated maximum and minimum elevations of the paleoshorelines relative to the modern lake level (~187 m asl) for each interval. The maps

also show the areas with optimal water depths for the growth of wild rice (0.5–1m) (Finkelstein and Davis 2006), which we use to estimate wild rice food resources available during each period. The water levels and paleoenvironmental changes during these intervals are summarized in the following sections.

2.6.2 Mid-Holocene Shoreline Transgression (4500 – 3300 cal BP)

During the mid-Holocene lowstand water levels were more than 5 m bpl (ca. 5800 BP) and the lake was hydrologically closed, as a result of a dry Hypsithermal climate (Fig. 2.14A) (Sonnenburg et al. 2012). After 4500 BP, water levels had begun to rise and the shoreline was transgressing as a result of a shift to a cooler, wetter Neoglacial climate (Yu and McAndrews 1994; Sonnenburg et al. 2013). The end of the Hypsithermal is signalled by the end of marl production, as indicated a sharp decrease in Ca at 1.8 m in core SRPM-02 (ca. 4450 cal BP) (Fig. 2.6). Lake levels recovered rapidly in the late Archaic period (Fig. 2.14A), but our reconstruction places levels at about 1 metre lower at 3800 BP than the estimates of Sonnenburg et al. (2012), which were based in part on core data from McAndrews (1984). We suspect this difference is due to uncorrected core compaction in the earlier study, which we determined in our cores to be as much as 55%, and which can result in a significant underestimation of the AMS sample depth and water plane elevation if not corrected. The paleobathymetric map for this interval indicate water levels were about 4 m bpl (183 m asl) at 4500 BP and the area to the east and west of Serpent Mounds was low lying marsh habitat.

Following EH-2 water levels began to rebound, but remained below the Hastings outlet sill (185 m asl) at just over 183 m asl. At the time, thecamoebian biofacies B1 was dominant, with only highly resilient species *A. vulgaris* and various Centropyxids in abundance. The geochemical record for most cores is within D2_G or D3_G (Fig. 2.11),

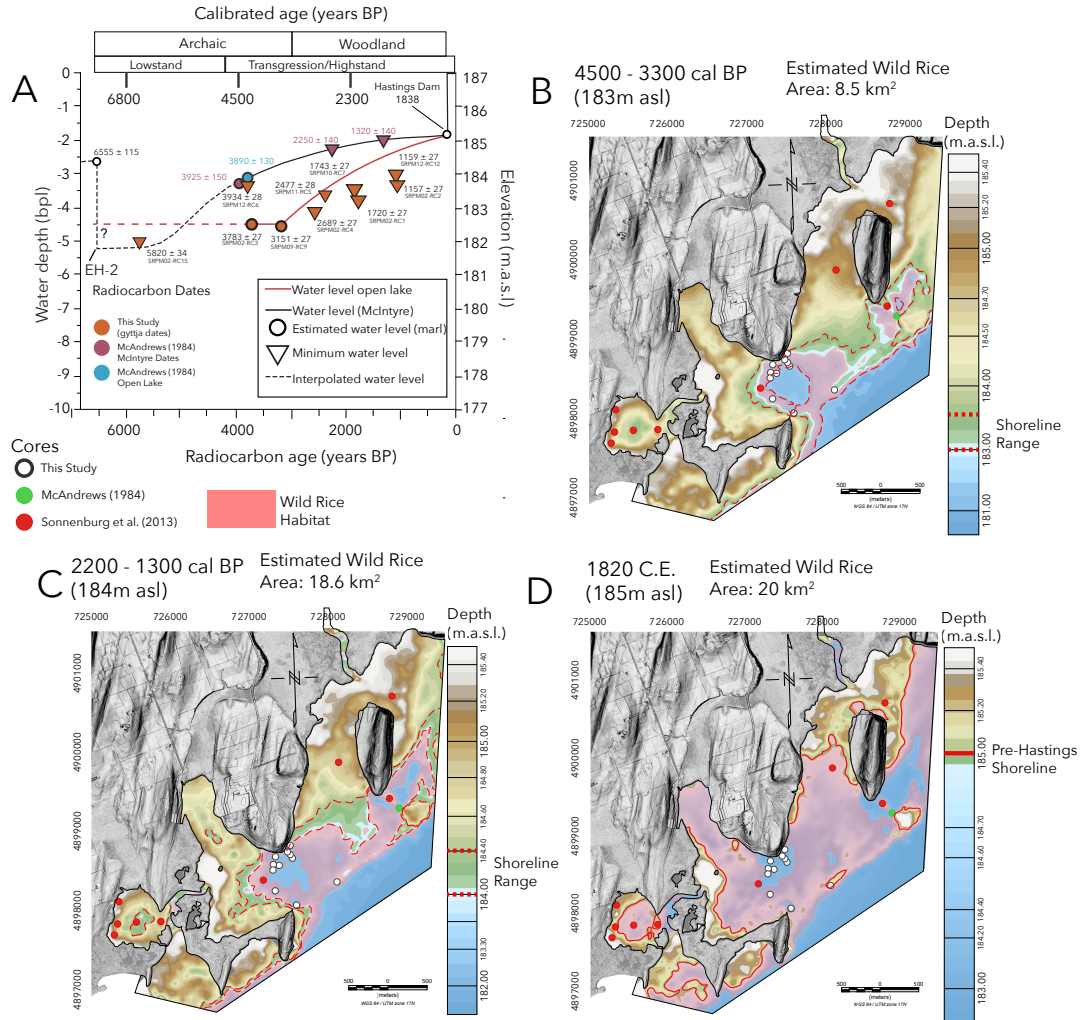


Figure 2.14: **A.** Reconstructed lake levels to 6000 yrBP with water level curve (Fig. 3 in Sonnenburg et al. (2013), with data from Yu and McAndrews (1994)) for comparison. Water levels based on ¹⁴C dates in transgressive shoreline deposit (Unit 4) and dates from upper gyttja sequence (Units 2,3), which provide estimate of minimum water levels during the Woodland Period and up to the Hastings Dam flooding (1838 CE). Water level curve of Sonnenburg et al. (2013) predicts a 1.5 m higher water level at 4500 yBP, possibly as a result of uncorrected core compaction. Paleogeographic maps show estimated water levels and shoreline positions: **B.** Mid-Holocene shoreline transgression following lowstand phase ca. 4500–3300 cal BP, **C.** Middle Woodland Point Peninsula occupation ca. 2200–1300 cal BP, **D.** European settlement phase (pre-dam) ca. 1820 CE. Areas with water depths suitable for wild rice stands (0.1–1m depths) shown in pink. The increase in the wild rice habitat was likely a major determinant in the occupation of the site beginning in the Middle Woodland period.

coupled with higher sedimentation rates (0.73 mm yr^{-1}), but with some iron sulfide production typical of shallow wetlands (evidenced by $D2_G$) (Haaijer et al. 2007).

Zr, Sr, Si, Ti, and K are most abundant at the base of Unit 4 (RC3; 4163 cal BP), but subside upon transitioning to Eq_G facies in all core but SRPM-01, which enters $D2_G$ facies attributed to high S content throughout Unit 3. Simultaneously, Biofacies B4 becomes dominant, increasing species diversity, and indicating a less silty substrate with the suddenly high abundance of *D. proteiformis 'amphoralis'*. The geochemical profile of SRPM-02 (Fig. 2.15) shows centennial-scale oscillations in heavier detrital input as water levels continued to recover through the Early Woodland.

The climate at this time was in a cooling trend, and gradually became more moist, aiding in water level recovery at Rice Lake (Marlon et al. 2017). The upland pine forest was in decline and was being replaced by deciduous vegetation (oak, beech, birch and maple), while the shallow areas of the lake became dominated by grasses (Yu and McAndrews 1994). According to McAndrews (1984), the establishment of wild rice was near synchronous with the recovery of water levels post-EH-2 elsewhere, but the paleobathymetric reconstruction of Figure 2.14B shows approximately 850 ha of viable growth area within the study site, long before water levels had recovered at McIntyre (Sonnenburg et al. 2013).

2.6.3 Middle Woodland Point Peninsula Occupation (2200 – 1300 cal BP)

The oscillatory trend observed in the last phase continues until a brief interval of increasing organic productivity ($Org1_G$) (Fig. 2.15). A sudden shift to $D1_G$ and $D2_G$ chemofacies occurs in all cores, roughly around the same time as the onset of Point Peninsula culture expansion at Rice Lake (Fig. 2.11B). All terrigenous elements in SRPM-02 intensify in the first of two distinct sedimentation episodes during the estimated occupation window

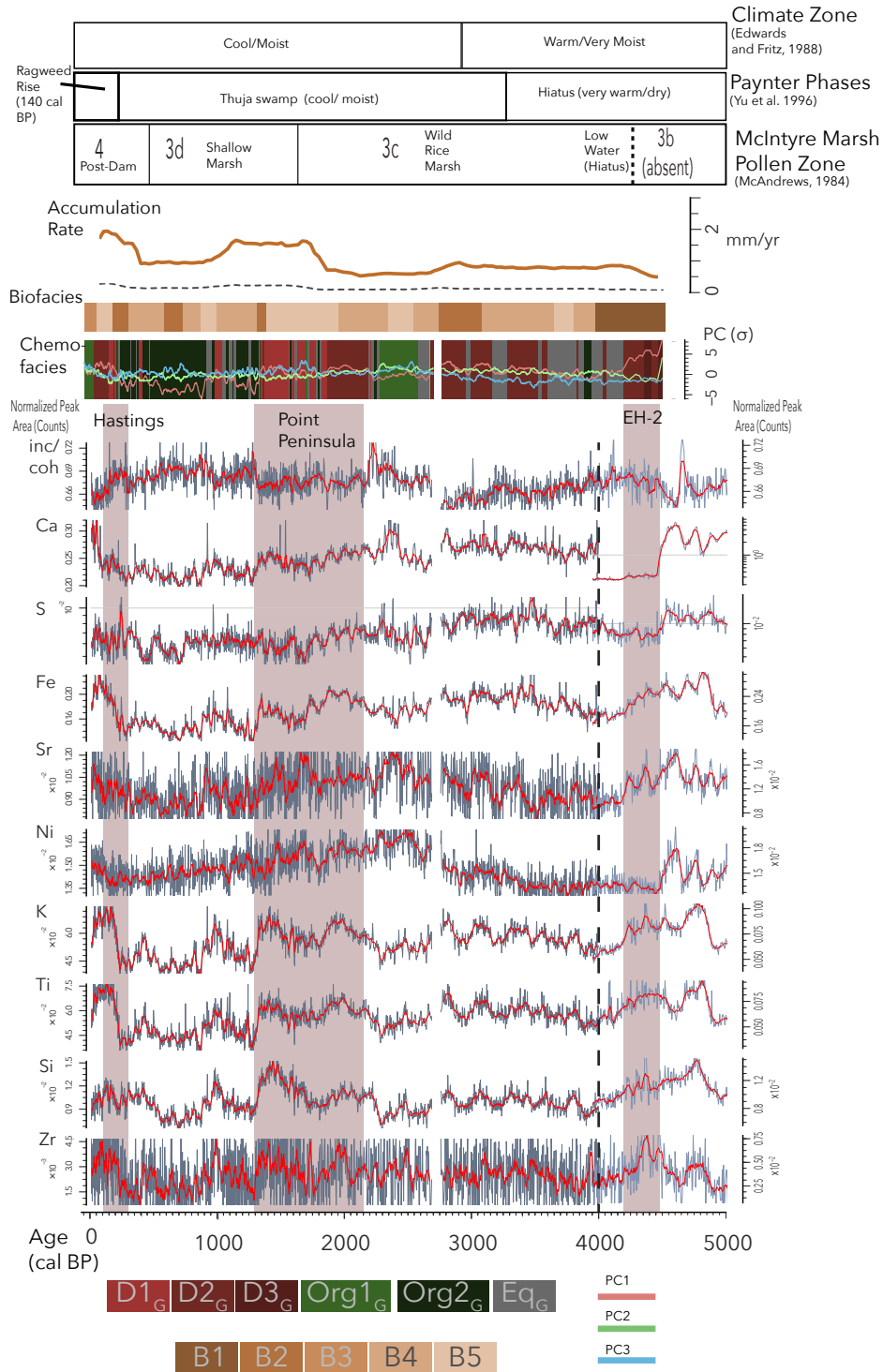


Figure 2.15: SRPM02 elemental data plotted by age with chemofacies and biofacies clusters, and accumulation rates through time. Normalized spectra (black traces) are plotted with a superimposed 100-year moving average in red. Paleoenvironmental interpretations from McAndrews (1984), Yu et al. (1996) and regional climate from Edwards and Fritz (1988) for comparison. Elemental data is plotted with a 10-year moving average.

of Serpent Mounds, but this episode is detected in all cores within the study area, but diminishing in a radial pattern from Roach Point. In SRPM-02, the initial sedimentation episode is accompanied by D2_G, which indicates elevated S counts with the simultaneous increase in terrigenous input, and high counts of *C. constricta* 'aerophila' and 'spinosa' (~15% each), indicative of sudden ecosystem stress. In other cores, this interval is punctuated by D3_G, which indicates peak detrital input on the same order of magnitude as the transgressive horizon (Fig. 2.11B).

At around 1630 cal BP, the middle of the Serpent Mounds occupation, a rapid change in sedimentation rate occurs (\bar{x} 0.57 mm yr⁻¹–1.46 mm yr⁻¹). After briefly subsiding in SRPM-02, a second, larger excursion in terrigenous elements continues until just after 1300 cal BP, when Serpent Mounds is thought to have been unoccupied (Johnston 1968). The abundance of *C. tricuspis* and *D. oblonga* increase to ~15% and ~10%, respectively, proportionate to the intensifying of detrital input, suggesting an increase in soil nutrient loading in the lake. Declining fractional abundance of marsh dwelling species *C. constricta* 'spinosa', and similar behavior of *C. constricta* 'aerophila' populations was observed through the second excursion. Populations drop to 3% and 10% respectively therein, from 13% and 18% within the first (Fig. 2.12). Reinhardt et al. (2005) note *C. constricta* 'aerophila' to be significant within marsh strata at Frenchman's Bay (Ontario). Intensifying human activity at Serpent Mounds from shellfish gathering and amplified erosion caused some marsh habitat reduction toward 1300 cal BP, reflected in the *C. constricta* 'aerophila' decline.

Figure 2.14C depicts the relative shoreline position during the occupation period of many sites in the area. Much of the area between East Sugar Island and Roach Point would have been traversable on foot, connecting the mounds on both. The viable growth area for wild rice expanded greatly to encompass a total 1860 ha. Immediately after 1300 cal BP, there is a sharp decline in the magnitude of PC1 across all cores, and

specifically, in SRPM-02, the inc / coh ratio values sharply increase, signalling a less silty lithology.

2.6.4 European Settlement Phase (ca. 1820 CE)

Rice Lake's first European inhabitants arrived ca. 1820 CE, and by 1838 CE, large tracts of forest had been cleared for agriculture, and a dam was built at the lake outlet in Hastings (Hastings Dam; Fig. 2.1). Prior to dam construction water levels were about 1.8–2m below present and about 2000 ha of viable wild rice habitat was available around Serpent Mounds. The accounts of European settlers testify to the abundance of wild rice. Following dam construction in 1838, water levels rose rapidly and the wild rice stocks declined significantly in the lake (Sonnenburg 2010). This dam construction is reflected in the geochemical record by a brief, but intense episode of sedimentation, roughly recorded at the Unit 2–Unit 1 boundary (Fig. 2.11B). Afterward, eutrophic facies are established, with substantially less detrital input. The pre-dam sedimentation rate is estimated to range between 0.9–1 mm yr⁻¹, but increases to between 1.65–1.89 mm yr⁻¹ following construction.

The thecamoebian assemblage changes accordingly to B3, to an assemblage with the highest abundance of *C. tricuspis* observed through all biofacies (24%) (Fig. 2.12). The flooding was preferential to the health of *Centropyxis*, *D. oblonga* and *D. corona* more so than *D. proteiformis 'amphoralis'*, which reaches its lowest average abundance in B3 (10.45%), where its dominance was ubiquitous in all other non-transgression (B1) assemblages (Table 2.2). The magnitude of the Hastings geochemical signal is equal to that of the Middle Woodland excursion, but of lesser duration.

2.6.5 Archaeological implications

2.6.5.1 Prehistoric land disturbance

Prehistoric land disturbance in the Northeastern United States and Ontario has been previously recognized for the Late Woodland period, for which Iroquoian village sites, such as Crawford Lake (Ontario) are exemplary (Ekdahl et al. 2004; Turton and McAndrews 2006; McAndrews and Turton 2010). Agriculture and landscape modification for semi-permanent villages was not a prominent feature of Middle Woodland period sites in Ontario, and despite robust evidence for mound construction in the geological record of other Hopewell-influenced sites (see Bernardini (2004), O’Neal et al. (2005), Stinchcomb et al. (2011), O’Neal (2012), Herrmann et al. (2014), Hugenholtz et al. (2014), Munoz et al. (2014), and Magnani and Schroder (2015)), no such evidence has yet been recovered in a lacustrine sediment core from pre-agricultural Ontario.

The Middle Woodland sediment excursion, lasting 2250–1300 cal BP, closely aligns to estimates of site usage from Johnston (1968) (Fig. 2.15). The first excursion peak (2200 cal BP), and transition to B5 biofacies suggests rapid change within the ecosystem, involving higher terrigenous input, and available nutrients in the lake, reminiscent of the geochemical record at the time of Hastings. Detrital input slowed only slightly from 1900–1700 cal BP, before a second, larger excursion with sedimentation rates comparable to the post-dam lake (1.46 mm yr^{-1}). This second excursion, and increase in nutrient-loving thecamoebians could reflect intensification of site usage approaching the middle to end of the Point Peninsula occupations, whereas the first may only have been a response to seasonal occupation and procurement of shellfish resources.

The shell midden at Serpent Mounds was dated 2020 ± 150 BP (1987 cal BP) by Johnston (1968), which he acknowledged may predate mound construction, estimated between 1756–1557 cal BP using recalibrated dates from Mound E. If there was an offset between shellfish harvesting and the construction of the mounds, then the second excursion (ca. 1700–1300 cal BP) may be produced by the construction of Serpent Mounds (Fig. 2.15). Although difficult to discern construction episodes from this signal, as were hypothesized by Johnston (1968), the duration of the signal suggests multiple episodes of construction.

This signal was not isolated to SRPM-02, and is detected in the GOM PCA across all cores (Fig. 2.11B) with radiocarbon dates from SRPM-10 and SRPM-11 confirming the signal to be of Point-Peninsula age. The strength of this signal is generally weaker moving away from Serpent Mounds, and is only detected as a small interval of $D3_G$ in SRPM-07, hundreds of metres from the mounds. The paleogeographic reconstruction of Figure 2.14C shows terrestrial connectivity between Serpent Mounds and the other mound sites on East Sugar Island and Harris Island, and the reported shell midden on Prison Island (Richardson 1968). With abundant wild rice and shellfish resources, it is plausible that the paleogeography of the area would be conducive to gatherings at multiple sites, for seasonal resource exploitation or ritual purposes. Population estimates from Middle Woodland Rice Lake are unclear, and biased toward excavations at one site (Dillane 2010). Smaller estimates from Wilson (1993) suggest small bands between 25–50 individuals, while Spence et al. (1984) suggest much larger groups between 100–200. These regional estimates originate from two different qualitative interpretations of a single mound (Mound "C") at the Cameron's Point Site (^{14}C dated to 1891–1697 cal BP), at the mouth of the Otonabee River (Fig. 1.5) (Dillane 2010). The supposition that a single burial sequence is adequately representative for regional population estimates in either model are reasonably suspicious. These estimates did not consider large regional gatherings, unrelated to mound construction and burials, which may have produced

intense episodes of terrestrial erosion, and substrate turbation from shellfish gathering.

Using large datasets to demonstrate the presence of prehistoric anthropogenic landscape change has been performed in Ontario and elsewhere with pollen data (Munoz et al. 2010; Munoz and Gajewski 2010). It was discovered that large scale land modification for agriculture relied on swidden farming techniques. An investigation by Stinchcomb et al. (2011) revealed substantial changes to the sediment record within the Delaware River Valley, related to deforestation and farming which took place between 1100–1600 CE (850–350 BP). Their findings demonstrate relatively small numbers of individuals can have disproportionately large impacts on hydrological systems. Munoz et al. (2014) also demonstrate anthropogenic influence within the pollen record of a lake sediment core near the Cahokia mounds site (Illinois, USA) starting at 1500 BP. Dates as early as ca. 3000 BP have been suggested for the domestication of non-maize seedstock in the midwest Hopewell region, which may likely have been traded as high-value items elsewhere (Mueller 2018). Despite an evident trade link with the south, large-scale agriculture was apparently not adopted by the Point Peninsula culture, at least, not as far as the Trent Valley excavations have shown (Ellis and Ferris 1990). Yet, stable isotope evidence obtained from skeletons at Serpent Mounds suggest some dietary component to be from maize (Katzenberg 2006). It is unclear or if it is the product of domestic growth, possibly at a much smaller scale than observed in the Late Woodland (Munoz and Gajewski 2010).

2.6.5.2 Climate and geomorphic factors?

We interpret the increase in detrital sediment flux to Rice Lake during the Point Peninsula occupation to be a land disturbance episode of anthropogenic origin, after consideration of other possible factors, including changes in climate and autogenic geomorphic processes (e.g. Foreman and Straub (2017)). In previous studies paleoclimatic shifts

have been identified based on pollen records and plant macrofossil data (Yu and McAndrews 1994; Yu et al. 1996), the climate experienced by Rice Lake was cool and moist, with additional data from nearby McIntyre Lagoon suggesting the lake was shallow, with abundant stands of wild rice (McAndrews 1984).

Available paleoclimate reconstructions for southern Ontario indicate that precipitation levels during the Point Peninsula phase were near present mean annual values (Edwards and Fritz 1986; Edwards and Fritz 1988; Edwards and McAndrews 1989; Edwards et al. 1996; McCarthy and McAndrews 2012; Lewis 2016). However, Ontario's climate for the past 4000 years remains difficult to interpret, owing to the distribution of study sites, and in some cases insufficient data, forcing large interpolations (Edwards and Fritz 1986; Edwards and McAndrews 1989). Figure 1 in Edwards et al. (1996) uses a composite dataset of inferred relative humidity and $\delta^{18}\text{O}$ values from several other studies (Edwards and Fritz 1986; Edwards and Fritz 1988; Edwards and McAndrews 1989; Duthie et al. 1996), but lacks the resolution to comment on Middle Woodland climate, as a 500-year moving average was applied.

Although comprehensive for the mid-Holocene hiatus, many of these studies, lack the fine age control required for comparison to the μ -XRF data of this study. Edwards and Fritz (1988) and Duthie et al. (1996) provide some measurements through this period at Little Lake, and in Hamilton Harbour (Ontario), respectively. The results show a general depletion in ^{18}O , indicating slightly more precipitation, but do not record any anomalies in precipitation which could explain the increased detrital sediment flux during the Point Peninsula occupation. The synthesis of precipitation values from Figure 12 in Lewis (2016), uses both the mean stable isotope record from Edwards et al. (1996), and transfer function-derived precipitation values from McCarthy and McAndrews (2012). The latter study compiled several transfer function results, finding no anomalous precipitation spikes during the Middle Woodland, and reporting mean annual precipitation

values lower than present for most sampled lakes.

Recent paleoclimate investigations in the northeastern United States, although not perfectly analogous to southern Ontario, provide a more complete record of change in recent millenia. A comprehensive climate investigation by Marlon et al. (2017) provides a complete multi-proxy overview of the past 3000 years (see Figure 7 in Marlon et al. (2017)). A key finding of this synthesis was a prolonged drought from 1650–1150 years BP, intensifying from 1400–1200 cal BP. If this drought phase extended to Serpent Mounds, precipitation-driven erosion may not have been a factor in the sediment signal. Further investigation of paleoclimate during the Middle Woodland is required, with greater regional specificity to Rice Lake, before a definitive conclusion can be made regarding the origin of the Middle Woodland signal.

Autogenic processes operating within the basin on the order of days to millenia can produce spurious sediment signals, which may overprint human activity at equivalent timescales to the Serpent Mounds occupation. These signals are largely stochastic, and are only overcome when a signal of interest is of longer duration, or greater amplitude (Foreman and Straub 2017). In some cases, even genuine event signals may be distorted through overprinting, or reworking (Romans et al. 2016). At Rice Lake, discharge from the Indian River, change in slope at Roach Point, and shoreline processes are examples of autogenic influences. Shoreline processes, such as wave action, operate on daily timescales, but also include annual events from ice rafting when the lake surface freezes, making shoreline processes a mixed signal with varying seasonal intensity from two primary forces. The timescales for hillslope denudation can naturally occur on the order of $>5 \text{ mm yr}^{-1}$ in steep topographies (Hovius et al. 1997), but surface movement down-slope can be between $6\text{--}30 \text{ mm yr}^{-1}$ in low to moderate-relief tills (Saunders and Young 1983). The latter values were documented in polar climates, however, and do not account for impedance from vegetation, or, in the case of Serpent Mounds, any alterations

which arise from human activity (O'Neal et al. 2005). The closest fluvial system, with a marshy delta lobe (Fig. 2.2) is the Indian river, which may produce a cyclic signal at a similar frequency to its episodes of flooding, and greater detrital loading (Bryant et al. 1995; Enfield et al. 2001; Macklin and Lewin 2003). However, after careful inspection of the sonar data of this study and of Sonnenburg et al. (2013), clear evidence of thalwegs tracking into the study area from the Indian river were not located. Several sonar lines showed evidence of spurious depressions in the lakebed, but only one example of a possible inundated outlet channel adjacent Harris Island (Fig. 2.2). Any anomalies in the sonar profile which resemble fluvial features would be difficult to distinguish in a temporal domain. The sediment profile of Rice Lake exhibits numerous examples of old bathymetric features (EH-1 and EH-2; Sonnenburg et al. (2013)) in-filled by younger sediments. Ancient channel features may retain some semblance of a sinuous form on the lakebed, though no channels may be active at the time younger sediments are deposited.

Figure 2.15 demonstrates some form of cyclic terrigenous element signal in Unit 3 of SRPM-02, likely propagated by allogenic or autogenic processes, or a combination of the two. Clear deviation from this signal is observed both during the Serpent Mounds phase, and the Hastings dam construction, at a high amplitude and much lower frequency, that exceeds the Unit 4 transgressive deposit in terms of ecosystem perturbation.

2.6.5.3 Non-invasive archaeology

Non-invasive geophysical and remote sensing techniques are being employed increasingly in archaeology as tools for locating sites, for pre-excavation planning and to investigate sites of high cultural value where disturbance must be minimized (Kvamme 2003; Bates et al. 2008; Forte and Pipan 2008; Hesse 2010; Burks 2014; Herrmann et

al. 2014). Recent studies of Adena and Hopewell mounds in the midwestern US have employed LiDAR and photogrammetric methods to construct high-resolution digital terrain models (DTM), which enable enhanced morphometric analysis of mound structures (Magnani and Schroder 2015). Geophysical methods (e.g. ground-penetrating radar, resistivity surveys) have also provided new details of the internal structure of burial mounds, yielding important insights into mound construction (Burks 2014).

Micropaleontological analysis, including thecamoebians, desmids, dinoflagellates, diatoms, pollen, and even cultivar pathogens have been used in Late Woodland contexts to detect the influence of large indigenous populations in Ontario (Burden et al. 1986; Scharf 2010; McCarthy and Krueger 2013; Volik et al. 2016). However, these are less useful for investigation of earlier archaeological periods, when widespread horticulture was not present in Ontario, and elsewhere. In these cases, the use of high-resolution μ -XRF core scan data can provide the highest available spatial and chronological resolution for paleolimnological datasets, and is able to discern potential land disturbance episodes in the absence of agriculture.

In this paper, we have demonstrated the application of μ -XRF elemental analysis for detecting prehistoric land disturbance in lake sediment. This approach has potential broader applications for detecting a range of environmental signals stemming from prehistoric land disturbance episodes (e.g. onset of agriculture, land clearance, village settlement, midden accumulation). The success of using μ -XRF core scanning depends on the availability of a continuous sediment archive (e.g. lake basin, wetland) proximal to the archaeological site. Serpent Mounds was an ideal candidate for this study, as the high-relief drumlinized topography at the site likely enhanced overland transport and delivery of sediments to the lake margin. Any site able to influence the local sediment record can be detected using the methodology of this study, but with varying levels of

clarity dependent on the length and frequency of occupation. Serpent Mounds is believed to have been occupied from spring to autumn, annually, with large gatherings involving the interment of the dead, which, after many centuries, is more liable to leave a geochemical imprint (Johnston 1968; Dillane 2010).

2.7 Conclusions

This study has resolved a prehistoric land disturbance episode at Serpent Mounds discerned by μ -XRF-CS as an increase in terrigenous elements for a period coinciding with the start (ca. 2200 BP) and end (ca. 1300 BP) of the Serpent Mounds occupation. The magnitude of terrigenous input from the event is comparable to that of the Hastings dam construction, but with greater duration. This signal coincides with a shift in thecamoebian biofacies to a eutrophic assemblage, responding to the sudden increase in eroded soil nutrients. The paleogeographic reconstructions indicate substantial wild rice habitat adjacent to Serpent Mounds and other sites, in what was a shallow lake environment with abundant peripheral wetlands. The resource availability, and terrestrial connectivity between sites owing to lower water levels (~183 m asl) would have been favourable for the establishment of large encampments, and the coordination of burial mound construction. Factors for land disturbance go beyond mound construction, as the dense cluster of Point Peninsula sites in the study area were used for procurement of shellfish and wild rice gathering.

The findings of this study demonstrate the utility of μ -XRF-CS and micropaleontology for investigating sensitive archaeological sites. The paleogeographic reconstruction adds further clarity to the μ -XRF and thecamoebian results, and provides an areal estimate of available wild rice stands, which may have given the impetus for monumental earthwork construction (Dillane 2010). This is the first study of a burial mound in North

America to recover a geochemical signal of pre-agricultural land clearance using μ -XRF-CS, and do so in a non-destructive manner; which is essential for the continued study of sensitive sites like Serpent Mounds.

Chapter 3

Summary

3.1 Conclusions

This thesis has demonstrated the application of μ -XRF-CS and micropaleontological analysis for non-invasive investigation of a sensitive archaeological site. The μ -XRF analysis has identified a terrigenous element excursion, that is synchronous with the Point Peninsula occupation of the Serpent Mounds site, as estimated by previous radiocarbon dating from the site (Johnston 1968) (Table 2.1). This objective was achieved through the multivariate analysis of a large volume of μ -XRF-CS data, corroborated by thecamoebian analysis, providing geochemical and micropaleontological evidence of environmental shifts at Serpent Mounds since 6600 BP. A detailed bathymetric survey was employed to construct the site paleogeography and assisted with selection of coring sites, and made possible the recovery of a nearly continuous Late Holocene sediment record. Sediment back-stripping and paleobathymetric maps allowed reconstruction of the Middle Woodland shoreline and lake water levels, providing estimates of viable wild rice growth habitat at the Serpent Mounds site. Furthermore, the water level curve of Sonnenburg et al. (2013) was revised and improved with a suite of new AMS radiocarbon dates, which demonstrate water levels were about 1 m lower than previous estimates during mid-Holocene (EH-2) shoreline transgression. The increased influx of

clastic sediment indicated by an excursions in minerogenic elements (principally Ti, Fe, K, Si, Zr) at ca. 2200–1300 cal BP is interpreted as evidence of mound building and site occupation by prehistoric indigenous peoples, owing to several lines of evidence:

1. The radiocarbon chronology of SRPM-02 indicates two pulses in clastic sedimentation over an interval of about 750 years, which coincides with the established dates for Middle Woodland occupation of Serpent Mounds, and other mound sites in the immediate area. The excursion begins at the arrival time of Point Peninsula peoples at Rice Lake (ca. 1820–2153 cal BP) and ends with the termination of activity at Serpent Mounds (ca. 1290 cal BP).
2. The thecamoebian biofacies indicate a rapid shift toward a more nutrient-rich, lacustrine environment, dominated by *D. oblonga* and *C. tricuspis*, with declining marsh species. The decline in marsh species may indicate continued rise in water levels and perhaps human environmental disturbance as utilization of wetland resources and shellfish harvesting intensified. High abundance of *D. urens*, which have been observed elsewhere to tolerate turbid environments and high sedimentation rates (Patterson et al. 2002), occurs during the second sediment excursion, which correlates with radiocarbon ages from within Mound E (East: 1756 cal BP, South: 1557 cal BP). The abundance of eutrophication-indicative thecamoebian taxa is second only to the post-dam phase, at a time before large-scale land clearance and agriculture.
3. The large increase in sedimentation rates (from 0.57 to approximately 1.5 mm yr⁻¹) at the time of Serpent Mounds construction indicates heightened erosion, and is comparable to increases in sedimentation rate stemming from indigenous agriculture elsewhere (Stinchcomb et al. 2011). Sedimentation rates return to lower values (0.9 mm yr⁻¹) a few hundred years afterwards (ca. 1000 cal BP).

4. The application of multivariate analysis to μ -XRF-CS data demonstrates that the event can be recognized as a distinctive chemofacies across multiple cores, with a sediment signal strength inversely-proportional to distance from Roach Point. Additional radiocarbon dates from SRPM-10 and SRPM-11 yielded similar ages for the sedimentation event observed in those cores.
5. The magnitude of the land disturbance event is comparable to the increase in sedimentation rate produced by construction of the Hastings Dam (1838 CE). The longer duration of the Middle Woodland signal (ca. 750 years) can be attributed not only to mound construction, but to the numerous other activities (shellfish bed usage, wild rice harvesting, shoreline habitation) that formed the fabric of everyday life for the Point Peninsula people.

The long sediment record obtained in core SRPM02 also provided new insights into the environmental changes associated with the Hypsithermal dry climate phase at Rice Lake. The continuous record from 6541 cal BP in Unit 6 provides a geochemical record of lake conditions during the terminal Hypsithermal. The silty Unit 6 gyttja was deposited when very nearby areas of Rice Lake, like neighboring McIntyre Lagoon, were depositing marl (Fig. 2B – RIL10 in Sonnenburg et al. (2013)). A steady and equal rise is observed in Si, Ti, K, and Fe profiles within Unit 5 of SRPM02 (Fig. 2.6), with concurrent marl production, which shows organic inclusion frequency increasing up-core in the optical image. These trends are observed during a slight increase in sedimentation rate (0.47 to 0.51 mm yr⁻¹) between 5050 and 4350 cal BP, after which point, a sharp decrease in Ca marks the end of marl deposition. The geochemical record during this time agrees with the hypotheses of several authors, and records a gradual rise in water level, thought to be from increasing precipitation, linked to a broader deciduous shift in the upland forest assemblage of Rice Lake (McAndrews 1984; Yu and McAndrews 1994).

This thesis provides the most complete, and detailed environmental reconstruction

of Rice Lake during the Middle Woodland Period. The paleoenvironmental data (e.g. water levels, shore line position) are key to understanding the archaeological context and relationship between mound sites and also provide some insights as to the extent of potential wild rice resources that were a staple for prehistoric indigenous peoples. Although the population during the Middle Woodland is not known, it has been estimated hundreds of people gathered seasonally at the mounds of Rice Lake and, the major river drainages (Dillane 2010). The population size and its concentration with the lake environs around MacGregor Bay may explain in part why the land disturbance signal is comparable to later land-clearance associated with European colonization.

3.2 Future Work and Archaeological Implications

The results of this study leave two areas of critical importance to be explored in future investigations at Rice Lake. The first concerns Middle Woodland period climate variability, particularly changes in precipitation effecting runoff. Multiple previous studies at Rice Lake and in the Lake Ontario basin have identified several climatic shifts (Sonnenburg et al. 2013), but most paleolimnological research has emphasized reconstruction of water levels and vegetation since deglaciation (Yu and McAndrews 1994; Anderson and Lewis 2012; Lewis 2016). Numerous studies have documented climate conditions during the Holocene Hypsithermal (Edwards and Fritz 1986; Fritz et al. 1987; Edwards and Fritz 1988; Edwards et al. 1996; McCarthy and McAndrews 2012) but there is a relative dearth on the subsequent Neoglacial, which is generally accepted to have been a wetter, cooler phase. Therefore it is difficult to disentangle the Middle Woodland detrital sediment excursion recorded at Rice Lake, from enhanced soil erosion resulting from a wetter Neoglacial climate.

While Neoglacial paleoclimate data for southern Ontario is scarce, several recent

studies in the northeastern USA have employed pollen and other proxies to reconstruct Neoglacial climate change. Recently, Marlon et al. (2017) compiled regional proxy climate data for the past 3000 years in the northeastern United States, noting a period of drought between 1400–1200 cal BP, and an even longer dry period spanning 1650–1150 cal BP. The implications are significant to this project, as a dry climate with reduced rainfall suggests the sediment signal is entirely anthropogenic in origin. A paleoclimate assessment of the late Holocene at Rice Lake should be undertaken to assess the validity of the interpreted land disturbance as archaeological in origin.

The second area of future work is the incorporation of μ -XRF-CS within the framework of studies investigating the impact of humans on the landscape of pre-colonial North America. Several studies have provided strong evidence for significant changes in the forests of southern Ontario after the wide adoption of maize agriculture around 1000 CE (Smith 1997; Ekdahl et al. 2004; Turton and McAndrews 2006; McAndrews and Turton 2010; Munoz et al. 2010; Munoz and Gajewski 2010). The methods employed in this thesis could significantly improve the chronology and environmental history of landscape impacts, owing to the high maximum resolution (200 μ m) of μ -XRF-CS. Studies investigating the Late Woodland period (~1000–1600 CE) often resort to using pollen datasets, which lack both the spatial and chronological resolution provided by μ -XRF-CS.

The methods used here can also compliment the large body of work conducted on earthwork structures at Hopewell sites in Ohio and Illinois. Several geoarchaeological investigations have employed non-destructive techniques such as LiDAR (O'Neal et al. 2005; Romain and Burks 2008; O'Neal 2012), photogrammetry (Magnani and Schroder 2015), ground penetrating radar (Herrmann et al. 2014), magnetic survey (Burks 2014) and core surveys (Stinchcomb et al. 2011; Munoz et al. 2014) to model the landscape

impact of mound construction, degradation, and broader landscape changes in the Mid-western United States. O'Neal et al. (2005) modelled the rates of erosion on Hopewellian-aged earthworks in Ohio (U.S.A.), suggesting the mounds rapidly degrade if not constantly maintained through the addition of built layers. Their models suggest an 1800-year window for degradation of mounds, from structural apex to present form, in a similar climate to that of Ontario. Topographic diffusivity in their model was found to be $5.0 \times 10^{-4} \text{m}^2 \text{yr}^{-1}$. O'Neal et al. (2005) cite a common problem with understanding the timing of earthwork construction, lies in the usual process of investigation through excavation, which rarely accounts for eroded material, which emphasizes the importance of understanding erosion in all aspects, from the mound to catchment. Combining μ -XRF-CS methods with conventional archaeological methods could provide more complete estimates of runoff contribution from mound construction in lakes, and more importantly, how long a mound will be detectable in the sediment record following disuse of a site. Detection of land use at Ohio and Illinois mound sites is somewhat easier, owing to the earlier adoption of agriculture there and greater scale of land clearance and disturbance when compared to southern Ontario (Stinchcomb et al. 2011).

At pre-agricultural mound-building sites such as Serpent Mounds, the detection of prehistoric land use changes can be a challenge, as the geochemical changes in lake sediment are likely to be subtle. The use of environmental proxies, like thecamoebians, further helps to detect changes in lake trophic state associated with land disturbance events, but μ -XRF-CS is a far more useful tool for resolving relatively short occupations with unparalleled chronostratigraphic sampling resolution. The multivariate analysis methods outlined in Chapter 2 clearly highlights the utility and flexibility of μ -XRF-CS data for discerning land disturbance episodes. This thesis is significant, as it is the first to provide evidence of pre-agricultural, pre-colonial land disturbance related to earthwork construction and site occupation in North America. This objective was furthermore achieved non-destructively, respecting the sacred importance of Serpent Mounds

to First Nations.

Appendix A

Chapter 1 Supplement

Table A1.1: Summary of basic and advanced functions included in Py-Trax

Pytrax Basic Functions
Automatic alignment and plotting of multiple core sections
Plotting cores to custom depth datum, automatic recalculation of data from desired start depth
Automatic image alignment, preserving aspect ratio through Lanczos interpolation when restricting plot area to one area of the core
Boolean operation used to remove erroneous data or unwanted data sections
Any number of element profiles (or other Itrax parameters) may be plotted
Data may be decimated to a desired interval during plotting
Moving average may be superimposed over respective element, to desired window
Depth interval may be selected by desired minimum and maximum depth of core
PyTrax Data Operations
Normalize data to: standard deviation, incoherent or coherent scatter, sum of scattering values
Additional options for log transformation and z-score scaling
Multiple levels of normalization and transformation (eg. normalizing to a scatter value, then log transform)
Custom profiles of elements based on sum, difference, product, or quotient, can be combined with normalization features
PCA of desired elements, with plotting available for individual principal components
Second comparative PCA may be performed and plotted for specific sections of the core
Cluster analysis of principal components for visualization of chemofacies based on reduced data
RGB spectra from image data can be calculated and plotted
PCA of RGB data may be performed for improved noise reduction
Additional Visualization Tools
Plotting with secondary y-axis to display radiocarbon ages in a linear format, respecting the changes in sedimentation rate with the plotting interval of minor ticks
Plotting data by age (can accept age models of any variety from CLAM (Blaauw 2010) or BACON (Blaauw and Christen 2011))
Selective log-scaling of data for improved visualization of elemental profiles with large magnitude variance
Clipping of data according to desired buffer value around the moving average of element profiles
Insertion of user-defined number of subplots if additional plotting of data outside the scope of PyTrax is desired

Appendix B

Chapter 2 Supplement

Table A2.1: Table of PCA values and variance ratio for optical images of all cores (excluding SRPM03)

Principal Component	Red	Green	Blue	Variance Ratio	Red	Green	Blue	Variance Ratio
SRPM01				SRPM08				
PC1	0.58	0.58	0.58	9.89×10^{-1}	0.58	0.58	0.58	9.88×10^{-1}
PC2	-0.70	-0.02	0.72	1.07×10^{-2}	-0.69	-0.03	0.72	1.19×10^{-2}
PC3	0.42	-0.81	0.40	3.07×10^{-4}	0.44	-0.81	0.38	1.54×10^{-4}
SRPM02				SRPM09				
PC1	0.58	0.58	0.58	9.86×10^{-1}	0.57	0.58	0.57	9.80×10^{-1}
PC2	-0.66	-0.08	0.75	1.42×10^{-2}	-0.71	-1.00×10^{-3}	0.71	2.04×10^{-2}
PC3	0.48	-0.81	0.34	1.66×10^{-4}	0.41	-0.81	0.41	4.46×10^{-5}
SRPM05				SRPM10				
PC1	0.58	0.58	0.58	9.89×10^{-1}	0.58	0.58	0.58	9.91×10^{-1}
PC2	-0.79	0.21	0.57	1.09×10^{-2}	-0.72	0.02	0.69	9.15×10^{-3}
PC3	0.21	-0.79	0.58	1.34×10^{-4}	0.39	-0.81	0.43	3.27×10^{-5}
SRPM06				SRPM11				
PC1	-0.58	-0.58	-0.57	9.80×10^{-1}	0.58	0.58	0.58	9.88×10^{-1}
PC2	0.65	0.10	-0.75	2.04×10^{-2}	-0.75	0.08	0.66	1.14×10^{-2}
PC3	0.41	-0.81	0.41	4.46×10^{-5}	0.34	-0.81	0.48	1.55×10^{-4}
SRPM07				SRPM12				
PC1	0.58	0.58	0.58	9.94×10^{-1}	0.58	0.58	0.58	9.94×10^{-1}
PC2	-0.74	0.06	0.68	6.50×10^{-3}	-0.68	-0.05	0.73	5.72×10^{-3}
PC3	-0.36	0.81	-0.46	4.79×10^{-5}	-0.45	0.81	-0.37	2.03×10^{-4}

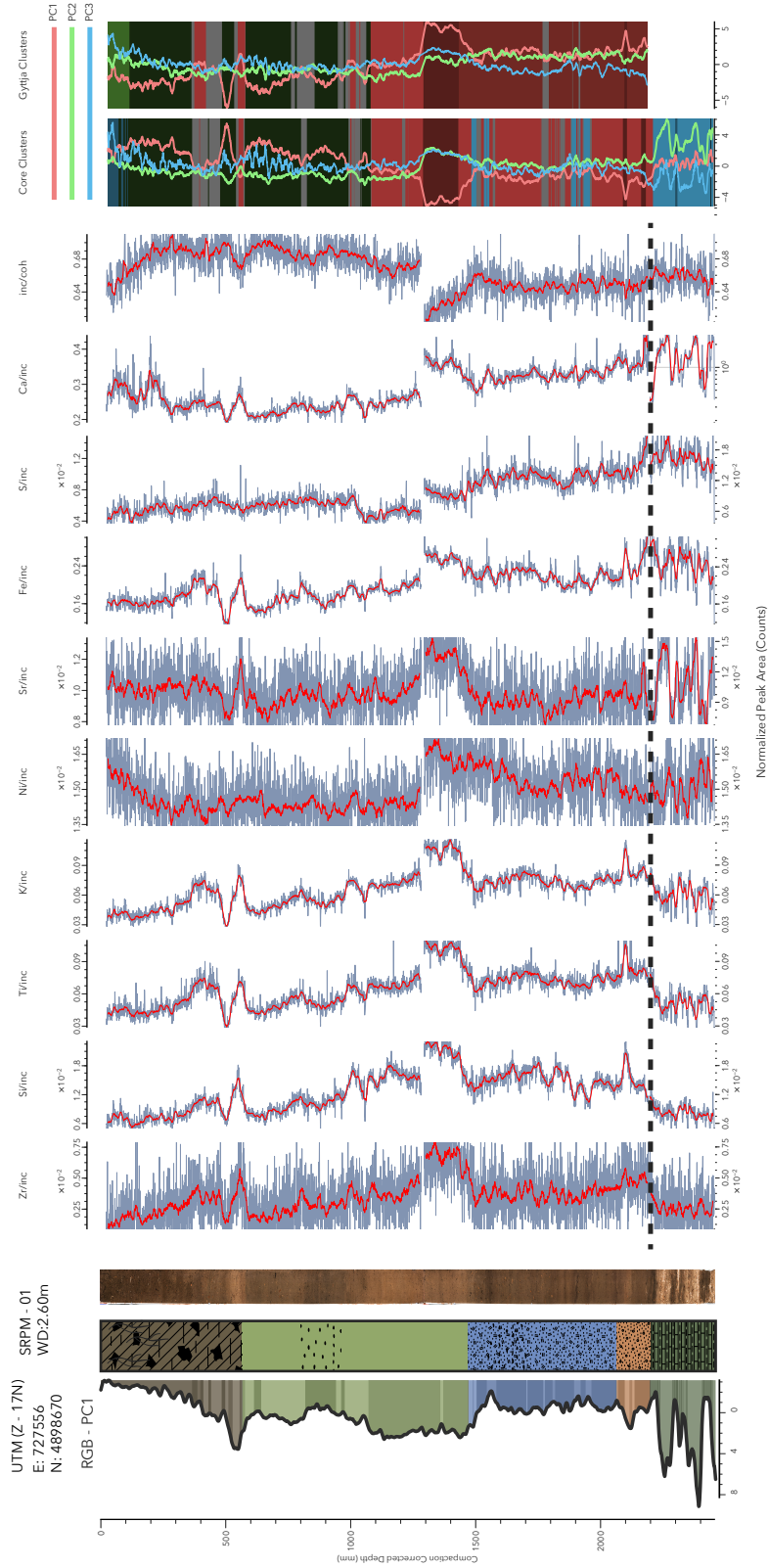


Figure A2.1: μ -XRF profile and RGB scans for SRPM-01 including FCM and GOM chemofacies and PCA results. XRF peak areas are normalized to incoherent scattering. Red line indicates change in XRF scales - average of normalized count values. Dashed line indicates change in XRF scales - scales for measurements above and below the dashed line are displayed at the top, and bottom of the plot, respectively. Lithofacies interpretation also included. RGB image brightness (PC1) plotted in standard deviations.

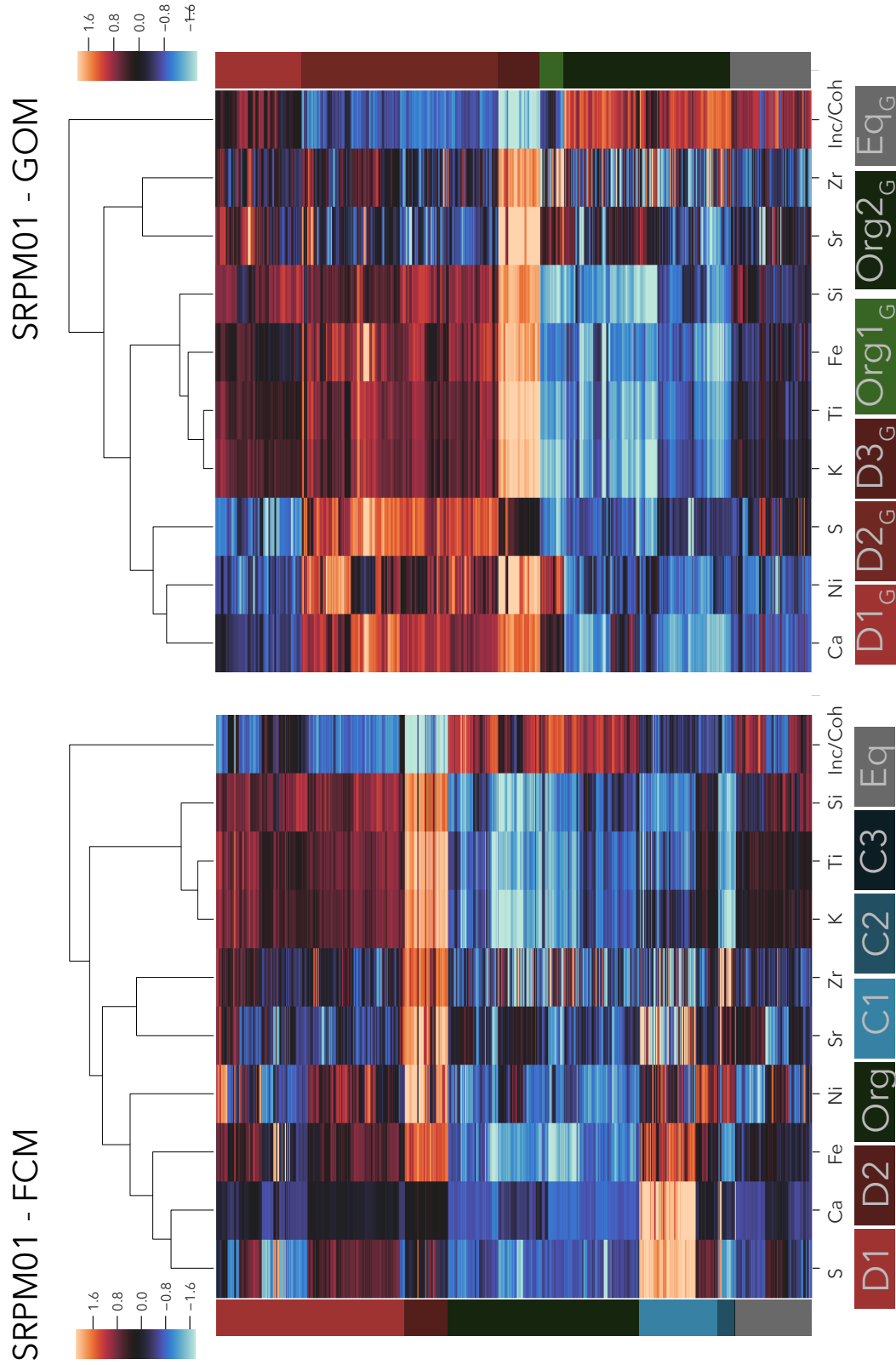


Figure A2.2: Heatmaps and R-mode dendrograms showing element associations within-core, plotted with respect to chemofacies (Data in non-stratigraphic order). Element values are standardized, and in units of standard deviations. Results are shown for both the FCM and GOM.

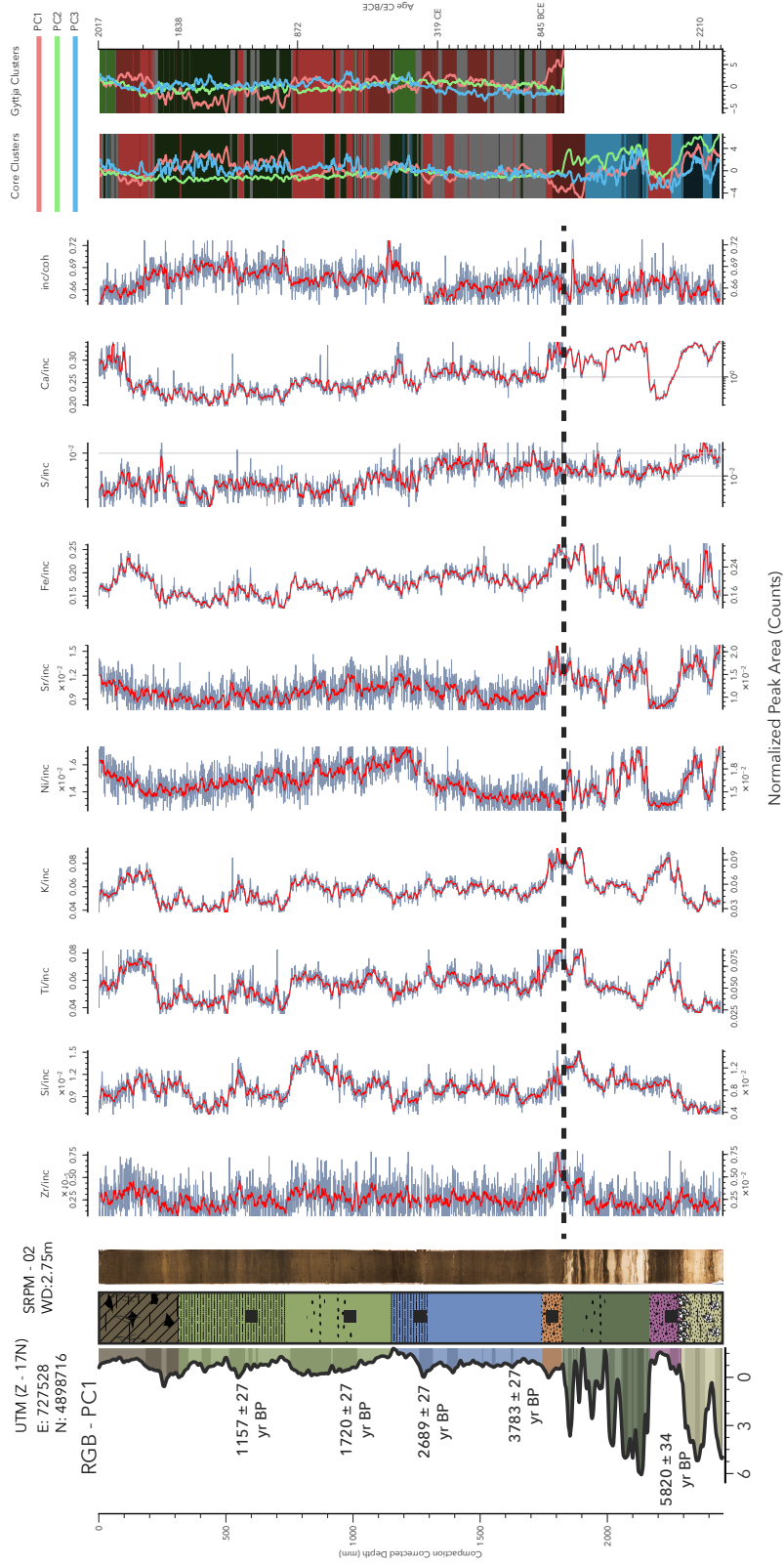


Figure A2.3: μ -XRF profile and RGB core scans for SRPM-02, including FCM and GOM chemofacies and PCA results. XRF peak areas are normalized to incoherent scattering. Red line overlapping element traces is a 1 cm moving average of normalized count values. Dashed line indicates change in XRF scales - scales for measurements above and below the dashed line are displayed at the top, and bottom of the plot, respectively. Lithofacies interpretation also included. RGB image brightness (PC1) plotted in standard deviations.

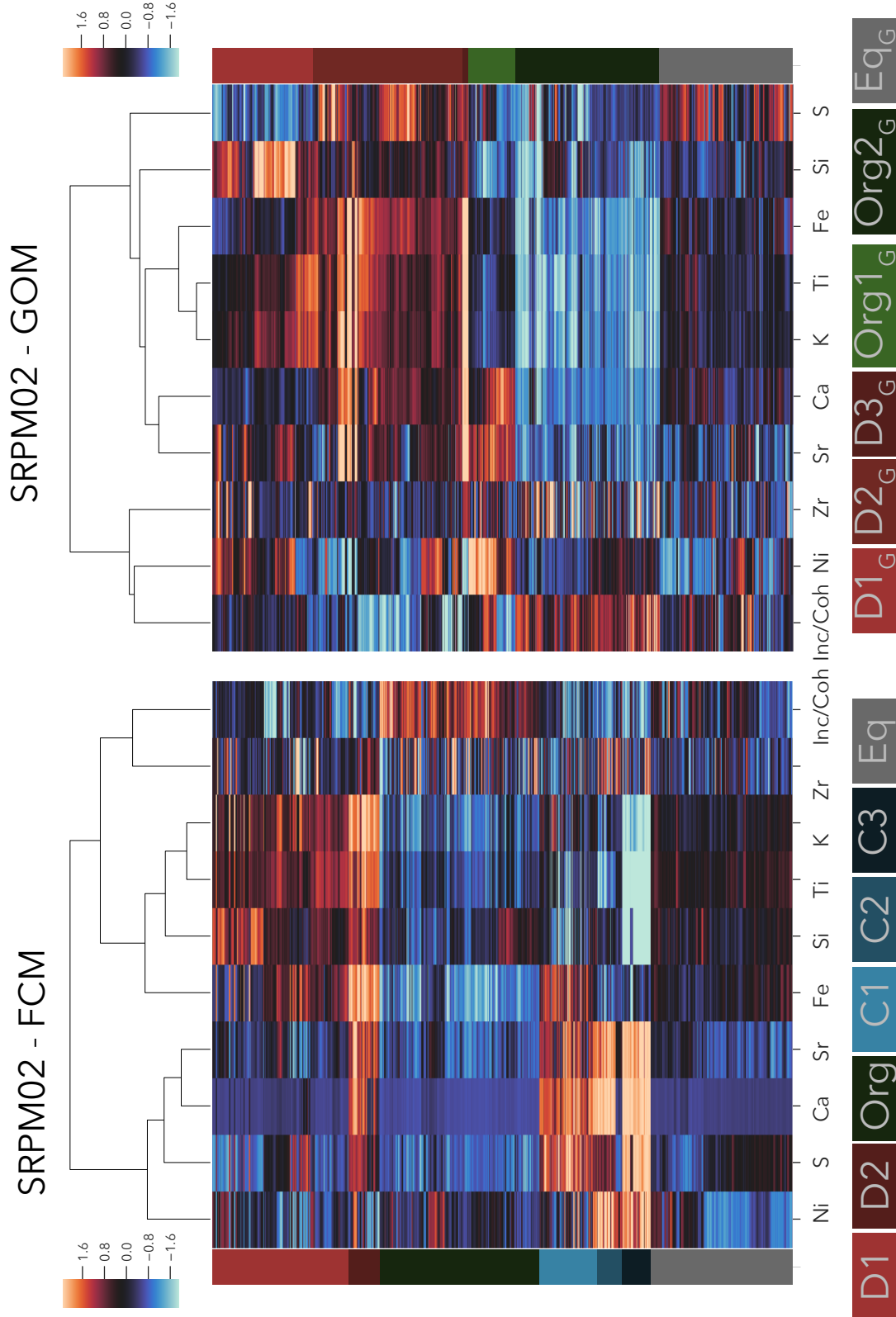


Figure A2.4: Heatmaps and R-mode dendrograms showing element associations within-core, plotted with respect to chemofacies (Data in non-stratigraphic order). Element values are standardized, and in units of standard deviations. Results are shown for both the FCM and GOM.

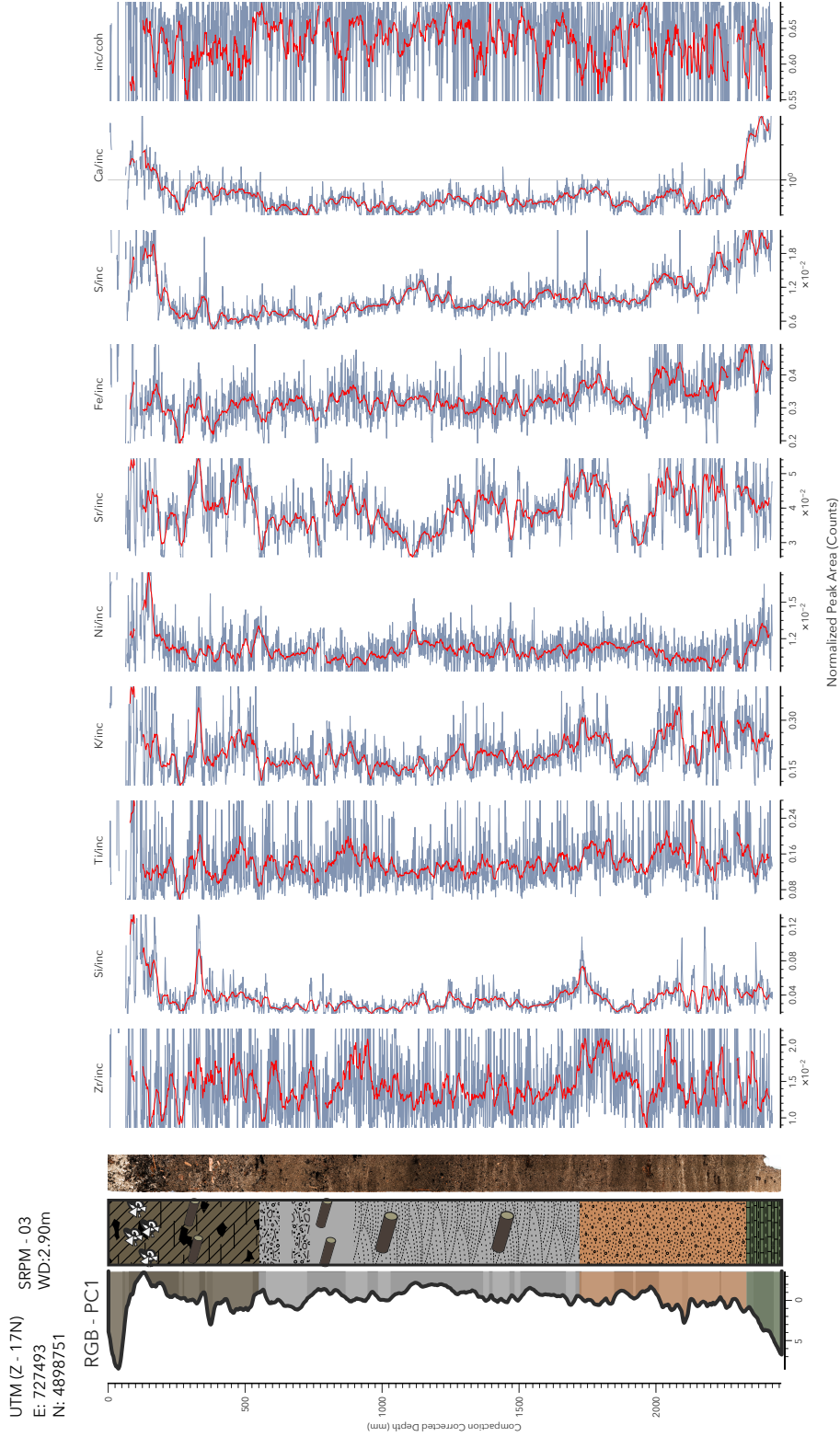


Figure A2.5: μ -XRF profile and RGB core scans for SRPM-03. XRF peak areas are normalized to incoherent scattering. Red line overlapping element traces is a 1 cm moving average of normalized count values. Dashed line indicates change in XRF scales - scales for measurements above and below the dashed line are displayed at the top, and bottom of the plot, respectively. Lithofacies interpretation also included. RGB image brightness (PC1) plotted in standard deviations.

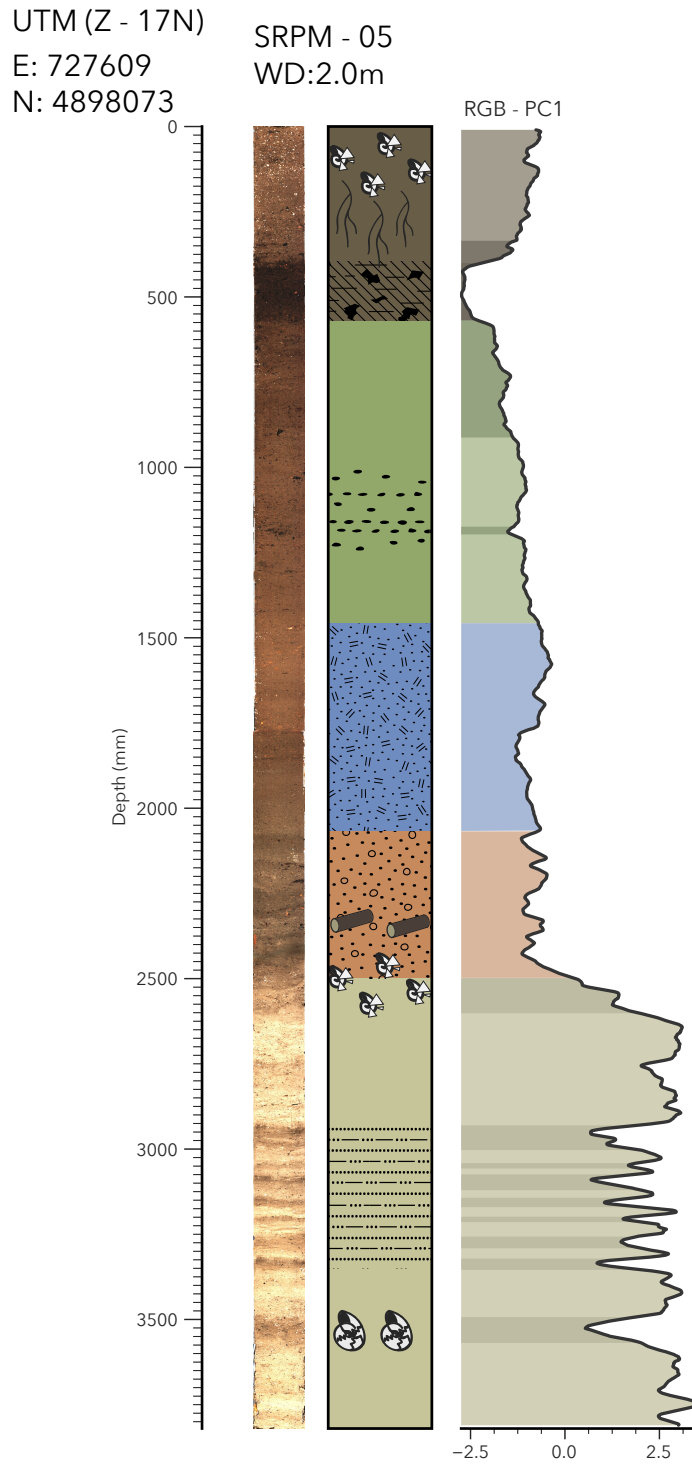


Figure A2.6: RGB core scan for SRPM-05. RGB image brightness (PC1) plotted in standard deviations. Lithofacies interpretation also included.

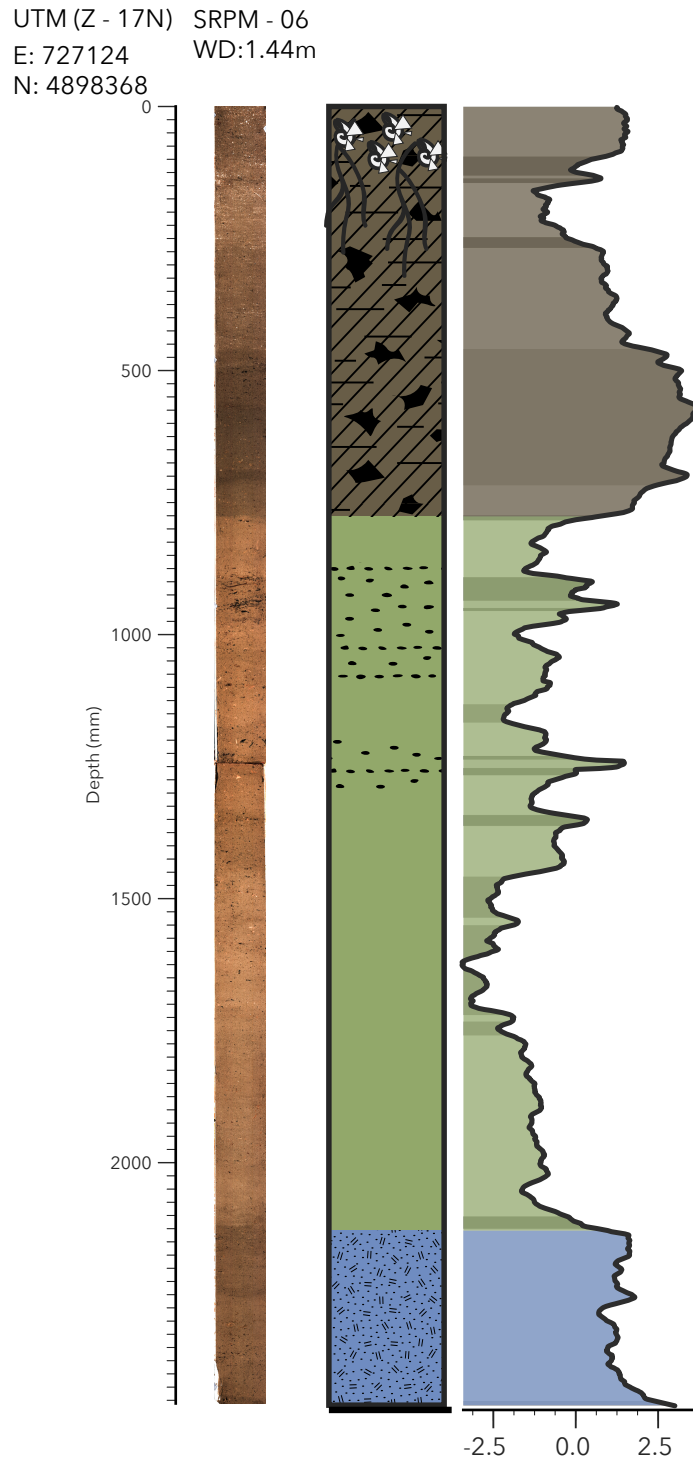


Figure A2.7: RGB core scan for SRPM-06. RGB image brightness (PC1) plotted in standard deviations. Lithofacies interpretation also included.

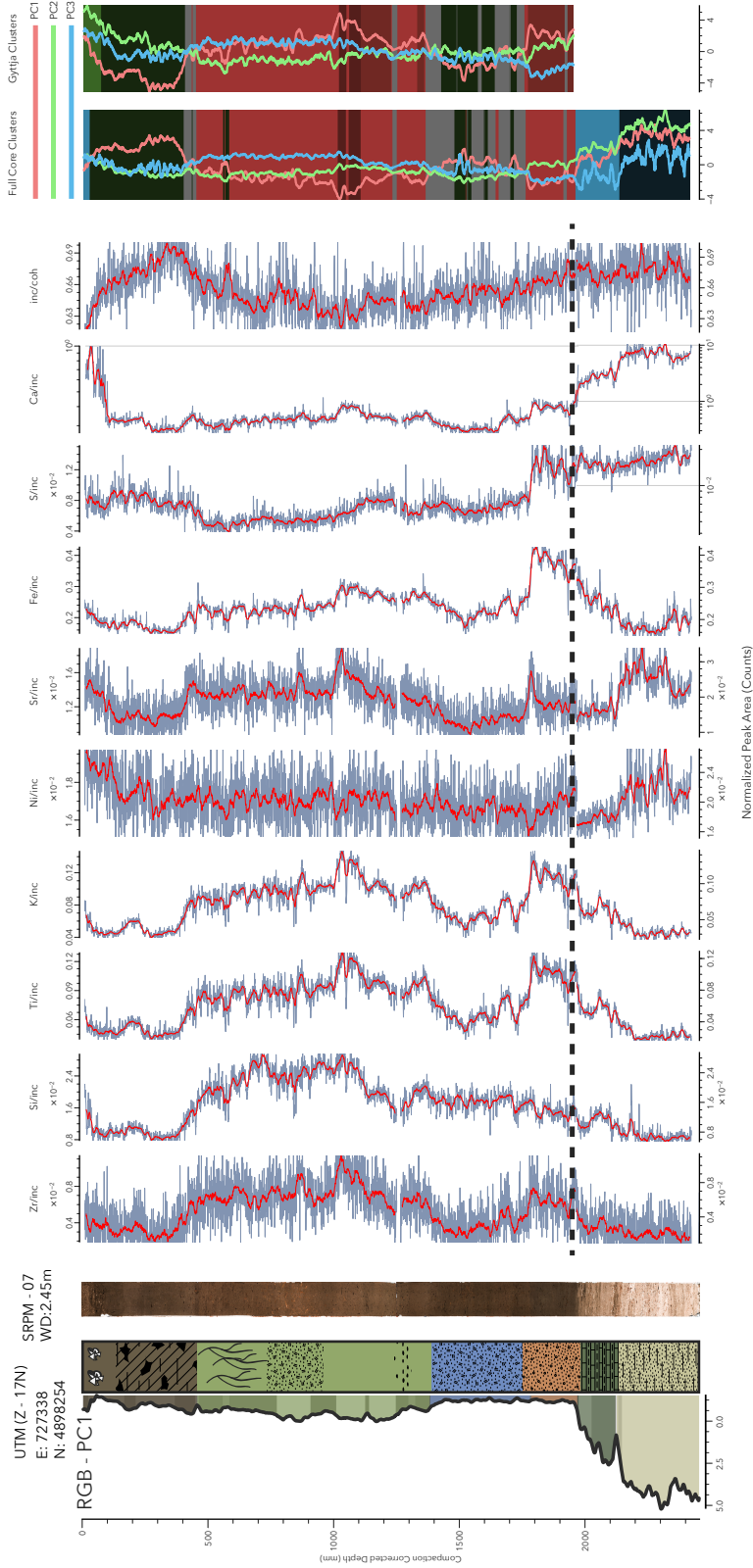


Figure A2.8: μ -XRF profile and RGB core scans for SRPM-07, including FCM and GOM chemofacies and PCA results. XRF peak areas are normalized to incoherent scattering. Red line indicates change in XRF scales - scales for measurements above and below the dashed line are displayed at the top, and bottom of the plot, respectively. Lithofacies interpretation also included. RGB image brightness (PC1) plotted in standard deviations.

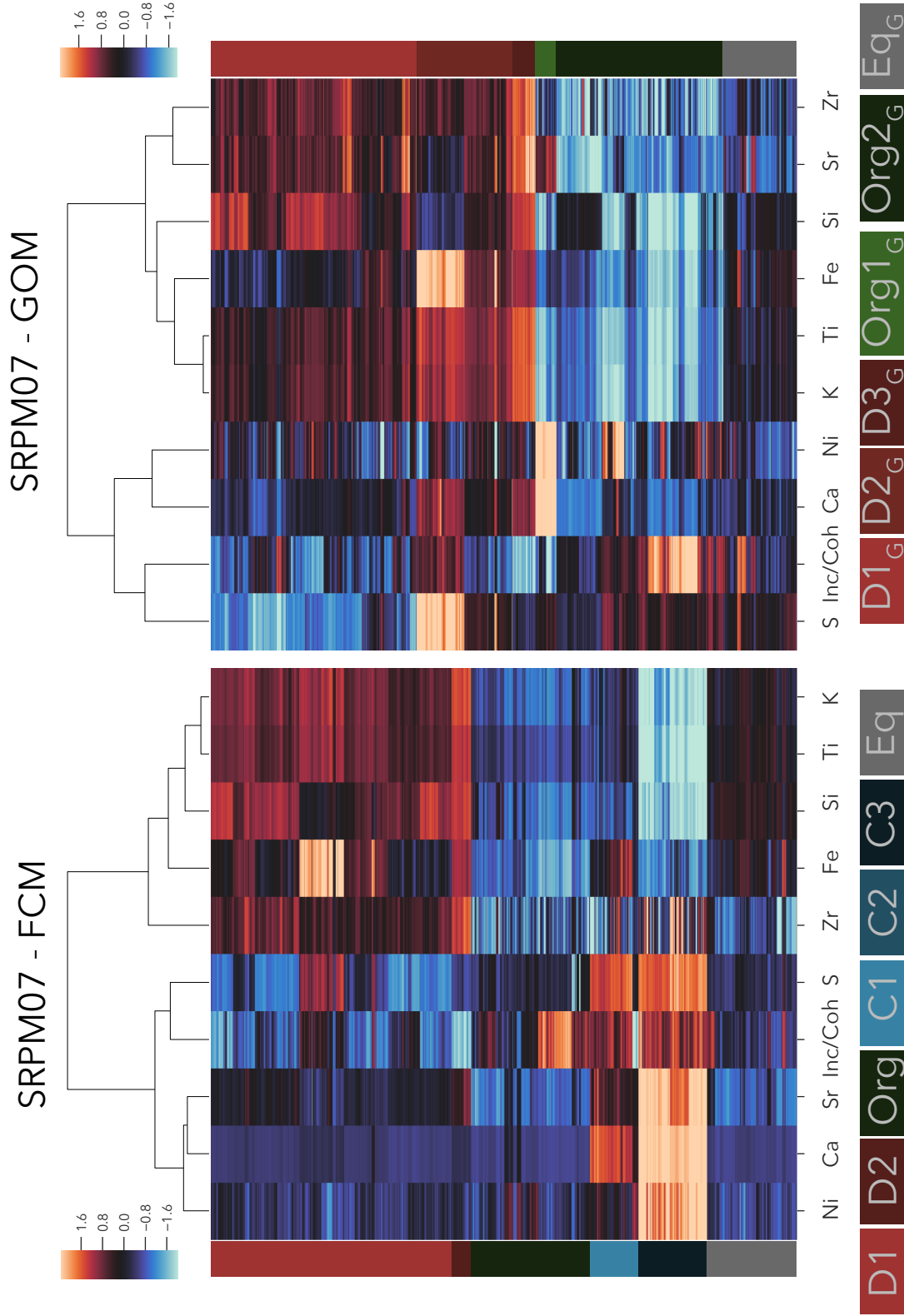


Figure A2.9: Heatmaps and R-mode dendrograms showing element associations within-core, plotted with respect to chemofacies (Data in non-stratigraphic order). Element values are standardized, and in units of standard deviations. Results are shown for both the FCM and GOM.

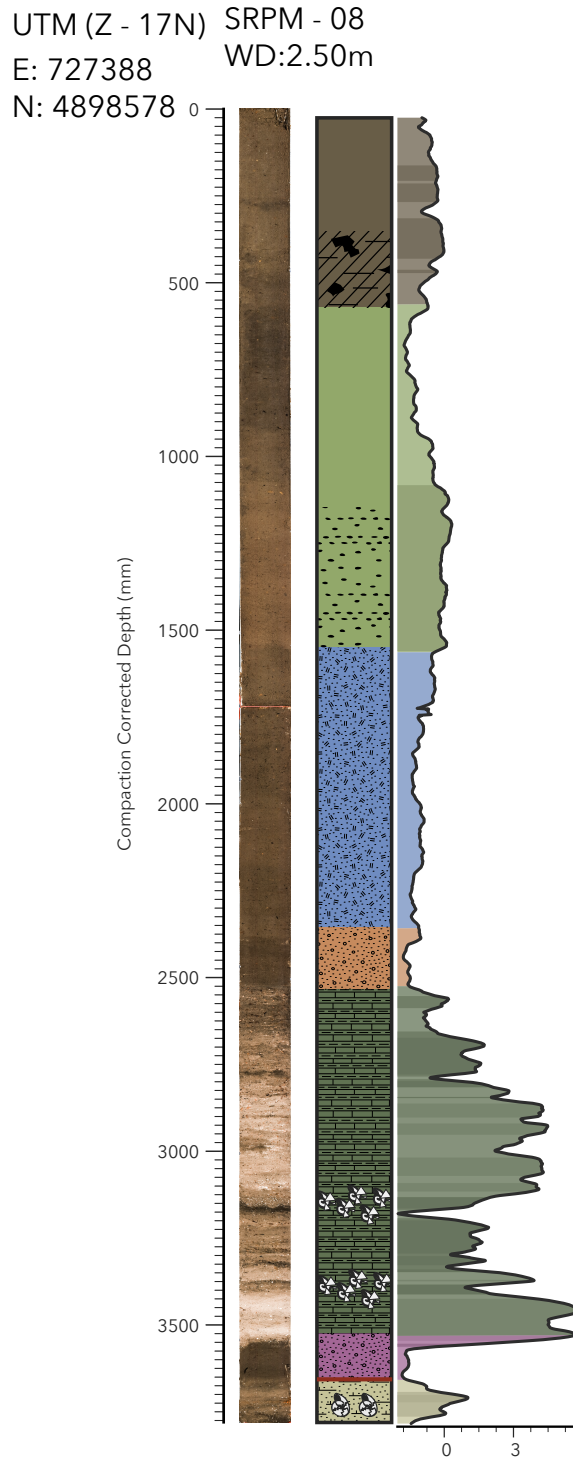


Figure A2.10: RGB core scan for SRPM-06. RGB image brightness (PC1) plotted in standard deviations. Lithofacies interpretation also included.

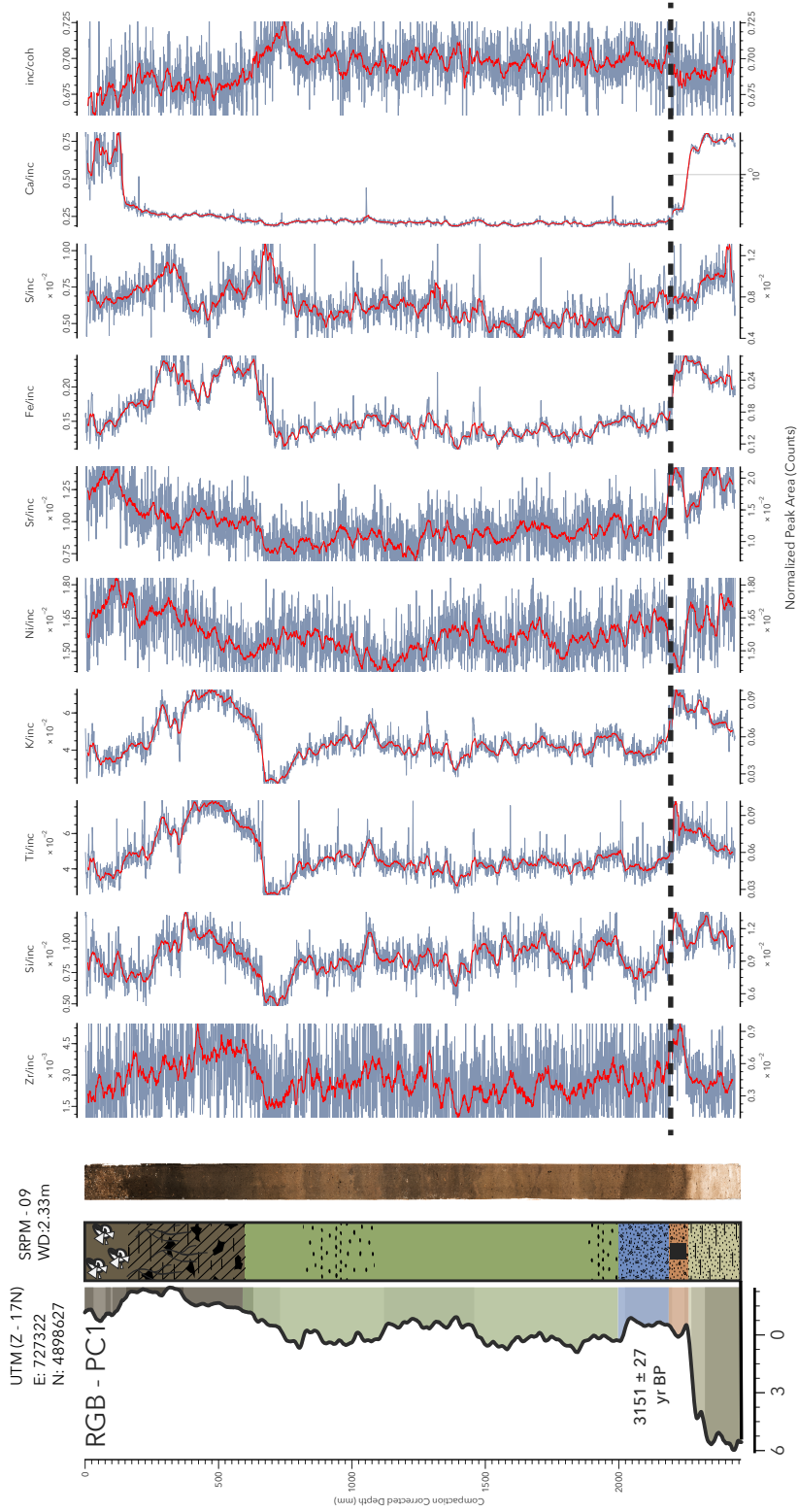


Figure A2.11: μ -XRF profile and RGB core scans for SRPM-09. XRF peak areas are normalized to incoherent scattering. Red line overlapping element traces is a 1 cm moving average of normalized count values. Dashed line indicates change in XRF scales - scales for measurements above and below the dashed line are displayed at the top, and bottom of the plot, respectively. Lithofacies interpretation also included. RGB image brightness (PC1) plotted in standard deviations.

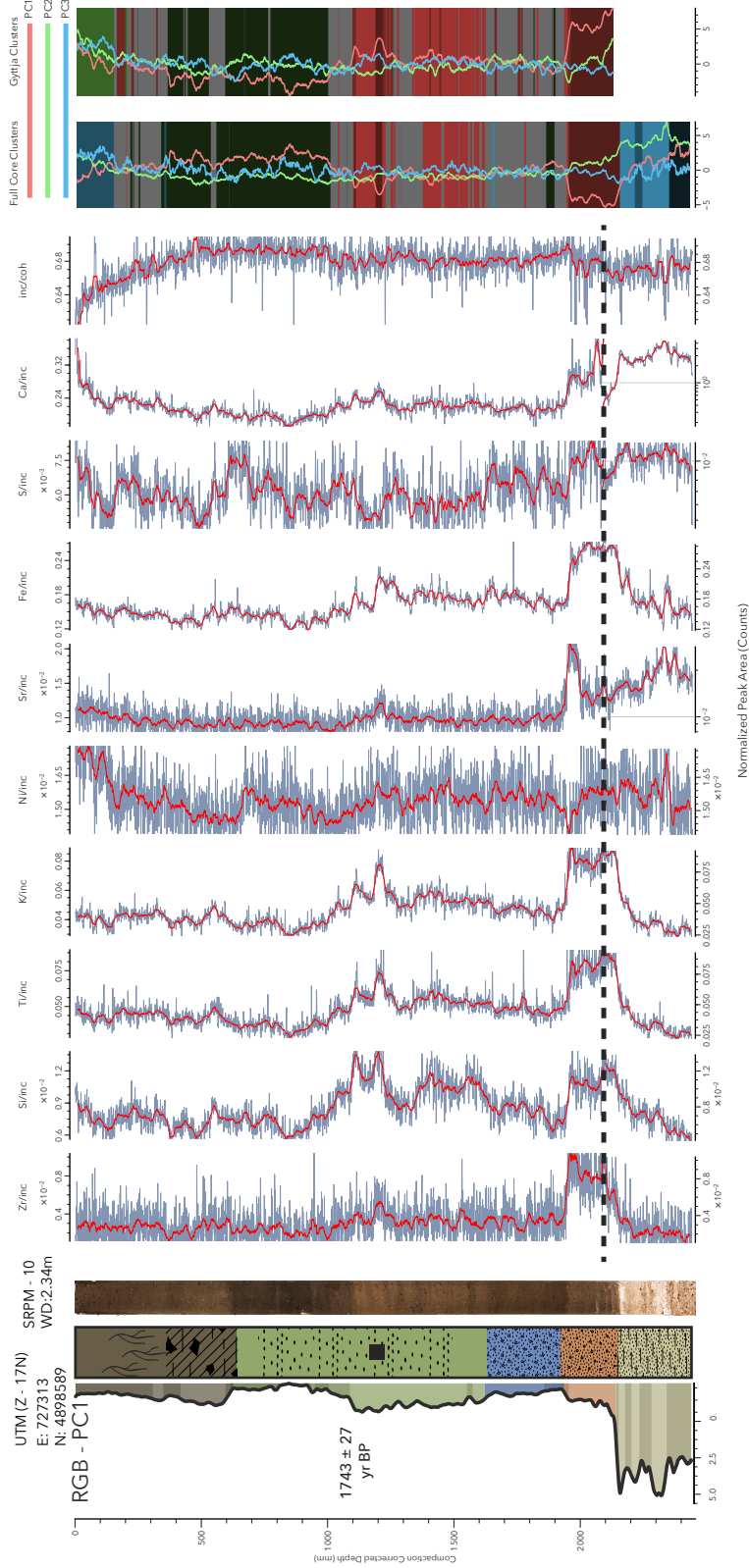


Figure A2.12: μ -XRF profile and RGB core scans for SRPM-10, including FCM and GOM chemofacies and PCA results. XRF peak areas are normalized to incoherent scattering. Red line overlapping element traces is a 1 cm moving average of normalized count values. Dashed line indicates change in XRF scales - scales for measurements above and below the dashed line are displayed at the top, and bottom of the plot, respectively. Lithofacies interpretation also included. RGB image brightness (PC1) plotted in standard deviations.

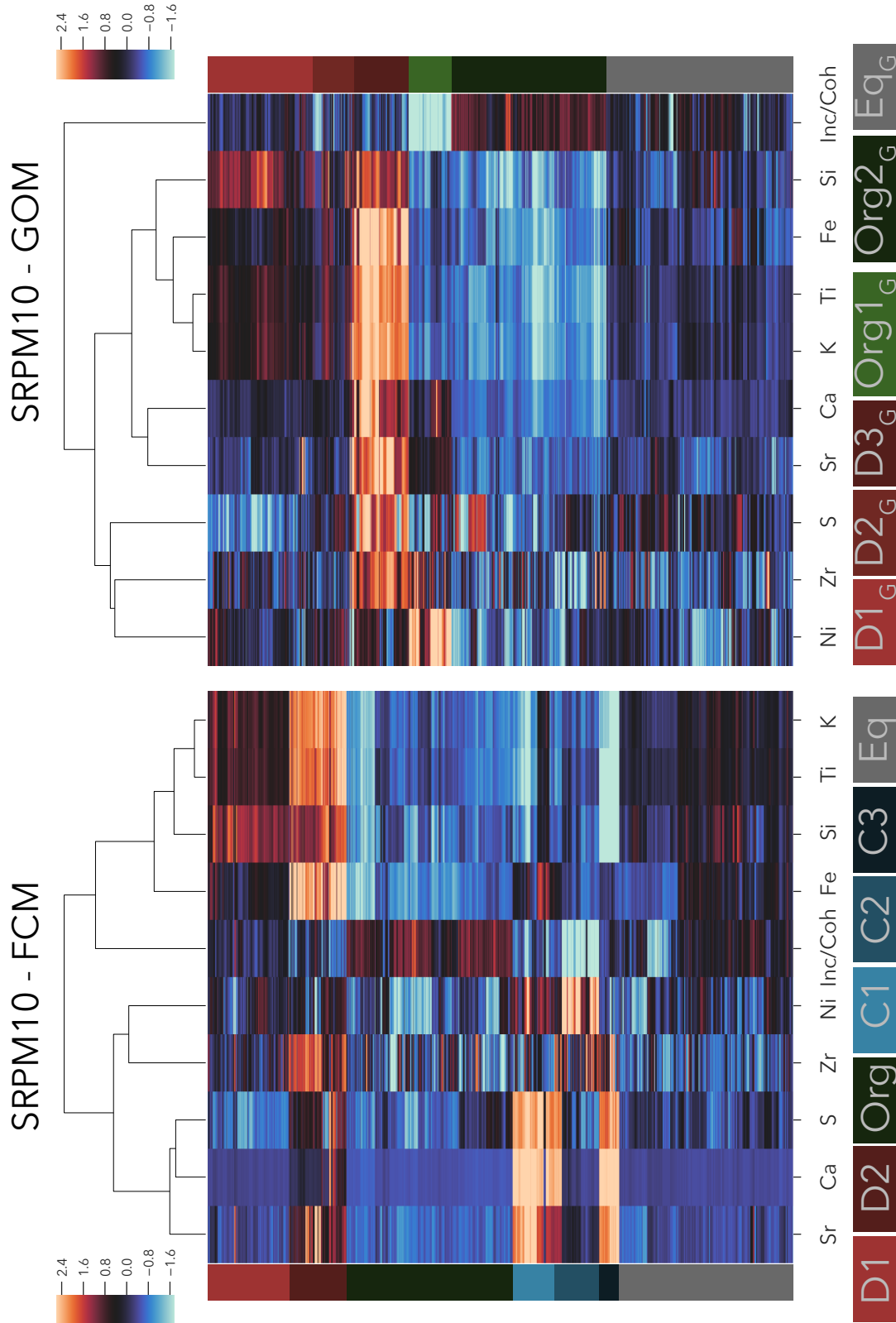


Figure A2.13: Heatmaps and R-mode dendrograms showing element associations within-core, plotted with respect to chemofacies (Data in non-stratigraphic order). Element values are standardized, and in units of standard deviations. Results are shown for both the FCM and GOM.

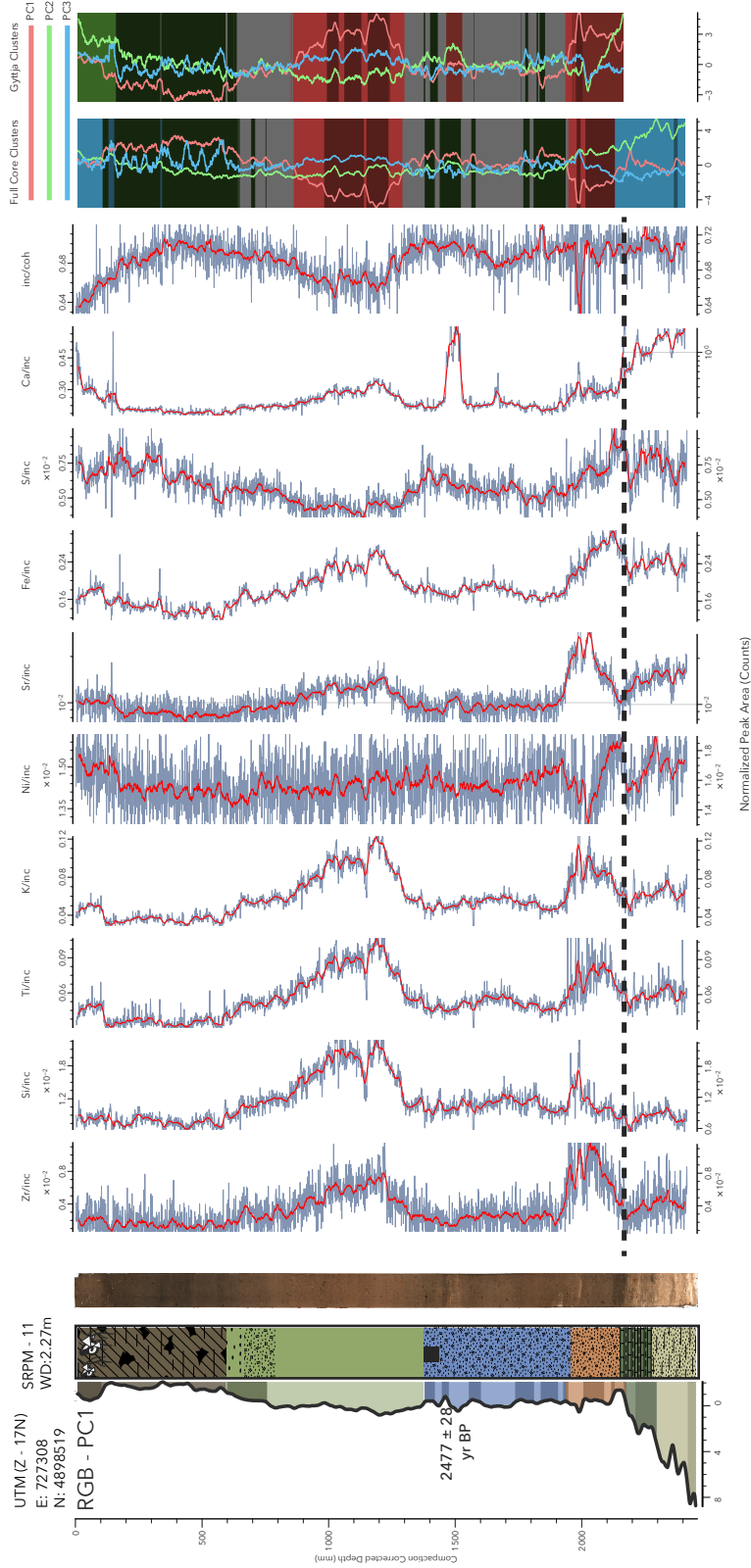


Figure A2.14: μ -XRF profile and RGB core scans for SRPM-11, including FCM and GOM chemofacies and PCA results. XRF peak areas are normalized to incoherent scattering. Red line overlapping element traces is a 1 cm moving average of normalized count values. Dashed line indicates change in XRF scales - scales for measurements above and below the dashed line are displayed at the top, and bottom of the plot, respectively. Lithofacies interpretation also included. RGB image brightness (PC1) plotted in standard deviations.

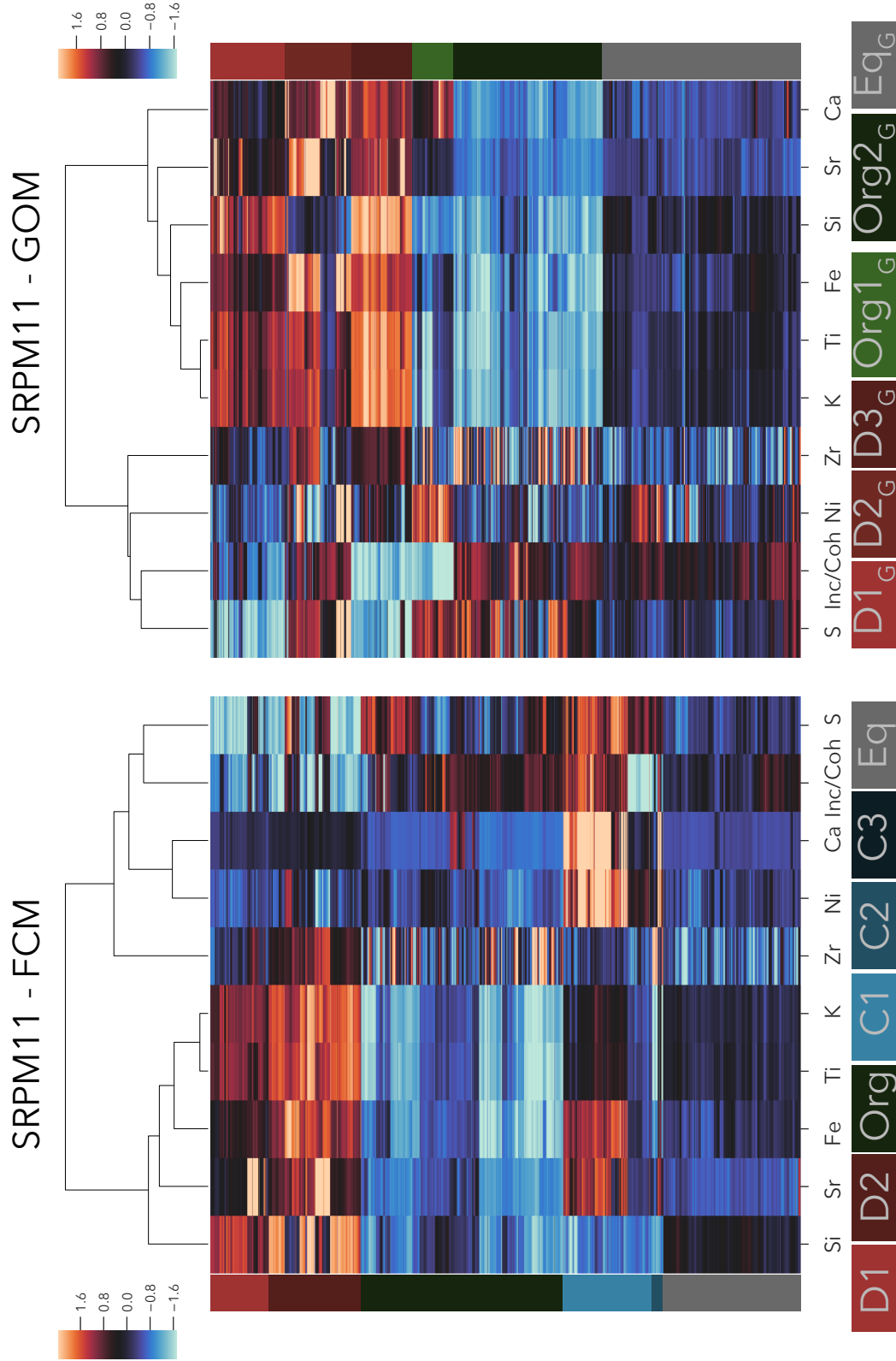


Figure A2.15: Heatmaps and R-mode dendrograms showing element associations within-core, plotted with respect to chemofacies (Data in non-stratigraphic order). Element values are standardized, and in units of standard deviations. Results are shown for both the FCM and GOM.

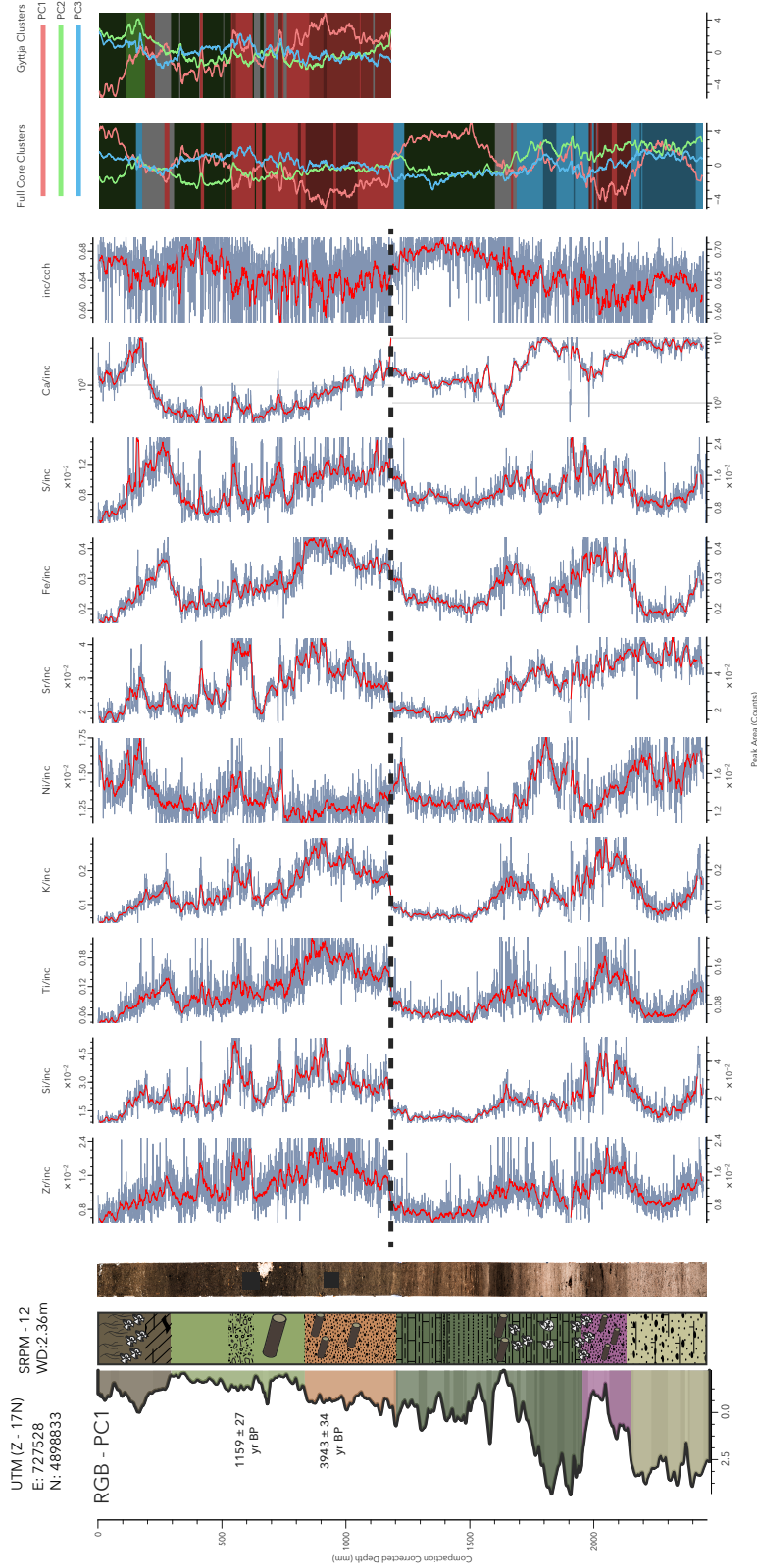


Figure A2.16: μ -XRF profile and RGB core scans for SRPM-12, including FCM and GOM chemofacies and PCA results. XRF peak areas are normalized to incoherent scattering. Red line overlapping element traces is a 1 cm moving average of normalized count values. Dashed line indicates change in XRF scales - scales for measurements above and below the dashed line are displayed at the top, and bottom of the plot, respectively. Lithofacies interpretation also included. RGB image brightness (PC1) plotted in standard deviations.

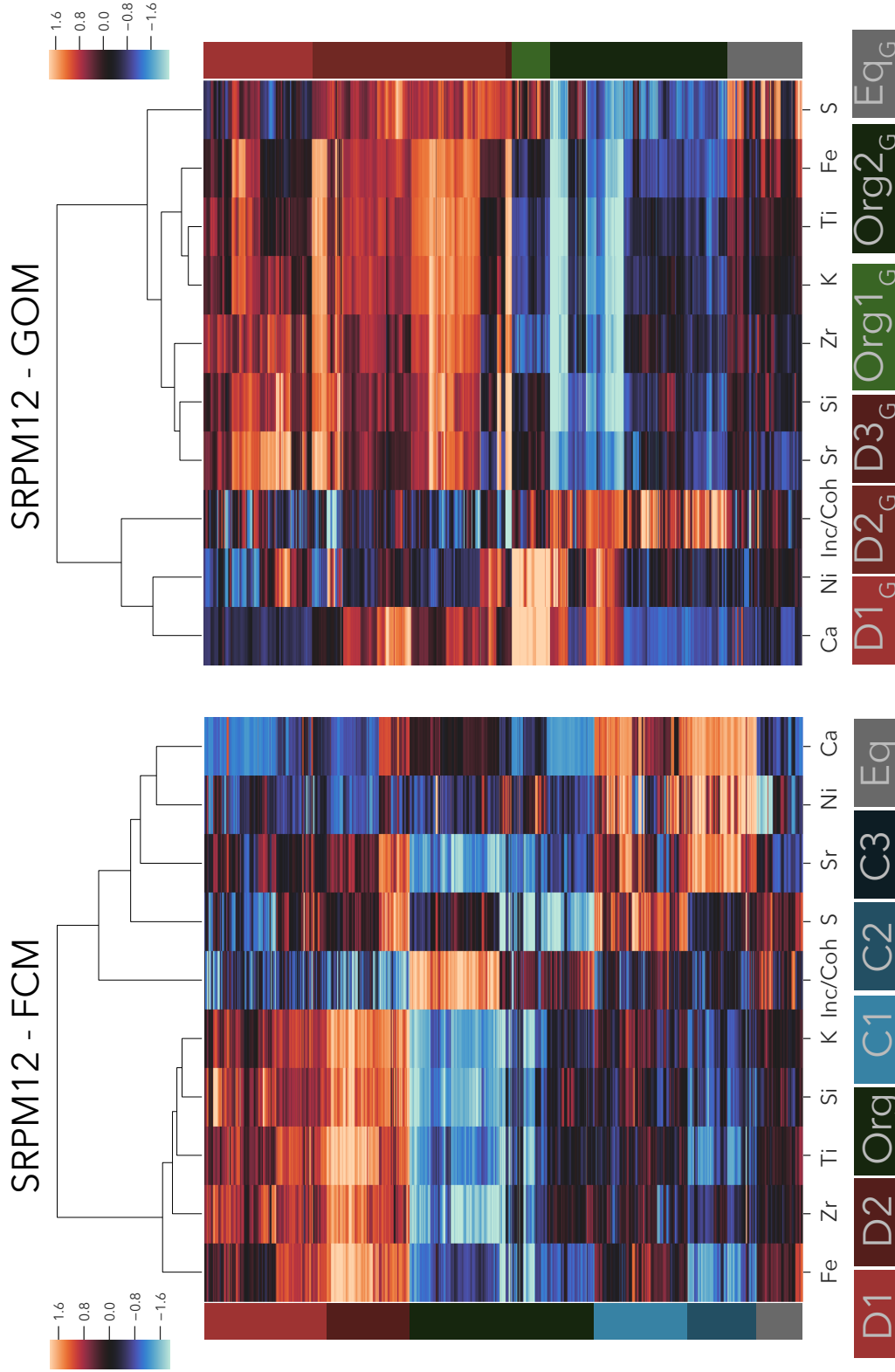


Figure A2.17: Heatmaps and R-mode dendrograms showing element associations within-core, plotted with respect to chemofacies (Data in non-stratigraphic order). Element values are standardized, and in units of standard deviations. Results are shown for both the FCM and GOM.

Table A2.2: Microfossil count statistics for SRPM02 gytjtja.

Interval (cm)	0.25	5	10	15	20	25	30	35	40	45	50	55	60	65	70	75	80	85	90	95	100	105	110	115	120	125	130	135	140	145	150	155	160	165	170	175	180		
Volume Counted (cm ³)	0.156	0.156	0.313	0.469	0.469	0.156	0.469	0.469	0.313	0.313	0.313	0.469	0.781	0.625	0.625	0.313	0.469	0.469	0.469	0.469	0.469	0.781	0.469	0.313	0.313	0.313	0.469	0.469	0.625	0.625	0.625	0.469	0.625	0.625	0.313	0.469			
SDI	2.38	2.12	2.29	2.19	2.36	2.03	2.32	2.08	2.30	2.31	2.33	2.24	2.21	2.11	2.18	2.07	2.39	2.37	2.30	2.35	2.26	2.29	2.24	2.27	2.63	2.16	1.55	2.29	2.25	2.20	2.25	2.33	2.12	2.11	1.99	1.82	1.85		
Biofacies	B3	B5	B2	B4	B2	B4	B5	B4	B2	B5	B4	B2																											
<i>A. vulgaris</i>	15	15	13	64	41	78	23	49	52	10	14	15	21	28	10	67	30	16	29	32	29	33	16	20	35	66	109	22	16	17	18	18	32	24	22	20	26		
fractional abundance (%)	7.69	7.28	5.88	18.34	11.08	34.36	8.49	15.81	18.44	5.99	6.17	6.17	8.24	11.07	4.81	26.80	11.15	4.43	12.61	13.28	9.12	12.18	7.44	6.45	12.03	22.22	5.17	9.48	7.80	6.30	8.00	5.61	14.75	9.56	14.01	19.42	22.41		
standard error (z)	1.48	1.40	1.73	2.78	2.19	2.44	2.27	2.78	2.53	2.01	1.75	2.07	2.98	3.06	2.30	3.07	2.58	1.45	2.94	2.39	2.17	2.67	2.40	2.42	2.56	2.64	3.75	2.58	2.51	2.29	2.80	1.99	3.23	2.88	4.29	4.27	5.20		
<i>Bullimaria</i> spp	0	0	0	0	11	6	0	0	2	1	0	0	2	0	0	8	1	0	0	1	4	0	1	0	0	28	7	1	0	0	0	0	0	0	0	0	0	0	
fractional abundance (%)	0.00	0.00	0.00	0.00	2.97	2.64	0.00	0.00	0.71	0.60	0.00	0.78	0.00	0.00	3.20	0.37	0.00	0.00	0.41	1.26	0.00	0.47	0.00	0.00	9.43	3.29	0.45	0.00	0.00	0.00	0.00	0.00	0.00	0.00	0.00	0.00	0.00		
standard error (z)	0.00	0.00	0.00	0.00	1.18	0.82	0.00	0.00	0.55	0.65	0.00	0.96	0.00	0.00	1.22	0.50	0.00	0.00	0.45	0.84	0.00	0.62	0.00	0.00	1.86	1.34	0.58	0.00	0.00	0.00	0.00	0.00	0.00	0.00	0.00	0.00	0.00		
<i>C. aculeata</i> "aculeata"	32	22	26	33	31	20	21	35	24	11	9	26	21	25	20	33	23	25	15	15	28	19	15	38	30	13	17	14	16	27	26	24	15	27	15	10	18		
fractional abundance (%)	16.41	10.68	11.76	9.46	8.38	8.81	7.75	11.29	8.51	6.59	3.96	10.70	8.24	9.88	9.62	13.20	8.55	6.93	6.52	6.22	8.81	7.01	6.98	12.26	10.31	4.38	7.98	6.03	7.80	10.00	11.56	7.48	6.91	10.76	9.55	9.71	15.52		
standard error (z)	2.05	1.67	2.37	2.10	1.93	1.46	2.18	2.41	1.82	2.10	1.42	2.66	2.98	2.91	3.17	2.35	2.29	1.79	2.18	1.71	2.13	2.08	2.33	3.23	2.39	1.30	2.03	2.10	2.51	2.83	3.30	2.27	2.31	3.03	3.64	3.20	4.51		
<i>C. aculeata</i> "discoides"	10	5	4	14	21	15	25	12	22	16	26	25	24	10	18	8	14	32	19	13	19	13	25	15	20	11	23	15	20	11	19	19	21	19	12	8	5	6	
fractional abundance (%)	5.13	2.43	1.81	4.01	5.68	6.61	9.23	3.87	7.80	9.58	11.45	10.29	9.41	3.95	8.65	3.20	5.20	8.86	8.26	5.39	7.23	5.54	5.12	7.42	5.15	6.73	5.16	10.78	7.80	7.04	8.44	6.54	8.76	4.78	5.10	4.85	5.17		
standard error (z)	1.22	0.83	0.98	1.41	1.61	1.28	2.36	1.47	1.75	2.50	2.32	2.62	3.17	1.90	3.02	1.22	1.82	2.01	2.44	1.59	1.95	1.86	2.02	2.58	1.74	1.59	1.66	2.73	2.51	2.41	2.87	2.14	2.57	2.09	2.72	2.32	2.76		
<i>C. constricta</i> "aerophila"	9	7	7	29	19	6	19	23	23	11	12	16	15	12	16	15	10	6	18	11	14	17	31	27	20	43	18	5	24	25	34	28	39	23	28	24	30		
fractional abundance (%)	4.62	3.40	3.17	8.31	5.14	2.64	7.01	7.42	8.16	6.59	5.29	6.58	5.88	9.49	9.13	2.40	3.35	4.99	4.78	5.81	5.35	11.44	12.56	6.45	14.78	6.06	2.35	10.34	12.10	12.59	14.67	11.84	13.36	13.15	17.83	23.30	25.86		
standard error (z)	1.16	0.98	1.29	1.98	1.54	0.82	2.08	2.00	1.79	2.10	1.63	2.13	2.55	2.85	3.10	1.06	1.47	1.89	1.65	1.69	2.59	3.03	2.42	2.79	1.52	1.14	2.68	2.79	3.10	3.30	3.47	3.79	4.73	4.56	5.46				
<i>C. constricta</i> "constricta"	1	2	8	0	14	5	1	7	3	13	5	6	2	3	2	5	10	6	6	14	9	2	9	6	1	1	4	8	2	5	8	2	4	1	0	0	0		
fractional abundance (%)	0.51	0.97	3.62	0.00	3.78	2.20	1.85	0.32	2.48	1.80	5.73	2.06	2.35	0.79	1.44	0.80	1.86	2.77	2.61	2.49	4.40	3.32	0.93	2.90	2.06	0.34	0.47	1.72	3.90	0.74	2.22	2.49	0.92	1.59	0.64	0.00	0.00		
standard error (z)	0.40	0.53	1.38	0.00	1.33	0.75	1.10	0.43	1.03	1.13	1.69	1.22	1.64	0.86	1.28	0.62	1.11	1.16	1.41	1.10	1.54	1.46	0.88	1.65	1.12	0.37	0.51	1.15	1.81	0.81	1.52	1.35	0.87	1.22	0.98	0.00	0.00		
<i>C. constricta</i> "spinosus"	21	10	12	23	21	19	35	60	41	29	26	44	51	32	45	15	26	23	22	31	36	34	39	38	41	38	18	38	27	42	40	45	29	40	35	20	20		
fractional abundance (%)	10.77	4.85	5.43	6.59	5.68	8.37	12.92	19.35	14.54	17.37	11.45	18.11	20.00	20.55	21.63	6.00	9.67	6.37	9.57	12.86	11.32	12.55	18.14	12.26	14.09	12.79	8.45	16.38	13.17	15.36	17.78	14.02	13.36	15.94	22.29	19.42	17.24		
standard error (z)	1.72	1.16	1.67	1.78	1.61	1.42	2.73	3.01	2.30	3.21	2.32	3.31	4.34	3.94	4.42	1.65	2.42	1.72	2.60	2.36	2.38	2.70	3.53	3.23	2.74	2.12	2.09	3.26	3.17	3.42	3.95	3.00	3.10	3.58	5.15	4.27	4.71		
<i>Corythia</i> spp	0	0	0	0	1	0	0	0	0	0	0	0	0	0	0	0	0	0	0	0	0	0	0	0	0	0	0	0	0	0	0	0	0	0	0	0	0	0	
fractional abundance (%)	0.00	0.00	0.00	0.00	0.27	0.00	0.00	0.00	0.00	0.00	0.00	0.00	0.00	0.00	0.00	0.00	0.00	0.00	0.00	0.00	0.00	0.00	0.00	0.00	0.00	0.00	0.00	0.00	0.00	0.00	0.00	0.00	0.00	0.00	0.00	0.00	0.00	0.00	
standard error (z)	0.00	0.00	0.00	0.00	0.36	0.00	0.00	0.00	0.00	0.00	0.00	0.00	0.00	0.00	0.00	0.00	0.00	0.00	0.00	0.00	0.00	0.00	0.00	0.00	0.00	0.00	0.00	0.00	0.00	0.00	0.00	0.00	0.00	0.00	0.00	0.00	0.00	0.00	
<i>C. trispinos</i>	35	65	50	46	50	2	23	21	23	15	14	14	21	13	13	17	37	38	34	29	16	26	16	28	19	8	4	24	16	22	17	31	26	20	10	3	5		
fractional abundance (%)	17.95	31.55	22.62	13.18	13.51	0.88	8.49	6.77	8.16	8.98	6.17	5.76	8.24	5.14	6.25	6.80	13.75	10.53	14.78	12.03	5.03	9.59	7.44	9.03	6.53	2.69	1.88	10.34	7.80	8.15	7.56	9.66	11.98	7.97	6.37	2.91	4.31		
standard error (z)	2.13	2.51	3.08	2.43	2.38	0.48	2.27	1.92	1.79	2.42	1.75	2.01	2.98	2.15	2.60	1.74	2.82	2.17	3.14	2.30	1.64	2.40	2.40	2.82	1.94	1.03	1.02	2.68	2.58	2.73	2.55	2.96	2.65	3.02	1.82	2.53			
<i>Cyclopyxis</i> spp	0	2	1	19	3	0	1	1	2	1	0	1	2	1	0	1	0	1	0	1	0	1	0	0	0	0	0	0	0	0	0	0	0	0	0	0	0	0	0
fractional abundance (%)	0.00	0.97	0.45	5.44	0.81	0.00	0.37	0.32	0.71	0.60	0.44	0.00	0.39	0.79	0.48	0.00	0.37	0.28	0.00	0.41	0.00	0.37	0.00	0.00	0.00	0.00	0.00	0.00	0.00	0.00	0.00	0.00	0.00	0.00	0.00	0.00	0.00		
standard error (z)	0.00	0.53	0.49	1.63	0.63	0.00	0.49	0.43	0.55	0.65	0.48	0.00	0.68	0.86	0.74	0.00	0.50	0.37	0.00	0.45	0.00	0.49	0.00	0.00	0.00	0.00	0.00	0.00	0.00	0.00	0.00	0.00	0.00	0.00	0.00	0.00	0.00	0.00	
<i>D. helms</i>	2	3	3	0	2	0	1	0	1	0	2	1	5	0	1	0	0	8	2	2	0	2	0	2	0	1	0	1	0	2	3	2	3	1	1	0	0	0	
fractional abundance (%)	1.03	1.46	1.36	0.00	0.54	0.00	0.37	0.00	0.35	0.00	0.88	0.41	1.96	0.00	0.48	0.00	2.22	0.87	0.83	0.00	0.74	0.00	0.65	0.34	0.00	0.47	0.00	0.98	1.11	0.89	0.93	0.46	0.40	0.00	0.00	0.00			
standard error (z)	0.56	0.65	0.85	0.00	0.51	0.00	0.49	0.00	0.39	0.00	0.68	0.55	1.50	0.00	0.74	0.00	1.04	0.82	0.64	0.00	0.70	0.00	0.79	0.46	0.00	0.51	0.00	0.92	0.99	0.97	0.63	0.62	0.62	0.00	0.00	0.00			
<i>D. corona</i>	6	2	3	9	17	6	9	6	4	2	9	3	2	4	1	1	9	13	3	7	10	5	9	7	7	4	0	3	5										

Bibliography

- Abrams, E. M. and Freter, A. (2005). *The emergence of the Moundbuilders: the archaeology of tribal societies in southeastern Ohio*. Ohio University Press.
- Allen, J. (2000). Holocene coastal lowlands in NW Europe: autocompaction and the uncertain ground. *Geological Society, London, Special Publications* 175(1), 239–252.
- Anderson, J. (1968). ART AND ARCHAEOLOGY Ce Physical Anthropology. *Royal Ontario M.*
- Anderson, T. W. and Lewis, C. F. M. (2012). A new water-level history for Lake Ontario basin: Evidence for a climate-driven early Holocene lowstand. *Journal of Paleolimnology* 47(3), 513–530. issn: 09212728.
- Arnaud, F., Révillon, S., Debret, M., Revel, M., Chapron, E., Jacob, J., Giguët-Covex, C., Poulénard, J., and Magny, M. (2012). Lake Bourget regional erosion patterns reconstruction reveals Holocene NW European Alps soil evolution and paleohydrology. *Quaternary Science Reviews* 51, 81–92. issn: 02773791.
- Artursson, M., Earle, T., and Brown, J. (2016). The construction of monumental landscapes in low-density societies: New evidence from the Early Neolithic of Southern Scandinavia (4000–3300 BC) in comparative perspective (November 5, 2015). *Journal of Anthropological Archaeology* 41, 1–18.
- Balascio, N. L., Francus, P., Bradley, R. S., Schupack, B. B., Miller, G. H., Kvisvik, B. C., Bakke, J., and Thordarson, T. (2015). Investigating the Use of Scanning X-Ray Fluorescence to Locate Cryptotephra in Minerogenic Lacustrine Sediment: Experimental Results. In: *Micro-XRF Studies of Sediment Cores*. Springer, 305–324.

BIBLIOGRAPHY

- Balascio, N. L., Zhang, Z., Bradley, R. S., Perren, B., Dahl, S. O., and Bakke, J. (2011). A multi-proxy approach to assessing isolation basin stratigraphy from the Lofoten Islands, Norway. *Quaternary Research* 75(1), 288–300.
- Bates, M., Barham, A., Jones, S., Parfitt, K., Parfitt, S., Pedley, M., Preece, R., Walker, M., and Whittaker, J. (2008). Holocene sequences and archaeology from the Crabble Paper Mill site, Dover, UK and their regional significance. *Proceedings of the Geologists' Association* 119(3-4), 299–327.
- Beckhoff, B., Kanngießler, B., Langhoff, N., Wedell, R., and Wolff, H. (2007). *Handbook of practical X-ray fluorescence analysis*. Springer Science & Business Media.
- Bernardini, W. (2004). Hopewell geometric earthworks: a case study in the referential and experiential meaning of monuments. *Journal of Anthropological Archaeology* 23(3), 331–356.
- Berntsson, A., Jansson, K. N., Kylander, M. E., De Vleeschouwer, F., and Bertrand, S. (2015). Late Holocene high precipitation events recorded in lake sediments and catchment geomorphology, Lake Vuoksjävråttje, NW Sweden. *Boreas* 44(4), 676–692.
- Berntsson, A., Rosqvist, G. C., and Velle, G. (2014). Late-Holocene temperature and precipitation changes in Vindelfjällen, mid-western Swedish Lapland, inferred from chironomid and geochemical data. *The Holocene* 24(1), 78–92.
- Bird, M. I., Fifield, L. K., Chua, S., and Goh, B. (2004). Calculating sediment compaction for radiocarbon dating of intertidal sediments. *Radiocarbon* 46(1), 421–435.
- Blaauw, M. (2010). Methods and code for 'classical' age-modelling of radiocarbon sequences. *Quaternary Geochronology* 5(5), 512–518. issn: 18711014.
- Blaauw, M. and Christen, J. A. (2011). Flexible paleoclimate age-depth models using an autoregressive gamma process. *Bayesian Analysis* 6(3), 457–474. issn: 19360975.
- Bloemsma, M., Croudace, I., Daly, J. S., Edwards, R. J., Francus, P., Galloway, J. M., Gregory, B. R., Huang, J.-J. S., Jones, A. F., Kylander, M., et al. (2018). Practical guidelines

BIBLIOGRAPHY

- and recent advances in the Itrax XRF core-scanning procedure. *Quaternary International*.
- Bloemsma, M. (2015). Development of a Modelling Framework for Core Data Integration using XRF Scanning. PhD thesis. TU Delft, Delft University of Technology.
- Boës, X., Rydberg, J., Martinez-Cortizas, A., Bindler, R., and Renberg, I. (2011). Evaluation of conservative lithogenic elements (Ti, Zr, Al, and Rb) to study anthropogenic element enrichments in lake sediments. *Journal of Paleolimnology* 46(1), 75–87. issn: 09212728.
- Boivin, N. et al. (2013). From the earth: minerals and meaning in the Hopewellian world. In: *Soils Stones and Symbols Cultural Perceptions of the Mineral World*. Routledge, 57–84.
- Bouchard, F., Francus, P., Pienitz, R., and Laurion, I. (2011). Sedimentology and geochemistry of thermokarst ponds in discontinuous permafrost, subarctic Quebec, Canada. *Journal of Geophysical Research: Biogeosciences* 116(G2).
- Boyce, J. I. and Eyles, N. (1991). Drumlins carved by deforming till streams below the Laurentide ice sheet. *Geology* 19(8), 787–790.
- Boyle, D. (1897). Mounds. *Annual Archaeological Report, Ontario*, 14–57.
- Boyle, J. F., Chiverrell, R. C., and Schillereff, D. (2015). Approaches to water content correction and calibration for μ -XRF core scanning: comparing X-ray scattering with simple regression of elemental concentrations. In: *Micro-XRF Studies of Sediment Cores*. Springer, 373–390.
- Bradley, R. (1998). Ruined buildings, ruined stones: Enclosures, tombs and natural places in the Neolithic of south-west England. *World Archaeology* 30(1), 13–22.
- Brigham-Grette, J., Melles, M., Minyuk, P., Andreev, A., Tarasov, P., DeConto, R., Koenig, S., Nowaczyk, N., Wennrich, V., Rosén, P., et al. (2013). Pliocene warmth, polar amplification, and stepped Pleistocene cooling recorded in NE Arctic Russia. *Science* 340(6139), 1421–1427.

BIBLIOGRAPHY

- Brown, J. A. (2014). North American mound builders: Hopewell, Natchez, Cahokia. In: *Encyclopedia of Global Archaeology*. Springer, 5390–5395.
- Brown, P. H., Welch, R. M., and Cary, E. E. (1987). Nickel: A micronutrient essential for higher plants. *Plant physiology* 85(3), 801–803.
- Bryant, M., Falk, P., and Paola, C. (1995). Experimental study of avulsion frequency and rate of deposition. *Geology* 23(4), 365–368.
- Burden, E. T., McAndrews, J. H., and Norris, G. (1986). Palynology of Indian and European forest clearance and farming in lake sediment cores from Awenda Provincial Park, Ontario. *Canadian Journal of Earth Sciences* 23(1), 43–54. issn: 0008-4077.
- Burks, J. (2014). Geophysical survey at Ohio earthworks: updating nineteenth century maps and filling the ‘empty’ spaces. *Archaeological Prospection* 21(1), 5–13.
- Burn, M. J. and Palmer, S. E. (2014). Solar forcing of Caribbean drought events during the last millennium. *Journal of Quaternary Science* 29(8), 827–836.
- Burnett, A. P., Soreghan, M. J., Scholz, C. A., and Brown, E. T. (2011). Tropical East African climate change and its relation to global climate: a record from Lake Tanganyika, Tropical East Africa, over the past 90+ kyr. *Palaeogeography, Palaeoclimatology, Palaeoecology* 303(1-4), 155–167.
- Carr, C. and Case, D. T. (2006). *Gathering Hopewell: Society*. Springer Publishing New York.
- Carson, D. (1980). Paleozoic Geology of the Burleigh Falls–Peterborough Area, District of Southern Ontario. *Ontario Geologic Survey Map*, 2337.
- Chagué-Goff, C., Chan, J. C. H., Goff, J., and Gadd, P. (2016). Late Holocene record of environmental changes, cyclones and tsunamis in a coastal lake, Mangaia, Cook Islands. *Island Arc* 25(5), 333–349.
- Chawchai, S., Chabangborn, A., Fritz, S., Väiliranta, M., Mörth, C.-M., Blaauw, M., Reimer, P. J., Krusic, P. J., Löwemark, L., and Wohlfarth, B. (2015). Hydroclimatic shifts in

BIBLIOGRAPHY

- northeast Thailand during the last two millennia—The record of Lake Pa Kho. *Quaternary Science Reviews* 111, 62–71.
- Chawchai, S., Kylander, M. E., Chabangborn, A., Löwemark, L., and Wohlfarth, B. (2016). Testing commonly used X-ray fluorescence core scanning-based proxies for organic-rich lake sediments and peat. *Boreas* 45(1), 180–189. issn: 15023885.
- Chuparina, E. V. and Azovsky, M. G. (2016). Elemental analysis of aquatic plants by X-ray fluorescence. *Analytical Letters* 49(12), 1963–1973.
- Clark, A. et al. (2010–). *Pillow (PIL Fork)*. [Online; accessed <today>].
- Clarke, A. H. (1981). *The freshwater molluscs of Canada*.
- Clement, A. C., Seager, R., and Cane, M. a. (2000). Suppression of El Nifio during the mid-Holocene by changes in the Earth ' s orbit. *Paleoceanography* 15(6), 731–737. issn: 0883-8305.
- Cohen, K., Finney, S., Gibbard, P., and Fan, J.-X. (2018). The ICS International Chronostratigraphic Chart. *Episodes* 36(199-204).
- Colman, S., Brown, E., and Rush, R. (2013). Mid-Holocene drought and lake-level change at Elk Lake, Clearwater County, Minnesota: Evidence from CHIRP seismic-reflection data. *The Holocene* 23(3), 460–465.
- Crann, C. A., Murseli, S., St-Jean, G., Zhao, X., Clark, I. D., and Kieser, W. E. (2017). First status report on radiocarbon sample preparation techniques at the AE Lalonde AMS Laboratory (Ottawa, Canada). *Radiocarbon* 59(3), 695–704.
- Croudace, I. W. (2006). ITRAX: description and evaluation of a new multi-function X-ray core scanner. *Geological Society, London, Special Publications* 267(1), 51–63. issn: 0305-8719.
- Croudace, I. W. and Rothwell, R. G. (2015a). ItraxPlot: An Intuitive Flexible Program for Rapidly Visualising Itrax Data. In: *Micro-XRF Studies of Sediment Cores*. Springer, 613–624.

BIBLIOGRAPHY

- Croudace, I. W. and Rothwell, R. G. (2015b). *Micro-XRF Studies of Sediment Cores: Applications of a non-destructive tool for the environmental sciences (Developments in Paleoenvironmental Research)*. Vol. 2, 464. isbn: 0306476703.
- Curtis, J. E. (2002). A Revised Temporal Framework for Middle Woodland Ceramics in South-Central Ontario. *Ontario Archaeology* 73(Figure 2), 15–28.
- Curtis, J. E. (2014). *Migration and Cultural Change: The Northern Iroquoian Case in South-Central Ontario*. Vol. 27, 2, 145–195. isbn: 1096301490.
- Cuven, S., Francus, P., Crémer, J. F., and Bérubé, F. (2015). Optimization of Itrax core scanner protocols for the micro X-ray fluorescence analysis of finely laminated sediment: A case study of lacustrine varved sediment from the high arctic. In: *Micro-XRF Studies of Sediment Cores*. Springer, 279–303.
- Cuven, S., Francus, P., and Lamoureux, S. (2011). Mid to Late Holocene hydroclimatic and geochemical records from the varved sediments of East Lake, Cape Bounty, Canadian High Arctic. *Quaternary Science Reviews* 30(19-20), 2651–2665. issn: 02773791.
- Cuven, S., Francus, P., and Lamoureux, S. F. (2010). Estimation of grain size variability with micro X-ray fluorescence in laminated lacustrine sediments, Cape Bounty, Canadian High Arctic. *Journal of Paleolimnology* 44(3), 803–817.
- Dallimore, A., Schröder-Adams, C. J., and Dallimore, S. R. (2000). Holocene environmental history of thermokarst lakes on Richards Island, Northwest Territories, Canada: thecamoebians as paleolimnological indicators. *Journal of Paleolimnology* 23(3), 261–283.
- Dean, W. E., Ahlbrandt, T. S., Anderson, R. Y., and Platt Bradbury, J. (1996). Regional aridity in North America during the middle Holocene. *The Holocene* 6(2), 145–155.
- Dillane, J. B. (2010). *Visibility Analysis of the Rice Lake Burial Mounds and Related Sites*.
- Dougherty, K. (2003). Social Organisation and Mortuary Program of the Rice Lake-Trent River Middle Woodland Hopewellian Manifestation at Cameron's Point.

BIBLIOGRAPHY

- Duckworth, P. B. (1979). The late depositional history of the western end of the Oak Ridges Moraine, Ontario. *Canadian Journal of Earth Sciences* 16(5), 1094–1107.
- Duthie, H., Yang, J., Edwards, T., Wolfe, B., and Warner, B. (1996). Hamilton Harbour, Ontario: 8300 years of limnological and environmental change inferred from microfossil and isotopic analyses. *Journal of Paleolimnology* 15(1), 79–97.
- Edwards, T. W. D. and Fritz, P. (1986). Assessing meteoric water composition and relative humidity from ^{18}O and ^2H in wood cellulose: paleoclimatic implications for southern Ontario, Canada. *Applied Geochemistry* 1(6), 715–723.
- Edwards, T. W. D. and Fritz, P. (1988). Stable-isotope paleoclimate records for southern Ontario, Canada : comparison of results from marl and wood. *Canadian Journal of Earth Sciences* 25(1986), 1397–1406. issn: 00084077 (ISSN).
- Edwards, T. W., Wolfe, B. B., and Macdonald, G. M. (1996). Influence of changing atmospheric circulation on precipitation $\delta^{18}\text{O}$ –temperature relations in Canada during the Holocene. *Quaternary Research* 46(3), 211–218.
- Edwards, T. and McAndrews, J. H. (1989). Paleohydrology of a Canadian Shield lake inferred from ^{18}O in sediment cellulose. *Canadian Journal of Earth Sciences* 26(9), 1850–1859.
- Ekdahl, E. J., Teranes, J. L., Guilderson, T. P., Turton, C. L., McAndrews, J. H., Wittkop, C. A., and Stoermer, E. F. (2004). Prehistorical record of cultural eutrophication from Crawford Lake, Canada. *Geology* 32(9), 745–748.
- Elbert, J., Wartenburger, R., Gunten, L. von, Urrutia, R., Fischer, D., Fujak, M., Hamann, Y., Greber, N. D., and Grosjean, M. (2013). Late Holocene air temperature variability reconstructed from the sediments of Laguna Escondida, Patagonia, Chile (45degree30'S). *Palaeogeography, Palaeoclimatology, Palaeoecology* 369, 482–492. issn: 00310182.
- Ellis, C. J., Timmins, P. A., and Martelle, H. (2009). At the crossroads and periphery: The Archaic archaeological record of southern Ontario. *Archaic societies: Diversity and complexity across the midcontinent*, 787–837.

BIBLIOGRAPHY

- Ellis, C. J. and Ferris, N. (1990). *The Archaeology of Southern Ontario to AD 1650*. London: London Chapter, Ontario Archaeological Society.
- Enfield, D. B., Mestas-Nuñez, A. M., and Trimble, P. J. (2001). The Atlantic multidecadal oscillation and its relation to rainfall and river flows in the continental US. *Geophysical Research Letters* 28(10), 2077–2080.
- Finkelstein, S. A. and Davis, A. M. (2006). Paleoenvironmental records of water level and climatic changes from the middle to late Holocene at a Lake Erie coastal wetland, Ontario, Canada. *Quaternary Research* 65(1), 33–43. issn: 00335894.
- Fishbein, E. and Patterson, R. T. (1993). Error-weighted maximum likelihood (EWML): a new statistically based method to cluster quantitative micropaleontological data. *Journal of Paleontology* 67(3), 475–486.
- Foerster, V., Junginger, A., Langkamp, O., Gebru, T., Asrat, A., Umer, M., Lamb, H. F., Wennrich, V., Rethemeyer, J., Nowaczyk, N., et al. (2012). Climatic change recorded in the sediments of the Chew Bahir basin, southern Ethiopia, during the last 45,000 years. *Quaternary International* 274, 25–37.
- Foreman, B. Z. and Straub, K. M. (2017). Autogenic geomorphic processes determine the resolution and fidelity of terrestrial paleoclimate records. *Science advances* 3(9), e1700683.
- Forte, E. and Pipan, M. (2008). Integrated seismic tomography and ground-penetrating radar (GPR) for the high-resolution study of burial mounds (tumuli). *Journal of Archaeological Science* 35(9), 2614–2623.
- Fortin, D., Francus, P., Gebhardt, A. C., Hahn, A., Kliem, P., Lisé-Pronovost, A., Roychowdhury, R., Labrie, J., St-Onge, G., and Team, T. P. S. (2013). Destructive and non-destructive density determination: method comparison and evaluation from the Laguna Potrok Aike sedimentary record. *Quaternary Science Reviews* 71, 147–153.
- Fritz, P., Morgan, A. V., Eicher, U., and McAndrews, J. H. (1987). Stable isotope, fossil coleoptera and pollen stratigraphy in late quaternary sediments from Ontario

BIBLIOGRAPHY

- and New York state. *Palaeogeography, Palaeoclimatology, Palaeoecology* 58(3-4), 183–202. issn: 00310182.
- Gearey, B. R. and Caseldine, C. J. (2006). Archaeological applications of testate amoebae analyses: A case study from Derryville, Co. Tipperary, Ireland. *Journal of Archaeological Science* 33(1), 49–55. issn: 10959238.
- Gorrell, G. and Brennand, T. (1997). Surficial Geology of the Rice Lake (31 D / 1) 1: 50 000 NTS map sheet, southern Ontario. *Geological Survey of Canada Open File* 3332.
- Gravenor, C. P. (1957). *Surficial Geology of the Lindsay-Peterborough Area, Ontario, Victoria, Peterborough, Durham, and Northumberland Counties, Ontario*. E. Cloutier.
- Guyard, H., Chapron, E., St-Onge, G., Anselmetti, F. S., Arnaud, F., Magand, O., Francus, P., and Mélières, M.-A. (2007). High-altitude varve records of abrupt environmental changes and mining activity over the last 4000 years in the Western French Alps (Lake Bramant, Grandes Rousses Massif). *quaternary science reviews* 26(19-21), 2644–2660.
- Haaijer, S. C., Lamers, L. P., Smolders, A. J., Jetten, M. S., and Op den Camp, H. J. (2007). Iron sulfide and pyrite as potential electron donors for microbial nitrate reduction in freshwater wetlands. *Geomicrobiology Journal* 24(5), 391–401.
- Hänsch, R. and Mendel, R. R. (2009). Physiological functions of mineral micronutrients (Cu, Zn, Mn, Fe, Ni, Mo, B, Cl). *Current opinion in plant biology* 12(3), 259–266.
- Harff, J., Endler, R., Emelyanov, E., Kotov, S., Leipe, T., Moros, M., Olea, R., Tomczak, M., and Witkowski, A. (2011). Late Quaternary climate variations reflected in Baltic Sea sediments. In: *The Baltic Sea Basin*. Springer, 99–132.
- Harrison, R. G. and Katzenberg, M. A. (2003). Paleodiet studies using stable carbon isotopes from bone apatite and collagen: Examples from Southern Ontario and San Nicolas Island, California. *Journal of Anthropological Archaeology* 22(3), 227–244. issn: 02784165.

BIBLIOGRAPHY

- Hawkes, A. D., Scott, D. B., Lipps, J. H., and Combellick, R. (2005). Evidence for possible precursor events of megathrust earthquakes on the west coast of North America. *Geological Society of America Bulletin* 117(7-8), 996–1008.
- Henry, E. R. and Barrier, C. R. (2016). The organization of dissonance in Adena-Hopewell societies of eastern North America. *World Archaeology* 48(1), 87–109.
- Herrmann, J. T., King, J. L., and Buikstra, J. E. (2014). Mapping the internal Structure of Hopewell tumuli in the lower Illinois River Valley through Archaeological Geophysics. *Advances in Archaeological Practice* 2(3), 164–179.
- Hesse, R. (2010). LiDAR-derived Local Relief Models—a new tool for archaeological prospection. *Archaeological prospection* 17(2), 67–72.
- Hoffmann, P. (2006). Non-invasive identification of chemical compounds by EDXRS. *Handbook of Practical X-ray Fluorescence Analysis*, edited by: Beckhoff, B., Kanngießner, B., Langhoff, N., Wedell, R., and Wolff, H., Springer-Verlag, Berlin Heidelberg, Germany, 769–783.
- Hovius, N., Stark, C. P., and Allen, P. A. (1997). Sediment flux from a mountain belt derived by landslide mapping. *Geology* 25(3), 231–234.
- Hugenholtz, C. H., Walker, J., Brown, O., and Myshak, S. (2014). Earthwork volumetrics with an unmanned aerial vehicle and softcopy photogrammetry. *Journal of Surveying Engineering* 141(1), 06014003.
- Hunter, J. D. (2007). Matplotlib: A 2D graphics environment. *Computing In Science & Engineering* 9(3), 90–95.
- Jarvis, S., Croudace, I. W., and Rothwell, R. G. (2015). Parameter optimisation for the ITRAX core scanner. In: *Micro-XRF Studies of Sediment Cores*. Springer, 535–562.
- Johnston, R. B. (1957). The findings after two years of work at Serpent Mounds Site, Rice Lake, Ontario. In: *Proceedings of the Indiana Academy of Science*. Vol. 67, 96–97.
- Johnston, R. B. (1968). *The archaeology of the Serpent Mounds site*. Royal Ontario Museum.

BIBLIOGRAPHY

- Johnston, R. B. (1979). Notes on ossuary burial among the Ontario Iroquois. *Canadian Journal of Archaeology/Journal Canadien d'Archéologie*, 91–104.
- Jones, E., Oliphant, T., Peterson, P., et al. (2001–). *SciPy: Open source scientific tools for Python*.
- Katzenberg, M. A. (2006). Prehistoric maize in southern Ontario. *Histories of Maize: Multidisciplinary Approaches to the Prehistory, Linguistics, Biogeography, Domestication, and Evolution of Maize*. Left Coast Press, Walnut Creek, 263–273.
- Kenyon, W. (1986). *Mounds of Sacred Earth*. Royal Ontario Museum. isbn: 0888543034.
- Koinig, K. A., Shotyky, W., Lotter, A. F., Ohlendorf, C., and Sturm, M. (2003). 9000 years of geochemical evolution of lithogenic major and trace elements in the sediment of an alpine lake—the role of climate, vegetation, and land-use history. *Journal of Paleolimnology* 30(3), 307–320.
- Kumar, A. and Dalby, A. P. (1997). Identification Key for Holocene Lacustrine Arcellacean (Thecamoebian) Taxa. *Paleontologica Electronica*.
- Kvamme, K. L. (2003). Geophysical surveys as landscape archaeology. *American Antiquity* 68(3), 435–457.
- Kylander, M. E., Ampel, L., Wohlfarth, B., and Veres, D. (2011). High-resolution X-ray fluorescence core scanning analysis of Les Echets (France) sedimentary sequence: New insights from chemical proxies. *Journal of Quaternary Science* 26(1), 109–117. issn: 02678179.
- Ladwig, R., Heinrich, L., Singer, G., and Hupfer, M. (2017). Sediment core data reconstruct the management history and usage of a heavily modified urban lake in Berlin, Germany. *Environmental Science and Pollution Research* 24(32), 25166–25178.
- Lewis, C. F. M. (2016). Geoscience Medallist 1. Understanding the Holocene Closed-Basin Phases (Lowstands) of the Laurentian Great Lakes and Their Significance*. *Geoscience Canada* 43, 179–198.

BIBLIOGRAPHY

- Lewis, C., Blasco, S. M., and Gareau, P. L. (2005). Glacial Isostatic Adjustment of the Laurentian Great Lakes Basin: Using the Empirical Record of Strandline Deformation for Reconstruction of Early Holocene Paleo-Lakes and Discovery of a Hydrologically Closed Phase. *Géographie physique et Quaternaire* 59(2-3), 187. issn: 0705-7199.
- Lintern, A., Deletic, A., Leahy, P., and McCarthy, D. (2015). Digging up the dirty past: evidence for stormwater's contribution to pollution of an urban floodplain lake. *Marine and Freshwater Research* 66(7), 596–608.
- Löwemark, L., Chen, H. F., Yang, T. N., Kylander, M., Yu, E. F., Hsu, Y. W., Lee, T. Q., Song, S. R., and Jarvis, S. (2011). Normalizing XRF-scanner data: A cautionary note on the interpretation of high-resolution records from organic-rich lakes. *Journal of Asian Earth Sciences* 40(6), 1250–1256. issn: 13679120.
- Lyle, M., Lyle, A. O., Gorgas, T., Holbourn, A., Westerhold, T., Hathorne, E. C., Kimoto, K., and Yamamoto, S. (2012). Data report : raw and normalized elemental data along the Site U1338 splice from X-ray fluorescence scanning. *Proceedings of the Integrated Ocean Drilling Program, Volume 320/321* 320, 1–19. issn: 19301014.
- Macklin, M. G. and Lewin, J. (2003). River sediments, great floods and centennial-scale Holocene climate change. *Journal of Quaternary Science: Published for the Quaternary Research Association* 18(2), 101–105.
- Maclachlan, J. C. and Eyles, C. H. (2013). Quantitative geomorphological analysis of drumlins in the Peterborough drumlin field, Ontario, Canada. *Geografiska Annaler: Series A, Physical Geography* 95(2), 125–144.
- Magnani, M. and Schroder, W. (2015). New approaches to modeling the volume of earthen archaeological features: a case-study from the Hopewell culture mounds. *Journal of Archaeological Science* 64, 12–21.
- Magurran, A. E. (1988). Why diversity? In: *Ecological diversity and its measurement*. Springer, 1–5.

BIBLIOGRAPHY

- Marlon, J. R., Pederson, N., Nolan, C., Goring, S., Shuman, B., Robertson, A., Booth, R., Bartlein, P. J., Berke, M. A., Clifford, M., et al. (2017). Climatic history of the north-eastern United States during the past 3000 years. *Climate of the Past*.
- Marshall, M. H., Lamb, H. F., Huws, D., Davies, S. J., Bates, R., Bloemendal, J., Boyle, J., Leng, M. J., Umer, M., and Bryant, C. (2011). Late Pleistocene and Holocene drought events at Lake Tana, the source of the Blue Nile. *Global and Planetary Change* 78(3-4), 147–161.
- Martín-Puertas, C., Valero-Garcés, B. L., Mata, M. P., Moreno, A., Giralt, S., Martínez-Ruiz, F., and Jiménez-Espejo, F. (2011). Geochemical processes in a Mediterranean Lake: A high-resolution study of the last 4,000 years in Zoñar Lake, southern Spain. *Journal of Paleolimnology* 46(3), 405–421. issn: 09212728.
- McAndrews, J. H. (1984). Late Quaternary vegetation history of Rice Lake, Ontario, and the McIntyre archaeological site. *RB Johnston, éd., The McIntyre Site: Archaeology, Subsistence and Environment. Archaeological Survey of Canada Paper* (126), 161–189.
- McAndrews, J. H. and Turton, C. L. (2010). Fungal spores record Iroquoian and Canadian agriculture in 2nd millennium a. d. sediment of Crawford Lake, Ontario, Canada. *Vegetation history and archaeobotany* 19(5-6), 495–501.
- McCarthy, F. and Krueger, A. (2013). Freshwater dinoflagellates in palaeolimnological studies: Peridinium cysts as proxies of cultural eutrophication in the SE Great Lakes region of Ontario, Canada. *Biological and geological perspectives of Dinoflagellates* 5, 133.
- McCarthy, F. and McAndrews, J. (2012). Early Holocene drought in the Laurentian Great Lakes basin caused hydrologic closure of Georgian Bay. *Journal of paleolimnology* 47(3), 411–428.
- McKinney, W. (2015). pandas: a Python data analysis library. see <http://pandas.pydata.org/>.
- Metcalf, S. E., Jones, M. D., Davies, S. J., Noren, A., and MacKenzie, A. (2010). Climate variability over the last two millennia in the North American Monsoon region,

BIBLIOGRAPHY

- recorded in laminated lake sediments from Laguna de Juanacatlán, Mexico. *The Holocene* 20(8), 1195–1206.
- Milner, G. (2005). *The moundbuilders: Ancient peoples of Eastern North America. Ancient people and places*. New York: Thames and Hudson. Google Scholar.
- MNR (2018). *High Resolution Digital Elevation Model (HRDEM) - CanElevation Series*.
- MNR, O. (2013). *South Central Ontario Orthophotography Project (SCOOP – 2013) Digital Terrain Model*.
- Montgomery, H. (1910). Recent archaeological investigations in Ontario. *Transaction of the Canadian Institute* 9(1), 1–12.
- Moreno, A., Giralt, S., Valero-Garcés, B., Sáez, A., Bao, R., Prego, R., Pueyo, J., González-Sampériz, P., and Taberner, C. (2007). A 14 kyr record of the tropical Andes: The Lago Chungará sequence (18 S, northern Chilean Altiplano). *Quaternary International* 161(1), 4–21.
- Moreno, A., López-Merino, L., Leira, M., Marco-Barba, J., González-Sampériz, P., Valero-Garcés, B. L., López-Sáez, J. A., Santos, L., Mata, P., and Ito, E. (2011). Revealing the last 13,500 years of environmental history from the multiproxy record of a mountain lake (Lago Enol, northern Iberian Peninsula). *Journal of Paleolimnology* 46(3), 327–349.
- MTCS (2017). *MTCS past portal archaeological site archive*.
- Mueller, N. G. (2018). The earliest occurrence of a newly described domesticate in eastern North America: Adena/Hopewell communities and agricultural innovation. *Journal of Anthropological Archaeology* 49, 39–50.
- Muller, E. H. and Prest, V. (1985). Glacial lakes in the Ontario basin. *Quaternary Evolution of the Great Lakes. Geological Association of Canada Special Paper* 30(258), 213–230.
- Munoz, S. E., Gajewski, K., and Peros, M. C. (2010). Synchronous environmental and cultural change in the prehistory of the northeastern United States. *Proceedings of the National Academy of Sciences* 107(51), 22008–22013. issn: 0027-8424.

BIBLIOGRAPHY

- Munoz, S. E. and Gajewski, K. (2010). Distinguishing prehistoric human influence on late-Holocene forests in southern Ontario, Canada. *The Holocene* 20(6), 967–981. issn: 0959-6836.
- Munoz, S. E., Schroeder, S., Fike, D. A., and Williams, J. W. (2014). A record of sustained prehistoric and historic land use from the cahokia region, illinois, USA. *Geology* 42(6), 499–502. issn: 19432682.
- Murphy, D. H. and Wilkinson, B. H. (1980). Carbonate deposition and facies distribution in a central Michigan marl lake. *Sedimentology* 27(2), 123–135.
- Nielson, K. K. (1977). Matrix corrections for energy dispersive x-ray fluorescence analysis of environmental samples with coherent/incoherent scattered x-rays. *Analytical chemistry* 49(4), 641–648.
- Ohlendorf, C., Wennrich, V., and Enters, D. (2015). Experiences with XRF-scanning of long sediment records. In: *Micro-XRF Studies of Sediment Cores*. Springer, 351–372.
- Oldfield, F., Wake, R., Boyle, J., Jones, R., Nolan, S., Gibbs, Z., Appleby, P., Fisher, E., and Wolff, G. (2003). The late-Holocene history of Gormire Lake (NE England) and its catchment: a multiproxy reconstruction of past human impact. *The Holocene* 13(5), 677–690.
- O’Neal, M. A. (2012). An objective approach to defining earthwork geometries using subdecimeter digital elevation models. *Geoarchaeology* 27(2), 157–165.
- O’Neal, M. A., O’Mansky, M. E., and MacGregor, J. A. (2005). Modeling the natural degradation of earthworks. *Geoarchaeology: An International Journal* 20(7), 739–748.
- ParksCanada (2018). *Serpent Mounds National Historical Site of Canada*. https://www.pc.gc.ca/apps/dfhd/page_nhs_eng.aspx?id=511. Accessed: 2018-09-26.
- Patterson, R. T., MacKinnon, K. D., Scott, D. B., and Medioli, F. S. (1985). Arcellaceans (“thecamoebians”) in small lakes of New Brunswick and Nova Scotia; modern distribution and Holocene stratigraphic changes. *The Journal of Foraminiferal Research* 15(2), 114–137. issn: 0096-1191.

BIBLIOGRAPHY

- Patterson, R. T., Dalby, A., Kumar, A., Henderson, L. A., and Boudreau, R. E. A. (2002). Arcellaceans (thecamoebians) as indicators of land-use change: Settlement history of the Swan lake area, Ontario as a case study. *Journal of Paleolimnology* 28(3), 297–316. issn: 09212728.
- Patterson, R. T. and Fishbein, E. (1989). Re-examination of the statistical methods used to determine the number of point counts needed for micropaleontological quantitative research. *Journal of Paleontology* 63(2), 245–248.
- Patterson, R. T. and Kumar, A. (2000). Assessment of arcellacean (thecamoebian) assemblages, species, and strains as contaminant indicators in James Lake, Northeastern Ontario, Canada. *The Journal of Foraminiferal Research* 30(4), 310–320.
- Patterson, R., Baker, T., and Burbidge, S. (1996). Arcellaceans (thecamoebians) as proxies of arsenic and mercury contamination in northeastern Ontario lakes. *The Journal of Foraminiferal Research* 26(2), 172–183.
- Pederson Weinberger, J. (2006). Ohio Hopewell Earthworks: an examination of site use from non-mound space at the Hopewell Site. PhD thesis. The Ohio State University.
- Pedregosa, F., Varoquaux, G., Gramfort, A., Michel, V., Thirion, B., Grisel, O., Blondel, M., Prettenhofer, P., Weiss, R., Dubourg, V., Vanderplas, J., Passos, A., Cournapeau, D., Brucher, M., Perrot, M., and Duchesnay, E. (2011). Scikit-learn: Machine Learning in {P}ython. *Journal of Machine Learning Research* 12, 2825–2830.
- Peet, R. K. (1974). The measurement of species diversity. *Annual review of ecology and systematics* 5(1), 285–307.
- Pérez, A. L., Rey, D., Martins, V., Plaza-Morlote, M., and Rubio, B. (Article In Press). Application of multivariate statistical analyses to Itrax TM core scanner data for the identification of deep-marine sedimentary facies: A case study in the Galician Continental Margin. *Quaternary International*.
- Poraj-Górska, A. I., Żarczyński, M. J., Ahrens, A., Enters, D., Weisbrodt, D., and Tylmann, W. (2017). Impact of historical land use changes on lacustrine sedimentation

BIBLIOGRAPHY

- recorded in varved sediments of Lake Jaczno, northeastern Poland. *Catena* 153, 182–193.
- Reimer, P. J., Bard, E., Bayliss, A., Beck, J. W., Blackwell, P. G., Ramsey, C. B., Buck, C. E., Cheng, H., Edwards, R. L., Friedrich, M., et al. (2013). IntCal13 and Marine13 radiocarbon age calibration curves 0–50,000 years cal BP. *Radiocarbon* 55(4), 1869–1887.
- Reinhardt, E. G., Little, M., Donato, S., Findlay, D., Krueger, A., Clark, C., and Boyce, J. (2005). Arcellacean (thecamoebian) evidence of land-use change and eutrophication in Frenchman’s Bay, Pickering, Ontario. *Environmental Geology* 47(5), 729–739. issn: 09430105.
- Reinhardt, E. G., Dalby, A. P., Kumar, A., and Patterson, R. T. (1998). Arcellaceans as Pollution Indicators in Mine Tailing Contaminated Lakes near Cobalt, Ontario, Canada. *Micropaleontology* 44(2), 131. issn: 00262803.
- Richardson, F. (1968). *The Trent Valley archaeological survey - 1968 field season*. Trent Archaeology Files - Trent University Department of Anthropology.
- Roberts, A. (1978). *Interim Licence and Grant Report to the Ministry of Culture and Recreation on an Archaeological Survey in Selected Townships Along the North Shore of Lake Ontario*. Manuscript – Ontario Ministry of Culture and Communications, Toronto.
- Rodríguez-Germade, I., Rubio, B., Rey, D., Vilas, F., López-Rodríguez, C. F., Comas, M. C., and Martínez-Ruiz, F. (2015). Optimization of Itrax core scanner measurement conditions for sediments from submarine mud volcanoes. In: *Micro-XRF studies of sediment cores*. Springer, 103–126.
- Roe, H. M., Patterson, R. T., and Swindles, G. T. (2010). Controls on the contemporary distribution of lake thecamoebians (testate amoebae) within the Greater Toronto Area and their potential as water quality indicators. *Journal of Paleolimnology* 43(4), 955–975. issn: 09212728.
- Romain, W. F. and Burks, J. (2008). LiDAR Imaging of the Great Hopewell Road. *Current Research in Ohio Archaeology* 2008.

BIBLIOGRAPHY

- Romans, B. W., Castelltort, S., Covault, J. A., Fildani, A., and Walsh, J. (2016). Environmental signal propagation in sedimentary systems across timescales. *Earth-Science Reviews* 153, 7–29.
- Rothwell, R. G. et al. (2015). Twenty years of XRF core scanning marine sediments: what do geochemical proxies tell us? In: *Micro-XRF Studies of Sediment Cores*. Springer, 25–102.
- Saunders, I. and Young, A. (1983). Rates of surface processes on slopes, slope retreat and denudation. *Earth Surface Processes and Landforms* 8(5), 473–501.
- Scharf, E. A. (2010). Archaeology, land use, pollen and restoration in the Yazoo Basin (Mississippi, USA). *Vegetation history and archaeobotany* 19(3), 159–175.
- Schlolaut, G., Marshall, M. H., Brauer, A., Nakagawa, T., Lamb, H. F., Staff, R. A., Ramsey, C. B., Bryant, C. L., Brock, F., Kossler, A., et al. (2012). An automated method for varve interpolation and its application to the Late Glacial chronology from Lake Suigetsu, Japan. *Quaternary Geochronology* 13, 52–69.
- Schreiber, N., Garcia, E., Kroon, A., Ilsøe, P. C., Kjær, K. H., and Andersen, T. J. (2014). Pattern Recognition on X-ray Fluorescence Records from Copenhagen Lake Sediments Using Principal Component Analysis. *Water, Air, & Soil Pollution* 225(12), 2221. issn: 0049-6979.
- Schwarcz, H. P., Melbye, J., Anne Katzenberg, M., and Knyf, M. (1985). Stable isotopes in human skeletons of Southern Ontario: reconstructing Palaeodiet. *Journal of Archaeological Science* 12(3), 187–206. issn: 10959238.
- Scott, A. D. B., Hermelin, J. O. R., Journal, S., and Jan, N. (1993). Paleontological Society A Device for Precision Splitting of Micropaleontological Samples in Liquid Suspension Published by : Paleontological Society Stable URL : <http://www.jstor.org/stable/1305976>. *Journal of Paleontology* 67(1), 151–154.
- Scott, D. B., Medioli, F. S., and Schafer, C. T. (2001). *Monitoring in coastal environments using foraminifera and thecamoebian indicators*. Cambridge University Press.

BIBLIOGRAPHY

- Shala, S., Helmens, K. F., Jansson, K. N., Kylander, M. E., Risberg, J., and Löwemark, L. (2014). Palaeoenvironmental record of glacial lake evolution during the early Holocene at S okli, NE F inland. *Boreas* 43(2), 362–376.
- Shannon, C. E. (1948). A mathematical theory of communication. *Bell system technical journal* 27(3), 379–423.
- Sharpe, D. R., Barnett, P. J., Brennand, T. A., Finley, D., Gorrell, G., Russell, H. A., and Stacey, P. (1997). *Surficial geology of the Greater Toronto and Oak Ridges Moraine area, southern Ontario*.
- Shaw, J., Sharpe, D., and Harris, J. (2010). A flowline map of glaciated Canada based on remote sensing data. *Canadian Journal of Earth Sciences* 47(1), 89–101.
- Sherratt, A. (1990). The genesis of megaliths: Monumentality, ethnicity and social complexity in Neolithic north-west Europe. *World Archaeology* 22(2), 147–167.
- Smith, D. G. (1997). Recent Investigations of Late Woodland Occupations at Cootes Paradise, Ontario. *Ontario Archaeology* 63(63), 4–16.
- Sonnenburg, E. P. (2010). Holocene Lake-Level Change and Submerged Archaeological Site Potential of Rice Lake Ontario. PhD thesis. McMaster University.
- Sonnenburg, E. P. and Boyce, J. I. (2008). Data-fused digital bathymetry and side-scan sonar as a base for archaeological inventory of submerged landscapes in the Rideau Canal, Ontario, Canada. *Geoarchaeology* 23(5), 654–674. issn: 08836353.
- Sonnenburg, E. P., Boyce, J. I., and Reinhardt, E. G. (2011). Quartz flakes in lakes: Microdebitage evidence for submerged great lakes prehistoric (Late Paleoindian-Early Archaic) tool-making sites. *Geology* 39(7), 631–634. issn: 00917613.
- Sonnenburg, E. P., Boyce, J. I., and Reinhardt, E. G. (2013). Multi-proxy lake sediment record of prehistoric (Paleoindian-Archaic) archaeological paleoenvironments at Rice Lake, Ontario, Canada. *Quaternary Science Reviews* 73, 77–92. issn: 02773791.

BIBLIOGRAPHY

- Sonnenburg, E. P., Boyce, J. I., and Suttak, P. (2012). Holocene paleoshorelines, water levels and submerged prehistoric site potential of Rice Lake (Ontario, Canada). *Journal of Archaeological Science* 39(12), 3553–3567.
- Spence, M. W., Finlayson, W. D., and Pihl, R. H. (1979). Hopewellian Influences on Middle Woodland Cultures in Southern Ontario. In: *Hopewell Archaeology: The Chillicothe Conference*, Kent State University Press, Kent, Ohio, 115–121.
- Spence, M. W., Pihl, R. H., and Molto, J. E. (1984). Hunter-gatherer social group identification: A case study from Middle Woodland southern Ontario. *Exploring the Limits: Frontiers and Boundaries in Prehistory*, 117–142.
- Spence, M. W., Pihl, R. H., and Murphy, C. (1990). Cultural complexes of the Early and Middle Woodland periods. *The Archaeology of Southern Ontario to AD 1650*, 125–169.
- Stinchcomb, G. E., Messner, T. C., Driese, S. G., Nordt, L. C., and Stewart, R. M. (2011). Pre-colonial (A.D. 1100-1600) sedimentation related to prehistoric maize agriculture and climate change in eastern North America. *Geology* 39(4), 363–366. issn: 00917613.
- Stothers, D. M. (1974). The East Sugar Island burial mound. *Pennsylvania Archaeologist* 44(4), 20–25.
- Thomson, J., Croudace, I., and Rothwell, R. (2006). A geochemical application of the ITRAX scanner to a sediment core containing eastern Mediterranean sapropel units. *Geological Society, London, Special Publications* 267(1), 65–77.
- Turner, J. N., Jones, A. F., Brewer, P. A., Macklin, M. G., and Rassner, S. M. (2015). Micro-XRF applications in fluvial sedimentary environments of Britain and Ireland: progress and prospects. In: *Micro-XRF Studies of Sediment Cores*. Springer, 227–265.
- Turton, C. and McAndrews, J. (2006). Rotifer loricas in second millennium sediment of Crawford Lake, Ontario, Canada. *Review of Palaeobotany and Palynology* 141(1-2), 1–6.
- Van Grieken, R. and Markowicz, A. (2001). *Handbook of X-ray Spectrometry*. CRC Press.

BIBLIOGRAPHY

- Volik, O., McCarthy, F. M. G., and Riddick, N. L. (2016). Insights from pollen, non-pollen palynomorphs and testate amoebae into the evolution of Lake Simcoe. *Journal of Paleolimnology* 56(2-3), 137–152. issn: 15730417.
- Vreeken, W. J. (1981). Distribution and chronology of freshwater marls between Kingston and Belleville, Ontario. *Canadian Journal of Earth Sciences* 18(7), 1228–1239.
- Walker, S. L. (2015). Cemeteries and hunter-gatherer land use patterns: a case study from the Middle Trent Valley, Ontario. PhD thesis. Trent University.
- Waskom, M., Botvinnik, O., Hobson, P., Cole, J. B., Halchenko, Y., Hoyer, S., Miles, A., Augspurger, T., Yarkoni, T., Megies, T., Coelho, L. P., Wehner, D., cynddl, Ziegler, E., diego0020, Zaytsev, Y. V., Hoppe, T., Seabold, S., Cloud, P., Koskinen, M., Meyer, K., Qalieh, A., and Allan, D. (2014). *seaborn: v0.5.0 (November 2014)*.
- Watchorn, M. A., Hamilton, P. B., and Patterson, R. T. (2013). The paleolimnology of Haynes Lake, Oak Ridges Moraine, Ontario, Canada: Documenting anthropogenic and climatic disturbances. *Environmental Earth Sciences* 68(7), 1823–1834. issn: 18666280.
- Weltje, G. J., Bloemsa, M., Tjallingii, R., Heslop, D., Röhl, U., and Croudace, I. W. (2015). Prediction of geochemical composition from XRF core scanner data: a new multivariate approach including automatic selection of calibration samples and quantification of uncertainties. In: *Micro-XRF Studies of Sediment Cores*. Springer, 507–534.
- Weltje, G. J. and Tjallingii, R. (2008). Calibration of XRF core scanners for quantitative geochemical logging of sediment cores: Theory and application. *Earth and Planetary Science Letters* 274(3-4), 423–438. issn: 0012821X.
- Wiik, E., Bennion, H., Sayer, C. D., Davidson, T. A., Clarke, S. J., McGowan, S., Prentice, S., Simpson, G. L., and Stone, L. (2015). The coming and going of a marl lake: multi-indicator palaeolimnology reveals abrupt ecological change and alternative views of reference conditions. *Frontiers in Ecology and Evolution* 3(August), 1–20. issn: 2296-701X.

BIBLIOGRAPHY

- Wiik, E., Bennion, H., Sayer, C. D., and Willby, N. J. (2013). Chemical and biological responses of marl lakes to eutrophication. *Freshwater Reviews* 6(2), 35–62.
- Wilson, J. (1993). The Rice Lake Phase reconsidered. In: *Keweenaw*. Ontario Archaeological Society - London Chapter.
- Yu, Z. and McAndrews, J. H. (1994). Holocene water levels at Rice Lake, Ontario, Canada: sediment, pollen and plant-macrofossil evidence. *The Holocene* 4(2), 141–152. issn: 0959-6836.
- Yu, Z. and Eicher, U. (1998). Abrupt climate oscillations during the last deglaciation in central North America. *Science* 282(5397), 2235–2238.
- Yu, Z., McAndrews, J. H., and Siddiqi, D. (1996). Influences of Holocene climate and water levels on vegetation dynamics of a lakeside wetland. *Canadian Journal of Botany* 74(10), 1602–1615.
- Yu, Z., McAndrews, J. H., and Eicher, U. (1997). Middle Holocene dry climate caused by change in atmospheric circulation patterns: Evidence from lake levels and stable isotopes. *Geology* 25(3), 251–254. issn: 00917613.
- Yusuf, M., Fariduddin, Q., Hayat, S., and Ahmad, A. (2011). Nickel: an overview of uptake, essentiality and toxicity in plants. *Bulletin of environmental contamination and toxicology* 86(1), 1–17.
- Zachara, J., Cowan, C., and Resch, C. (1991). Sorption of divalent metals on calcite. *Geochimica et cosmochimica acta* 55(6), 1549–1562.